Linear Stability Investigations of Three-Dimensional Disturbances in the Boundary Layer over Anisotropic Compliant Walls

A thesis accepted by the Faculty of Aerospace Engineering and Geodesy of the University of Stuttgart in partial fulfilment of the requirements for the degree of Doctor of Engineering Sciences (Dr.-Ing.)

submitted by
Marcus Matthias Zengl
born in
Gießen

main referee:	apl. Prof. Dr.-Ing. Ulrich Rist
co-referee:	Prof. Dr.-Ing. habil. Christoph Brücker
co-referee:	Prof. Dr. rer. nat. Claus-Dieter Munz
date of defence:	January 10, 2023

Institut für Aerodynamik und Gasdynamik
Universität Stuttgart
2023

Vorwort

Der überwiegende Teil der vorliegenden Arbeit entstand während meiner Tätigkeit als Wissenschaftlicher Mitarbeiter am Institut für Aerodynamik und Gasdynamik (IAG) der Universität Stuttgart. Sie basiert auf den Erkenntnissen und Methoden des Forschungsprojekts "Numerische Untersuchungen zur Laminarhaltung durch kontrollierte Wandschwingungen" das im Rahmen des Schwerpunktprogramms SPP 1207 "Strömungsbeeinflussung in der Natur und Technik" durch die Deutsche Forschungsgemeinschaft (DFG) finanziert wurde.

Herrn apl. Prof. Dr.-Ing. Ulrich Rist danke ich ganz herzlich für die Betreuung meiner Arbeit, sowohl während meiner Zeit am IAG als auch darüber hinaus. Er hatte stets Vertrauen in mich und gewährte mir viel Freiheit bei meiner Forschung.

Allen Kolleginnen und Kollegen am IAG danke ich von ganzem Herzen. Die kollegiale Unterstützung, viele wertvolle Diskussionen und auch die gelegentliche Ablenkung haben die Arbeit am Institut sehr bereichert. Bei meinen Projektpartnern des Schwerpunktprogramms möchte ich mich ebenfalls für die gute Zusammenarbeit bedanken. Prägend für die vorliegende Arbeit waren auch die ersten beiden Young ERCOFTAC Workshops der European Research Community On Flow, Turbulence and Combustion (ERCOFTAC), bei denen ich jeweils teilnehmen durfte.

Nicht zuletzt möchte ich meiner Familie danken, insbesondere meinen Eltern und meiner Frau Katharina. Ihre Unterstützung und ihr Verständnis waren ein wichtiger Rückhalt während meiner Promotionszeit.

Gaimersheim, im Oktober 2023 Marcus Zengl

Contents

Nomenclature

Upper Case Roman

C_m	wall inertia coefficient
C_k	wall spring stiffness coefficient
C_d	wall damping coefficient
C_b	wall bending stiffness coefficient
C_{Tx}	streamwise wall tension coefficient
C_{Tz}	spanwise wall tension coefficient
C_i	induced tension coefficient
C_ν	transversal contraction coefficient
E	disturbance energy
L	reference length
N	degrees of freedom / N-factor
N_c	number of collocation points
$\mathbf{Q}_E$	energy weight matrix
Re	Reynolds number
U_∞	reference velocity

Lower Case Roman

$c_{\text{ph.}}$	phase speed
$\vec{e}$	unit vector
i	imaginary unit ($= \sqrt{-1}$)
p	pressure
t	time
$t_1 \ldots t_6$	terms of the Orr-Sommerfeld and Squire ens.
t_8	term of the free stream boundary condition

u	streamwise velocity
v	wall-normal velocity
w	spanwise velocity
$\mathbf{w_{cc}}$	Clenshaw-Curtis quadrature weights
x	streamwise coordinate / solution vector
y	wall-normal coordinate
z	spanwise coordinate
$z_1 \ldots z_6$	disturbance quantities of the Orr-Sommerfeld and Squire eqns.

Upper Case Greek

Ψ	wave propagation angle
Ω	wall-normal vorticity
Λ	diagonal eigenvalue matrix

Lower Case Greek

α	streamwise wavenumber (complex)
β	spanwise wavenumber (complex)
γ	shear strain
δ_1	displacement thickness
δ_2	momentum thickness
δ_{99}	boundary layer thickness
δ_{ij}	Kronecker delta $(= \vec{e_i} \cdot \vec{e_j})$
ϵ	normal strain / BC residual
ζ	spanwise wall elongation
η	wall-normal wall elongation
θ	anisotropy angle
κ	resulting wavenumber (complex)
λ	wavelength

μ	dynamic viscosity / boundary condition parameter
ν	kinematic viscosity
ξ	streamwise wall elongation
ρ	density
σ	normal stress / singular value
τ	shear stress
φ	flow quantity
ϕ	wall quantity
ψ	yaw angle
ω	(complex) angular frequency

Symbols

$\mathcal{D}$	differentiation operator with respect to y

Subscripts

r, i	real & imaginary part
w	wall
x	vector component / derivative in x-direction
y	vector component / derivative in y-direction
z	vector component / derivative in z-direction
∞	reference quantity

Superscripts

$\star$	dimensional quantity
$^{-}$	mean quantity
$^{\prime}$	disturbance quantity

˘	quantity in the (unmapped) domain $[-1, 1]$
˘	quadrature weights within $y \in [0, y_{\max}]$
~	modal quantity (complex)
$*$	complex conjugate
H	transpose complex conjugate

Abbreviations

BC	boundary condition
BL	boundary layer
CFD	computational fluid dynamics
CIFI	compliance-induced flow instability
FISI	flow-induced surface instability
LST	linear stability theory
OS	Orr-Sommerfeld
PIV	particle-image velocimetry
SQ	Squire
SVD	singular value decomposition
TS	Tollmien Schlichting
app.	appendix
eqn.	equation
eqns.	equations
fig.	figure
sect.	section
chap.	chapter

Abstract

In this work three-dimensional disturbances in the boundary layer over anisotropic compliant walls are investigated by application of linear stability theory. A surface-based was model is used to simulate the compliant wall. Hereby, the anisotropic wall model of Carpenter [15] is extended to accommodate an additional yaw angle with respect to the flow direction. Based on this wall model a boundary condition for the linear stability theory is derived. Since this novel boundary condition couples the Orr-Sommerfeld and Squire equation, two novel solvers, a shooting solver and a matrix solver, which account for this circumstance were developed.

The shooting solver transforms the governing eigenvalue problem to a boundary value problem and uses a classical approach of shooting and minimizing the boundary condition residual, to solve the problem. The solver incorporates a Gram-Schmid orthonormalization procedure to account for the numerically stiff problem and its intrinsic parasitic-error growth. With the use of a novel phase scaling of the residual, which is to be minimized, it is robust and performant to investigate a given spatial or temporal mode.

For temporal stability investigations the coupled Orr-Sommerfeld and Squire eigenvalue problem is solved with the matrix solver. The quadratic eigenvalue problem that the compliant wall introduces is taken care of. Hereby, a pseudospectral discretization using Chebyshev collocation points is used. Special care is taken in the formulation of the discretized problem to reduce numerical errors. The numerical accuracy of the solvers is scrutinized to make sure that the results are grid independent.

To investigate the potential of compliant walls to delay laminar-turbulent transition the approach of Carpenter [15] was adopted. Carpenter optimized compliant-wall parameters to attenuate Tollmien-Schlichting (TS) modes as far as possible, while leaving Flow-Induced Surface Instability (FISI)

modes marginally stable. This approach was chosen, because FISI modes can exhibit absolute instability, which can lead to immediate transition. Stability calculations were carried out for two sets of wall parameters, which Carpenter has optimized with his two-dimensional framework. Hereby, not only three-dimensional disturbances are considered, but also an additional yawing of the compliant wall was investigated as well. Results are judged with respect to temporal stability of the TS and FISI modes, and with respect to the spatial amplification and transition prediction using N-factors. It is shown that three-dimensional disturbances reach given N-factors before their two-dimensional counterparts. The predicted laminar length is slightly shorter than it its predicted in two-dimensional solvers. Also it appears that yawing of the compliant material is not favorable for transition delay for the underlying wall and flow parameters.

Finally, optimal perturbations are calculated for the anisotropic compliant wall to investigate transient energy growth. Hereby, the initial amplitudes of the computed eigenmodes are optimized, so that the superposition of these modes reaches its maximum energy growth for a given time. The envelope of these optimal perturbations is then calculated for varying streamwise and spanwise wavenumbers, and varying time of growth. Results show that no relevant transient growth is introduced by the compliant materials. It is shown that the classical transient growth mechanism, which prevails in the rigid wall case, is not altered.

Kurzfassung

In dieser Arbeit werden dreidimensionale Störungen in der Grenzschicht über anisotropen nachgiebigen Wänden mit linearer Stabilitätstheorie untersucht. Ein oberflächenbasiertes Modell wird verwendet, um die nachgiebige Wand abzubilden. Hierbei wird das anisotrope Wandmodell von Carpenter [15] erweitert, um einen zusätzlichen Schiebewinkel der Wand bezüglich der Strömungsrichtung einzubringen. Basierend auf diesem Wandmodell wird eine Randbedingung für die Lineare Stabilitätstheorie hergeleitet. Aufgrund der Tatsache, dass diese Randbedingung die Orr-Sommerfeld- und Squire-Gleichung koppelt, wurden zwei neuartige Lösungsverfahren, ein Schießverfahren und ein Matrixlöser, für diesen besonderen Umstand entwickelt.

Der Schießlöser transformiert das zugrunde gelegte Eigenwertproblem in ein Randwertproblem und verwendet ein klassisches Schießverfahren zur Lösung des Problems. Um das numerisch steife Problem mit seinem parasitärem Fehlerwachstum zu berücksichtigen beinhaltet das Lösungsverfahren eine Gram-Schmid Orthonormierungsroutine. Durch eine neuartige Skalierung der Phase des zu minimierenden Residuums wird das zeitliche und räumliche Modell robust und performant für gegebene Eigenmoden gelöst.

Das durch die gekoppelte Orr-Sommerfeld- and Squire-Gleichung entstehende Eigenwertproblem wird auch mit einer Matrix-basierenden Methode gelöst. Das durch die nachgiebige Wand entstehende zeitliche quadratische Eigenwertproblem wird dabei berücksichtigt. Hierbei wird eine pseudospektrale Diskretisierung mit Chebyshev-Kollokation verwendet. Besonders betrachtet wird die Formulierung des diskretisierten Problems auf seine numerischen Fehler. Die numerische Genauigkeit der Lösungsverfahren wird genau überprüft, um die Gitterunabhängigkeit der Ergebnisse sicher-

zustellen.

Um das Potenzial der nachgiebigen Wände zur Verzögerung des laminar-turbulenten Umschlags zu untersuchen, wurde die Vorgehensweise von Carpenter [15] übernommen. Carpenter optimierte die Parameter der nachgiebigen Wand so, dass Tollmien-Schlichting (TS) Moden so weit wie möglich abgeschwächt werden, während Fluid-Struktur (FISI) Moden grenzwertig stabil bleiben. Dieses Vorgehen wurde ausgewählt, weil Fluid-Struktur Moden absolut instabil sein können, was zu sofortigem Strömungsumschlag führen kann. Stabilitätsrechnungen wurden ausgeführt für zwei Sätze von Wandparametern, die Carpenter mit seinem zweidimensionalen Rahmenwerk optimiert hat. Hierbei wurden nicht nur dreidimensionale Störungen betrachtet, sondern es wurde auch der Einfluss des neu eingebrachten Schiebewinkels der nachgiebigen Wand untersucht. Die Ergebnisse wurden bezüglich der zeitlichen Anfachung der TS- und FISI-Moden, und bezüglich des mit N-Faktoren vorhergesagten Umschlagspunkts beurteilt. Es wird gezeigt, dass dreidimensionale Störungen bestimmte N-Faktoren vor ihren zweidimensionalen Pendants erreichen. Die vorhergesagte laminare Länge ist etwas kürzer als mit zweidimensionalen Verfahren vorhergesagt. Es scheint als ob der eingebrachte Schiebewinkel für die untersuchten Parametersätze keinen Vorteil bezüglich Laminarhaltung bringt.

Schließlich wurden optimale Störungen berechnet, um das Transiente Energiewachstum für die anisotrope nachgiebige Wand zu untersuchen. Hierbei wurden die Anfangsverteilungen von Eigenmoden so optimiert, dass deren Überlagerung ein maximales Energiewachstum für eine vorgegebene Zeit erfährt. Die Einhüllende dieser optimalen Störungen wird dann für variierende Wellenzahlen in Strömungs- und Spannweitenrichtung, und variierende Wachstumszeit berechnet. Die Ergebnisse zeigen kein durch die nachgiebige Wand hervorgerufenes relevantes transientes Wachstum. Es wird gezeigt, dass der klassische Mechanismus für transientes Wachstum, der bei der steifen Wand dominiert, nicht verändert wird.

1 Introduction

There has also been some work done on the stability of inviscid flows over flexible coatings. (...) The main feature that their models lack is the viscosity of the fluid.

R. D. Joslin

Reduction of aerodynamic drag is of interest in various engineering fields, while in aerodynamic vehicles frictional drag is superior to pressure drag. Different approaches exist to reduce friction drag—these are, e.g., shape optimization, modification of the turbulent boundary layer (BL) or delay of laminar-turbulent transition. Since laminar-turbulent transition is caused by the instability of the laminar flow, it is possible to delay transition by altering its stability properties. For flows dominated by Tollmien-Schlichting (TS) type instabilities, this can be done by heating or cooling of the wall (depending on the fluid), boundary layer suction, shape optimization, or—in focus of this work—the application of compliant coatings. The TS instability can be attenuated or even inhibited with the application of compliant coatings.

Due to the fact that both, the boundary layer and the compliant wall are wave-bearing media, the analysis of the combined system is more complicated than the analysis of the boundary layer over a rigid wall. Additional instability modes emerge, which are dominated by wall oscillations. Carpenter [13, 14] named these modes flow-induced surface instability (FISI) modes. In contrast to that Yeo [70, 68, 69] named these modes compliance-induced flow instability (CIFI) modes. For convenience and without judgment the term FISI is used in this work. FISI modes can become unstable and, more importantly, can become absolutely unstable. Commonly a change of a compliant wall property has opposing effects on the stability of the TS mode and the FISI modes: stabilizing the TS eigenvalue and destabilizing the FISI modes, or vice versa. So a trade-off is to be made. Carpenter proposed to

optimize the wall parameters such that the TS mode is maximally stabilized while keeping the FISI modes stable to avoid possible absolute instabilities. Moreover, the consideration of three-dimensional (oblique) disturbances is fundamental for the assessment of external flows over compliant walls (e.g. [39, 69]). Depending on the wall parameters oblique-traveling disturbances can be more or less dominant. In spite of these facts, the use of compliant walls can lead to significant transition delays.

1.1 Historical Overview

Comprehensive reviews on the effects of compliant walls on boundary layers exist in literature (e.g. [36, 52, 25, 17]). Most reviews generally address different topics together: the effect on laminar-turbulent transition, the reduction of turbulent skin friction, and the suppression of flow-induced noise and vibrations. In this short review the focus is on linear stability of external flows.

In the 1950s the influence of compliant walls on drag reduction was investigated by Kramer [41]. He reported a significant drag reduction caused by an increase in laminar length and provided a simplified theory. Kramer argued that the rubber coating in close contact to the fluid increases the damping in the boundary layer and thus delays breakdown to turbulence. Indeed, this sound explanation is somewhat too simple—friction can actually cause fluid instabilities as it is the case in the Blasius boundary layer, which is inviscidly stable. Theoretical works in the following years (e.g. [5, 42, 6]) indicated that a delay of transition is generally possible. Investigators also tried to reproduce Kramer's findings experimentally, but no significant drag reduction was reported. However, in these experiments the joints between the solid and the compliant coating as well as the free-stream turbulence level were problematic. Attention was then drawn to the effects of compliant coatings on turbulent boundary layers, because it might have been the case that the reduction of skin friction in Kramer's experiments could have been caused by a reduction of turbulent skin friction, but this physical mechanism is out of the scope of this work.

In the mid 1980s Carpenter and Garrad [13, 14] investigated the effects of compliant coatings by numerical solution of the Orr-Sommerfeld equation, and theoretical considerations. They reported only marginal improvements concerning the materials Kramer has used, but also reported that "Kramer-type coatings are theoretically capable of considerable transition postponement [...]." Shortly after that Gaster [26] presented that compliant coatings are also practically, i.e. in an experiment, capable of transition postponement. He found good agreement between linear stability calculations and experimental measurements in the low-disturbance environment of a towing tank. The best surface tested showed an increase of 30 percent in the transition Reynolds number.

In 1990 Carpenter and Morris [15] as well as Yeo [68] presented investigations of anisotropic compliant coatings with considerable potential to improve transition delay. A rise of the transition Reynolds number ten times as well as seven times the value of rigid walls has been reported, respectively. Additionally, Joslin and Morris [37] pointed out techniques to optimize compliant wall parameters numerically. However, these works considered only two-dimensional disturbances.

Three-dimensional disturbances were then investigated by Joslin [39] and Yeo [69] with the conclusion that three-dimensional TS-instabilities are more unstable than their two-dimensional counterparts for sufficiently compliant walls. This leads to an overestimation of the transition Reynolds number, but still a significant transition delay can be achieved in case surface modes are inhibited. Their findings indicate that three-dimensional disturbances do play a critical role in transition over compliant coatings. Secondary instability was investigated by Joslin [38], who reported that compliant walls are also capable of attenuating secondary instabilities compared to the rigid wall case, and confirmed that suppression of primary instability growth also results in a suppression of secondary instability growth.

1.2 Compliant Walls in Nature

Various flow-control features exist in swimming fishes and mammals and birds. Of popular interest has been shark skin which features streamwise microgrooves that reduce turbulent skin friction. These so-called riblets can reduce the local friction coefficient by up to 8% for practical configurations [4]. Other drag reducing features are the long chained polymers of fish slime (e.g. [19]) or micronized air bubbles on the plumage of penguins which reduce skin friction (cf. Davenport [20]).

Delphinidae feature in contrast to the aforementioned species a smooth and noticeable compliant epidermis. In the 1930s Sir James Gray [29] analyzed the musculature of dolphins and came to the conclusion that delphinidae must either have enormously powerful muscles or must have a mechanism that reduces their hydrodynamic drag. This is called Gray's paradox. The experiments of Kramer [41] indicated that the compliant epidermis of dolphins could lead to a postponement of laminar-turbulent transition, which reduces frictional drag and could solve Gray's paradox. Recently, Legac et.al. [43] performed PIV measurements of swimming dolphins and concluded that Gray was in error with his calculation of the propulsive power that dolphins can develop—Gray's paradox was solved. Still it has not been proven wrong that the dolphin could possess a drag reduction mechanism with it's appreciable compliant epidermis.

The investigation of dolphin's epidermis is not trivial, because it changes it's mechanical properties, i.e. its compliance, postmortem. Additionally, these properties can be altered by the tension of the skin muscle. Hence, tests if its physical properties are capable of damping fluid instabilities must be done in vivo. Practical, ethical, and monetary reasons prohibit the investigation of the mechanical properties of dolphins skin. Pavlov [49] investigated the epidermis of harbor porpoises (Phocoena phocoena) and compared the local skin morphology to the local flow conditions which were calculated using CFD. He hypothesized that the epidermis acts like an anisotropic compliant wall due to dermal ridges within the papillary layer. Furthermore, he reported that these dermal ridges make an angle to the local

flow direction which varies over the streamwise location. These findings inspired the extension of the physical wall model used by Carpenter [15], which is presented in chap. 2. Two numerical solvers incorporating this extension of the wall model are presented in chap. 3 and 4. Investigations using this novel wall model are presented in chap. 5 and 6.

1.3 Transient Growth in the Flow over Compliant Walls

In the derivation of the Orr-Sommerfeld and Squire equation a modal ansatz was introduced (cf. app. B) which leads to the eigenvalue problem. The exponential growth or decay of these modes determines if the flow is asymptotically unstable or stable, respectively, to these modes for large times ($t \rightarrow \infty$). However, the short-time dynamics of disturbances are only captured by these modes in disguise. Generally a disturbance can be described as a superposition of these modes. Since these modes are generally non-orthogonal, which is also the case for external flow over compliant walls, a short-time growth to a certain disturbance level can occur long before the least stable mode would reach the same level. Additionally, a flow can exhibit disturbance growth within a finite-time horizon even though it is asymptotically stable for $t \rightarrow \infty$. This type of growth that can not be ascribed to a single mode is commonly termed non-modal growth or transient growth. A concise review of non-modal stability can be found in Schmid [54].

Commonly, non-modal stability theory is relevant for flows in which modal growth is very low or non-existent. Since optimized anisotropic compliant walls exhibit low growth rates of the TS-mode, as a matter of fact non-modal growth becomes a more relevant route to turbulence. In sect. 4.7 of this work it was suggested that numerical errors, due to non-orthogonality of the eigenmodes, are larger for compliant walls than for the rigid wall. This indicates that the non-modal growth of flow over compliant walls might be larger than flow over rigid walls. Therefore, we investigate in the following if and how anisotropic compliant walls change the transient behavior of disturbances in the boundary layer. We calculate optimal perturbations based on the temporal eigenmodes of the Orr-Sommerfeld and Squire equation

and compare the rigid-wall case to the compliant-wall case.

Butler and Farrell [12] investigated the non-modal growth of disturbances inter alia in the Blasius BL over rigid walls. They compared 2-D optimal perturbations with 3-D optimal perturbations and reported that 3-D structures exhibited clearly stronger growth factors. They found energy growth factors up to $E(\tau)/E(0) = 1514$ for three-dimensional structures (at $Re_{\delta_1} = 1000$). Zengl and Rist [72] investigated transient growth in the Blasius boundary layer over anisotropic compliant walls, but the author admits that the energy norm under consideration did not include the potential energy of the compliant wall, which can cause misleading conclusions. Later Hœpffner et al. [34] investigated the evolution of non-modal growth in channel flow between isotropic compliant walls. They found an additional transient-growth mechanism which involves both FISI modes forming a standing wave in two forms—a sinuous (antisymmetric to the channel half width) and a varicose (symmetric to the channel half width) form. 2017 Tsigklifis and Lucey [66] investigated the two-dimensional global, local and transient stability of a compliant panel in the Blasius boundary layer. They found that, depending the compliant material properties, considerable transient growth can take place.

2 Physical Wall Model

> One of the central problems of carrying out any numerical investigation of boundary-layer stability over a compliant wall is the proliferation of parameters relating to the wall properties.

Peter W. Carpenter and Philipp J. Morris

For the numerical computation of linear stability properties a physical model must be used to resemble the compliant wall characteristics. In this chapter the kinematic model of the compliant wall is presented. The non-dimensionalization and derivation of the equation of wall motion is scrutinized. Boundary conditions for the two formulations of equations are derived for the application in local linear-stability theory. Finally, application of Squire's findings is discussed under the aspect of external boundary layers with increasing thickness.

2.1 Kinematic Model of the Compliant Wall

In order to investigate the stability properties of compliant walls, e.g., by stability theory or direct numerical simulations, the compliant wall must be modeled. Two types of wall models prevail in literature: so-called volume-based wall models (e.g. [70, 68, 69]) which treat the compliant coating as continuous volume, and so-called surface-based wall models (e.g. [13, 14, 15]) which treat the compliant coating as a spring-backed flexible plate. The volume-based approach resembles the physics of the applied compliant coating by application of the Navier equation, while the surface-based approach—which was chosen for this work—simplifies the wall as a spring backed plate and is therefore less complex. Duncan [21] provides a comparison between the two approaches.

The compliant-wall model used in this work is an extension of the model

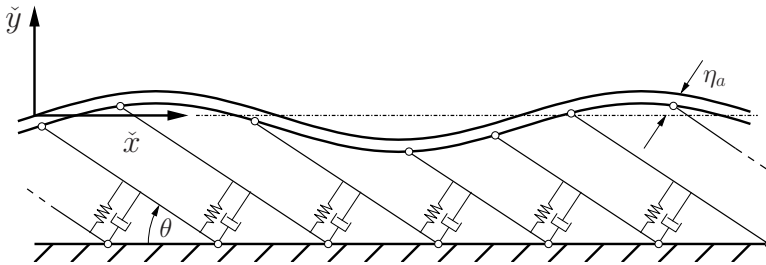used in Carpenter [15]. A cross-section is shown in fig. 2.1. The wall is

Figure 2.1 Cross-section of the anisotropic compliant wall model.

represented as a spring-backed flexible plate bound to a rigid base by stiff swivel arms. These swivel arms feature springs and dampers which are attached to them. It is assumed that there are sufficiently enough swivel arms compared to the smallest wavelength under consideration so that their effect on the wall motion can be seen as continuous. The anisotropy angle, i.e. the angle of swivel arms to the surface plane, is denoted as θ. The absolute value of the wall elongation perpendicular to the swivel arms is denoted as η_a. As an extension to Carpenter [15] the wall can be yawed by the angle ψ with respect to the flow direction, which is illustrated in fig. 2.2.
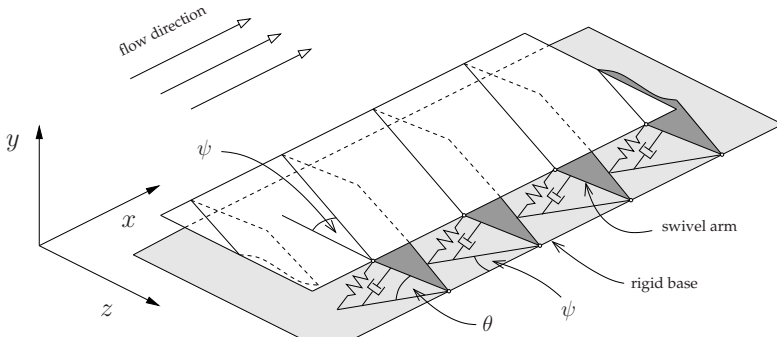

Figure 2.2 Illustration of the yawed anisotropic compliant wall model.

The elongation of a point on the surface of the wall in streamwise, wall-

normal, and spanwise direction is termed ξ, η, and ζ, respectively. The swivel arms of the anisotropic wall couple this movement so that

$$\xi = \sin(\theta)\cos(\psi)\,\eta_a \tag{2.1}$$

$$\eta = \cos(\theta)\,\eta_a \tag{2.2}$$

$$\zeta = \sin(\theta)\sin(\psi)\,\eta_a \ . \tag{2.3}$$

For $\theta = 0$ only a movement in wall-normal direction is possible which resembles the isotropic compliant wall. In fact the equations of the anisotropic and the isotropic compliant-wall boundary conditions are identical in this case.

2.2 Non-Dimensionalization of the Compliant Wall Parameters

Various material properties play a role for the different inner forces of the compliant wall. Non-dimensional wall parameters can be formed which relate these properties to the fluid properties. Two definitions of dimensionless parameters are used in this thesis. These are listed in Table 2.1. Hereby

Table 2.1 Dimensionless parameters of the anisotropic compliant-wall.

non-dimensional parameter	definition I	definition II
wall inertia	$C_m = \frac{\rho_m^\star b_m^\star}{\rho^\star L^\star}$	$C_m^{(\nu)} = \frac{\rho_m^\star b_m^\star U_\infty^\star}{\rho^\star \nu^\star}$
spring stiffness	$C_k = \frac{k_m^\star L^\star}{\rho^\star U_\infty^{\star\,2}}$	$C_k^{(\nu)} = \frac{k_m^\star \nu^\star}{\rho^\star U_\infty^{\star\,3}}$
wall damping	$C_d = \frac{d_m^\star}{\rho^\star U_\infty^\star}$	$C_d^{(\nu)} = \frac{d_m^\star}{\rho^\star U_\infty^\star}$
bending stiffness	$C_b = \frac{B^\star}{\rho^\star U_\infty^{\star\,2} L^{\star\,3}}$	$C_b^{(\nu)} = \frac{B^\star U_\infty^\star}{\rho^\star \nu^{\star\,3}}$
longitudinal tension	$C_{Tx} = \frac{T_x^\star}{\rho^\star U_\infty^{\star\,2} L^\star}$	$C_{Tx}^{(\nu)} = \frac{T_x^\star}{\rho^\star U_\infty^\star \nu^\star}$
transversal tension	$C_{Tz} = \frac{T_z^\star}{\rho^\star U_\infty^{\star\,2} L^\star}$	$C_{Tz}^{(\nu)} = \frac{T_z^\star}{\rho^\star U_\infty^\star \nu^\star}$
induced tension	$C_i = \frac{E_b^\star b_m^\star}{\rho^\star U_\infty^{\star\,2} L^\star}\frac{1}{1-\nu_p^2}$	$C_i^{(\nu)} = \frac{E_b^\star b_m^\star}{\rho^\star U_\infty^\star \nu^\star}\frac{1}{1-\nu_p^2}$
transversal contraction	$C_\nu = \frac{1+\nu_p}{2}$	$C_\nu^{(\nu)} = \frac{1+\nu_p}{2}$
anisotropy angle	θ	θ
yaw angle	ψ	ψ

starred quantities denote dimensional parameters. Note that a reference length $L^\star$ must be chosen for the non-dimensionalization of the parameters, as it can be seen in definition I. In the numerical implementation of the programs used for this thesis, a user-specified *global* Reynolds number defines the reference length $L^\star = Re\,\nu/U_\infty$. Carpenter and others typically choose the *local* displacement thickness $\delta_1^\star$ of the velocity profile under investigation. This implies that the non-dimensional wall parameters generally vary over the steamwise coordinate in case the dimensional wall parameters are constant over the streamwise coordinate. The so-called *viscous length* $L_\nu^\star = \nu/U_\infty$ is an alternative to the local displacement thickness as a reference length. It is constant over the streamwise coordinate and leads to definition II. Thus our dimensionless wall parameters remain constant in the boundary layer for constant dimensional parameters. Please note that definition I is generally used in the equations of this work unless the compliant wall parameters are marked with the superscript $^{(\nu)}$.

2.3 The Equation of Wall Motion

An equation of motion can be determined for the wall by considering its inner forces, i.e. the forces due to

- the springs and dampers,

- the bending stiffness of the flexible plate,

- the longitudinal and transversal tensioning of the flexible plate,

- and the restricted motion of the swivel arms.

Hereby, it is assumed that the neutral wall position is planar. These inner forces are balanced by its inertia and the force of the fluid on the wall, i.e. the pressure and shear stress at the interface. All forces acting on the compliant wall must be in dynamic equilibrium, and the velocities and stresses of the fluid and the wall must be equal at their interface. The following forces on the wall act in the direction of the degree of freedom, or in other words perpendicular to the swivel arms.

Due to the springs of the kinematic model the surface-specific force

$$f_k = C_k \eta_a \tag{2.4}$$

acts on the wall. Since the kinematic model also features dampers, the surface-specific damping force is

$$f_d = C_d \frac{\partial \eta_a}{\partial t} \quad . \tag{2.5}$$

The surface-specific bending force [32, sect. 3.6]

$$f_b = \cos^2 \theta \, C_b \left(\frac{\partial^4 \eta_a}{\partial x^4} + 2 \frac{\partial^4 \eta_a}{\partial x^2 \partial z^2} + \frac{\partial^4 \eta_a}{\partial z^4} \right) \tag{2.6}$$

of the flexible plate acts on the wall. In case the plate has a longitudinal or transversal tension $T_x^\star$ in x-direction and $T_z^\star$ in z-direction, the surface specific force [32, sect. 3.5]

$$f_t = - \cos^2 \theta \left(C_{Tx} \frac{\partial^2 \eta_a}{\partial x^2} + C_{Tz} \frac{\partial^2 \eta_a}{\partial z^2} \right) \quad . \tag{2.7}$$

acts on the wall. The stiffeners of the compliant-wall model induce a tension in the flexible plate when it is elongated. The derivation of the induced tension follows the ansatz of Boyer [9]. When considering an infinitely wide compliant material, or a finite material which is not allowed to contract at the sides, a transversal contraction is inhibited. This results in a state of biaxial stress. With Hooke's law [31, eqns. (3.11)-(3.12)]

$$\epsilon_x E = \sigma_x - \nu_p \sigma_z \tag{2.8a}$$

$$\epsilon_z E = \sigma_z - \nu_p \sigma_x \tag{2.8b}$$

$$\gamma_{xz} E = 2 \left(1 + \nu_p \right) \tau_{xz} \quad , \tag{2.8c}$$

the mechanical equilibrium conditions [31, eqn. (2.21)]

$$\frac{\partial \sigma_x}{\partial x} + \frac{\partial \tau_{xz}}{\partial z} + \frac{f_{ix}}{b_m} = 0 \tag{2.9a}$$

$$\frac{\partial \sigma_z}{\partial z} + \frac{\partial \tau_{xz}}{\partial x} + \frac{f_{iz}}{b_m} = 0 \quad , \tag{2.9b}$$

and the strains [31, eqn. (3.6)]

$$\epsilon_x = \frac{\partial \xi}{\partial x} \ , \tag{2.10a}$$

$$\epsilon_z = \frac{\partial \zeta}{\partial z} \ , \text{and} \tag{2.10b}$$

$$\gamma_{xz} = \frac{1}{2} \left(\frac{\partial \xi}{\partial z} + \frac{\partial \zeta}{\partial x} \right) \tag{2.10c}$$

we obtain

$$f_i = -C_i \sin^2 \theta \left(\frac{\partial^2}{\partial x^2} + \frac{\partial^2}{\partial z^2} - C_\nu \left(\sin \psi \frac{\partial}{\partial x} - \cos \psi \frac{\partial}{\partial z} \right)^2 \right) \eta_a \tag{2.11}$$

for the surface-specific induced tension force in the direction of elongation. Note that Carpenter [15] uses, in contrary to the present implementation, a uniaxial stress state for the determination of the induced tension. In order to compare the results with Carpenter, a Poisson ratio of $\nu_p = 0$ must be used for the calculation of C_i and C_ν.

The wall-normal stress of the fluid and the wall must be equal. The stress tensor of an incompressible fluid is [3, sect. 4.1]

$$\sigma_{ij}^\star = -p^\star \, \delta_{ij} + \mu \left(\frac{\partial u_i^\star}{\partial x_j^\star} + \frac{\partial u_j^\star}{\partial x_i^\star} \right) \ . \tag{2.12}$$

After non-dimensionalization using (B.1) we find that the surface-specific force of the fluid acting on the wall surface must be

$$\vec{f_f} = -p\,\vec{n} + \frac{1}{Re} \begin{bmatrix} 2\frac{\partial u}{\partial x} & \frac{\partial u}{\partial y} + \frac{\partial v}{\partial x} & \frac{\partial u}{\partial z} + \frac{\partial w}{\partial x} \\ \frac{\partial v}{\partial x} + \frac{\partial u}{\partial y} & 2\frac{\partial v}{\partial y} & \frac{\partial v}{\partial z} + \frac{\partial w}{\partial y} \\ \frac{\partial w}{\partial x} + \frac{\partial u}{\partial z} & \frac{\partial w}{\partial y} + \frac{\partial v}{\partial z} & 2\frac{\partial w}{\partial z} \end{bmatrix} \vec{n} \ . \tag{2.13}$$

Hereby,

$$\vec{n} = \frac{\vec{e}_y - \left(\cos \psi \frac{\partial \eta}{\partial x} + \sin \psi \frac{\partial \eta}{\partial z} \right) \left(\cos \psi \, \vec{e}_x + \sin \psi \, \vec{e}_z \right)}{\sqrt{\left(\cos \psi \frac{\partial \eta}{\partial x} + \sin \psi \frac{\partial \eta}{\partial z} \right)^2 + 1}} \tag{2.14}$$

is the vector normal to the surface of the compliant wall. Note that due to linearization the wall-normal vector can be simplified to $\vec{n} = \vec{e}_y$, because the wall elongations in (2.14) drop out upon inserting the normal vector in (2.13).

Hence, the force of the wall acting on the fluid in the direction of freedom is accordingly

$$
f_f = \cos\theta \left(-p + \frac{2}{Re}\frac{\partial v}{\partial y} \right) +
$$
$$
\frac{\sin\theta}{Re} \left(\cos\psi \left(\frac{\partial u}{\partial y} + \frac{\partial v}{\partial x} \right) + \sin\psi \left(\frac{\partial w}{\partial y} + \frac{\partial v}{\partial z} \right) \right) \quad . \quad (2.15)
$$

Finally, the dynamic equilibrium is

$$
C_m \frac{\partial^2 \eta_a}{\partial t^2} + f_k + f_d + f_b + f_t + f_i = f_f \quad . \tag{2.16}
$$

2.4 Derivation of the Resulting Compliant Wall Boundary Conditions

The boundary conditions of the solved equations—in this work the linear stability equations—need to be derived according to the wall model. The boundary conditions in the linear stability theory are prescribed at the neutral wall position, i.e. at $y = 0$. This is the position where the wall is in static mechanical equilibrium. The location where the boundary conditions are prescribed is generally different to the momentarily wall position. Therefore, we use a Taylor series at the neutral wall position with the distance of the wall elongation to relate the fluid quantities at the wall to the fluid quantities at $y = 0$.

After application of the same linearization and modal approach as in the derivation of the Linear Stability equations we receive a set of three equations that serve as the boundary conditions for the *Orr-Sommerfeld* and the *Squire* equation. In general these equations couple the two equations so that both equations must be solved in combination. The consequences of this coupling are addressed in sect. 2.5.

The fluid and wall velocities must be equal at the fluid-wall interface. Therefore, we postulate

$$
u(\xi, \eta, \zeta) = \frac{\partial \xi}{\partial t} \tag{2.17}
$$

$$v(\xi, \eta, \zeta) = \frac{\partial \eta}{\partial t} \tag{2.18}$$

$$w(\xi, \eta, \zeta) = \frac{\partial \zeta}{\partial t} \ . \tag{2.19}$$

A Taylor series of the fluid velocities, the fluid pressure, and the fluid velocity gradients in (2.17)-(2.19) and (2.15) is used. For the fluid velocity in x-direction follows exemplarily

$$u(\xi, \eta, \zeta) = u\Big|_{y=0} + \xi \frac{\partial u}{\partial x}\Big|_{y=0} + \eta \frac{\partial u}{\partial y}\Big|_{y=0} + \zeta \frac{\partial u}{\partial z}\Big|_{y=0} + \mathcal{O}(\xi^2, \eta^2, \zeta^2) \ . \tag{2.20}$$

The quadratic and higher order terms will drop out in the following due to linearization.

As in appendix B, the fluid quantities are divided into a steady mean-flow and an unsteady sufficiently small disturbance, which are denoted by an overbar and an acute accent, respectively. Furthermore, it is assumed that the mean wall displacement is zero. Accordingly, the wall elongations ξ, η and ζ are disturbance quantities by definition. The equations are linearized so that products of disturbance terms drop out. For the velocity in x-direction we obtain the simplifications

$$\underbrace{\bar{u}(\xi, \eta, \zeta)}_{=\frac{\partial \bar{\xi}}{\partial t}=0} + \acute{u}(\xi, \eta, \zeta) = \bar{u}\Big|_{y=0} + \underbrace{\acute{u}\Big|_{y=0}}_{=0} + \xi \frac{\partial \bar{u}}{\partial x}\Big|_{y=0} + \underbrace{\xi \frac{\partial \acute{u}}{\partial x}\Big|_{y=0}}_{=0} + \eta \frac{\partial \bar{u}}{\partial y}\Big|_{y=0} +$$

$$\underbrace{\eta \frac{\partial \acute{u}}{\partial y}\Big|_{y=0}}_{=0} + \zeta \frac{\partial \bar{u}}{\partial z}\Big|_{y=0} + \underbrace{\zeta \frac{\partial \acute{u}}{\partial z}\Big|_{y=0}}_{=0} + \underbrace{\mathcal{O}(\xi^2, \eta^2, \zeta^2)}_{=0} \tag{2.21}$$

exemplarily. For the other Taylor expanded fluid quantities the linearization is analogous.

Like in the derivation of the Orr-Sommerfeld and the Squire equation, the modal approach

$$\phi(x, z, t) = \tilde{\phi} \, e^{\mathrm{i}(\alpha x + \beta z - \omega t)} + \text{complex conjugate} \tag{2.22}$$

is then used for the wall elongation ξ, η, and ζ. Derivatives with respect to streamwise and spanwise direction and with respect to time result in a

multiplication with streamwise and spanwise wavenumber and with angular frequency, respectively, in the acute-accent equations.

Regarding the governing quantities z_1 to z_6 (cf. sect. B) the wall boundary conditions

$$\omega z_1 + (\mathrm{i} t_2 - \omega t_4 \tan \theta)\, z_3 = 0 \ , \tag{2.23}$$

$$\left(-\cos^2\theta\, 2\, \mathrm{i}\omega\kappa^2\right) z_1 + \left(\sin\theta\,\cos\theta\,\omega t_4\right) z_2 + $$
$$\mathrm{i}\kappa^2 \left(\sin\theta\,\cos\theta\,(\omega t_4 + t_6) - CRe\right) z_3 + \left(-\cos^2\theta\,\omega\kappa^2 Re\right) z_4 + $$
$$\left(\sin\theta\,\cos\theta\,\omega t_5\right) z_6 = 0 \ , \tag{2.24}$$

and

$$(\mathrm{i} t_3 - \omega t_5 \tan \theta)\, z_3 + \omega z_5 = 0 \tag{2.25}$$

emerge with

$$t_4 = \alpha\,\cos\psi + \beta\,\sin\psi \tag{2.26}$$

$$t_5 = \alpha\,\sin\psi - \beta\,\cos\psi \tag{2.27}$$

$$t_6 = \bar{u}_{yy}\,\cos\psi + \bar{w}_{yy}\,\sin\psi \tag{2.28}$$

and

$$C = -\omega^2 C_m - \mathrm{i}\omega C_d + \cos^2\theta\,\kappa^4 C_b + $$
$$\cos^2\theta\,\alpha^2 C_{Tx} + \cos^2\theta\,\beta^2 C_{Tz} + \sin^2\theta(\kappa^2 - C_\nu t_5^2)C_i + C_k \ . \tag{2.29}$$

Note that the multiplier of z_6 in (2.24) drops out for the case of $\theta = 0$, i.e. for the isotropic compliant wall case, as well as for the case of $t_5 = 0$, i.e. for the case that the phase propagation angle $\arctan\left(\frac{\beta}{\alpha}\right)$ is equal to the yaw angle ψ of the material. In these two cases, the Orr-Sommerfeld and Squire equation are not coupled and can be solved independently. Since only two-dimensional waves over isotropic or unyawed anisotropic materials were considered in the works [13, 14, 15] the equations were decoupled and only the Orr-Sommerfeld eqn. had to be solved.

Regarding the formulation in terms of the wall-normal velocity $\tilde{v}$ and wall-normal vorticity $\tilde{\Omega}$ the boundary equations result in

$$\mathrm{i} t_2 \tilde{v} = \omega\left[\tan\theta\, t_4 - \mathrm{i}\mathcal{D}\right]\tilde{v} \ , \tag{2.30}$$

$$it_3\tilde{v} = \omega\left[\tan\theta\, t_5\tilde{v} - i\tilde{\Omega}\right] \quad, \tag{2.31}$$

and

$$\left[\kappa^2 ReC_d + \cos^2\theta\left(\mathcal{D}^3 - 3\kappa^2\mathcal{D}\right) + \cos^2\theta\, iRe\left(t_2 - t_7\mathcal{D}\right)\right.$$
$$\left. - \sin\theta\,\cos\theta\, it_4\left(\kappa^2 + \mathcal{D}^2\right)\right]\tilde{v}+$$
$$\kappa^2\left[ReC_k + Re\cos^2\theta\left(C_b\kappa^4 + \alpha^2 C_{Tx} + \beta^2 C_{Tz}\right) + \sin^2\theta\, C_i Re\left(\kappa^2 - C_\nu t_5^2\right)\right.$$
$$\left. - \sin\theta\,\cos\theta\, t_6\right]\eta+$$
$$\left[-\sin\theta\,\cos\theta\, it_5\mathcal{D}\right]\tilde{\Omega} = \omega\left[iRe\left(\kappa^2 C_m - \cos^2\theta\,\mathcal{D}\right)\right]\tilde{v} \quad, \tag{2.32}$$

with

$$t_7 = \alpha\bar{u} + \beta\bar{w} \quad, \tag{2.33}$$

and

$$i\tilde{v} = \omega\tilde{\eta} \quad. \tag{2.34}$$

Note that the compliant wall boundary conditions contain the square of the complex angular frequency ω and the sixth power of κ, or rather the sixth power of the streamwise wavenumber α. Hence the temporal problem becomes a quadratic eigenvalue problem and the spatial problem becomes a polynomial eigenvalue problem of sixth order. Also note that in the absence of a spanwise mean velocity ($\bar{w} = 0$) and spanwise wavenumber $\beta = 0$, the spatial problem reduces to fifth order.

2.5 Squire Theorem, Squire Modes and Squire Equation

Squire [59] showed up, that "For the study of the stability of flow between two parallel walls it is sufficient to confine attention to disturbances of two-dimensional type." This can be achieved by using an equivalent transformation of the Orr-Sommerfeld equation which links a neutrally stable three-dimensional mode with a corresponding neutrally stable two-dimensional mode at a lower Reynolds number. For the special case of two-dimensional self-similar external flows over rigid walls the same theory can be applied by non-dimensionalization of the equation with the local boundary-layer thickness, to prove that the first mode to become unstable is a two-dimensional

mode. Indeed, in most cases two-dimensional instability modes also show the highest cumulative growth, but this must not be taken as given. However, the application of this theory is not valid for flows with boundary conditions that vary over the streamwise location when non-dimensionalized with the local boundary-layer thickness. This is the case for the compliant walls present in this work. These exhibit constant dimensional properties in the streamwise direction—hence, three-dimensional disturbances must be and are considered here. Yeo [69] noted that for isotropic compliant walls the three-dimensional stability problem can be reduced to an equivalent two-dimensional problem, which then exhibits a higher (non-dimensional) wall stiffness. So three-dimensional disturbances experience a higher stiffness than their two-dimensional counterpart. He named this phenomenon the *stiffness rescaling effect*.

Instability modes for which the wall-normal disturbance velocity is zero, i.e. the trivial solutions of the Orr-Sommerfeld equation, are named Squire modes. Squire [59] has shown that these modes are always stable for flows between parallel walls. Beyond that, this can be generalized to all parallel flows. For compliant walls, Squire modes exhibit no wall-oscillations in the y-direction and consequently no wall-oscillation in the x- or z-direction, unless $\theta = 90°$ which is not covered by the wall-model in this work anyway. Consequently, the Squire modes of the considered wall-model are identical to the Squire modes over a rigid wall. Since these are always stable it is unnecessary to solve for them.

In general (local) linear stability is constituted by the Orr-Sommerfeld and the Squire equation which pose an eigenvalue problem. Hereby, the Orr-Sommerfeld equation contains only the wall-normal velocity and the Squire equation contains the wall-normal velocity and the wall-normal vorticity. For problems where the boundary conditions of the Orr-Sommerfeld equation do not depend on wall-normal vorticity the eigenvalue problem can be split into two smaller problems: (1) The eigenvalue problem of the Orr-Sommerfeld equation. (2) The eigenvalue problem of the Squire equation where the wall-normal velocity is set to zero. Hereby, the Squire equation is needed to calculate the wall-normal vorticity of the eigenfunctions of the Orr-

Sommerfeld equation. Consequently, the eigenvalues of the Squire equation where the wall-normal velocity is set to zero are stable. Therefore, only the eigenvalues of the Orr-Sommerfeld equation need to be calculated to find all possible unstable modes unless its boundary condition is dependent on wall-normal vorticity.

For the calculation of three-dimensional disturbances over anisotropic compliant walls, generally both equations are coupled by the wall boundary condition and must be solved in combination. The first mode to become unstable can be an oblique-traveling wave. There is no indication that two-dimensional modes reach certain amplitudes earlier than three-dimensional modes.

3 Shooting Solver

> We cannot repeat this too often: Asymptotic
> concepts like "convergence order" are meaningful
> only for large n. For small n, who knows!

<div align="right">John P. Boyd</div>

In this chapter a numerical method is presented to solve the stability equations using "shooting." The boundary-value problem is reduced to an initial-value problem. Hereby, streamwise wavenumber α or angular frequency ω are a parameter of this problem and determined, so that the boundary conditions of the boundary-value problem are fulfilled. The integration scheme is presented, the free-stream solutions that are used for starting the integration are shown, the orthogonalization procedure and the wall boundary conditions that must be met are explained. The iteration of the eigenvalues and the calculation of eigenfunctions is elucidated. Finally, the numerical accuracy of the shooting solver is scrutinized.

To solve the linear stability equations, namely the Orr-Sommerfeld and the Squire equation, one can rewrite the equations as a system of n first-order equations with k boundary conditions on one side, and $(n-k)$ boundary conditions on the other side. We obtain a linear boundary-value problem of the form

$$\frac{d}{dy}\mathbf{z}(y) = \mathbf{A}(y)\,\mathbf{z}(y) \ , \tag{3.1}$$

$$\mathbf{B}\,\mathbf{z}(y=0) = \mathbf{0} \ , \tag{3.2}$$

$$\mathbf{C}\,\mathbf{z}(y=y_{\text{max.}}) = \mathbf{0} \ , \tag{3.3}$$

with the solution vector $\mathbf{z}(y) = [z_1(y),\ldots,z_n(y)]^T$, $\mathbf{A}$ as an $n \times n$ matrix, $\mathbf{B}$ as a full rank $(n-k) \times n$ matrix, and $\mathbf{C}$ as a full rank $k \times n$ matrix. For this purpose, we choose to use equations (B.16)-(B.19) when only the solution of the Orr-Sommerfeld system is needed, and use equations (B.16)-(B.21) when the solution of the coupled Orr-Sommerfeld and Squire equation system is

needed. Hereby follows $n = 4$ and $k = 2$, or $n = 6$ and $k = 3$, respectively. Since the system of equations is linear, we can write its solution as a sum of n linearly independent base solutions $\mathbf{z}^{(i)}(y)$ in the form

$$\mathbf{z}(y) = c_1 \mathbf{z}^{(1)}(y) + c_2 \mathbf{z}^{(2)}(y) + \ldots + c_n \mathbf{z}^{(n)}(y) \ . \tag{3.4}$$

3.1 Integration Scheme

The baseflow in the interval $[0, y_{\mathrm{max}}]$ is divided into generally non-equidistant subintervals according to the data given at the N_p wall-normal grid points y_j , $(j = 1, \ldots, N_p)$. We write k linearly independent base solutions of equation (3.4) which meet the boundary condition (3.3) in the columns of the $n \times k$ matrix $\mathbf{Y}(y)$, with

$$\mathbf{Y}(y) = \begin{bmatrix} z_1^{(1)}(y) & \cdots & z_1^{(k)}(y) \\ \vdots & \ddots & \vdots \\ z_n^{(1)}(y) & \cdots & z_n^{(k)}(y) \end{bmatrix} \ . \tag{3.5}$$

This matrix must satisfy the equation

$$\frac{d}{dy} \mathbf{Y}(y) = \mathbf{A}(y) \, \mathbf{Y}(y) \ . \tag{3.6}$$

For numerical reasons the base solutions are integrated in the direction towards the wall. A standard Runge-Kutta (e.g. [47]) scheme

$$\mathbf{K}_1 = \mathbf{A}(y_{j+1}) \mathbf{Y}_{j+1} \ , \tag{3.7}$$

$$\mathbf{K}_2 = \mathbf{A}(y_{j+0.5}) \left(\mathbf{Y}_{j+1} + \tfrac{1}{2} h_j \mathbf{K}_1 \right) \ , \tag{3.8}$$

$$\mathbf{K}_3 = \mathbf{A}(y_{j+0.5}) \left(\mathbf{Y}_{j+1} + \tfrac{1}{2} h_j \mathbf{K}_2 \right) \ , \tag{3.9}$$

$$\mathbf{K}_4 = \mathbf{A}(y_j) \left(\mathbf{Y}_{j+1} + h_j \mathbf{K}_3 \right) \ , \tag{3.10}$$

$$\mathbf{Y}_j = \mathbf{Y}_{j+1} + \tfrac{1}{6} h_j \left(\mathbf{K}_1 + 2\mathbf{K}_2 + 2\mathbf{K}_3 + \mathbf{K}_4 \right) \tag{3.11}$$

with

$$h_j = y_j - y_{j+1} \tag{3.12}$$

is applied. For the intermediate stages of the Runge-Kutta scheme, the baseflow and its derivatives are interpolated with a piecewise Lagrangian

polynomial approximation of fourth order. An Aitken-Neville [11, sect. 19.6] algorithm was implemented for this purpose. The derivatives of the baseflow are calculated by fourth-order finite differences.

3.2 Free-Stream Boundary Condition

In the free stream, outside of the boundary layer, the base flow is uniform. The system of equations becomes a homogeneous linear system with constant coefficients, and has the solution

$$\mathbf{z}(y) = e^{\mathbf{A}(y - y_{\text{ref}})} \mathbf{z}(y_{\text{ref}}) = \mathbf{S} e^{\mathbf{\Lambda}(y - y_{\text{ref}})} \mathbf{S}^{-1} \mathbf{z}(y_{\text{ref}}) \ , \tag{3.13}$$

with $\mathbf{S}$ being the matrix containing the eigenvectors of $\mathbf{A}$, and the diagonal matrix $\mathbf{\Lambda}$ containing the corresponding eigenvalues λ_i of $\mathbf{A}$.

We denote the streamwise mean velocity by $\bar{u}_0$ and the spanwise mean velocity by $\bar{w}_0$ and obtain

$$\mathbf{S} = \begin{bmatrix} 1 & t_{8,0} & 0 & 1 & t_{8,0} & 0 \\ -\kappa & -t_{8,0}^2 & 0 & \kappa & t_{8,0}^2 & 0 \\ i\kappa^{-1} & i & 0 & -i\kappa^{-1} & -i & 0 \\ -t_{1,0}\kappa^{-2} & 0 & 0 & -t_{1,0}\kappa^{-2} & 0 & 0 \\ 0 & 0 & 1 & 0 & 0 & 1 \\ 0 & 0 & -t_{8,0} & 0 & 0 & t_{8,0} \end{bmatrix} , \tag{3.14}$$

$$\mathbf{\Lambda} = \operatorname{diag}(-\kappa, -t_{8,0}, -t_{8,0}, +\kappa, +t_{8,0}, +t_{8,0}) \ , \tag{3.15}$$

with

$$t_{1,0} = (\alpha \bar{u}_0 + \beta \bar{w}_0 - \omega) \ , \tag{3.16}$$

and

$$t_{8,0} = \sqrt{\kappa^2 + iRe \left(\alpha \bar{u}_0 + \beta \bar{w}_0 - \omega \right)} \ . \tag{3.17}$$

Two eigenvalues have a geometric and algebraic multiplicity of two. The free-stream base solutions have three eigensolutions which grow and three eigensolutions which decay in the free stream direction. Both, the growth rates as well as the decay rates differ considerably in their real part, which means that the system of equations is stiff. Note that four eigenfunctions

exhibit $z_5 = z_6 = 0$ and that two eigenfunctions exhibit $z_1 = z_2 = z_3 = z_4 = 0$. There eigenvalues directly correspond to the Orr-Sommerfeld, and the Squire equation, respectively. We use these eigenfunctions as base solutions.

Since we are interested in the disturbances inside the boundary layer, we require that the solution decays for $y \to \infty$. Hence the boundary condition at $y = y_{\max}$ is that the solution is in the space spanned by the eigenvectors of the k decaying base solutions. In the notation of equation (3.3) the matrix $\mathbf{C}$ contains the transposed vectors which are normal to the decaying eigenvectors.

3.3 Orthonormalization Procedure

When the k base solutions which decay toward the free stream are to be integrated numerically, it is necessary to set the direction of integration to be towards the wall. In this case the solutions amplify during the integration process, and numerical errors which are not in the linear space of the three solutions under consideration decay. However, numerical errors in the linear space of the strongly growing solutions are generated during the integration of the weakly growing solution. These errors then grow with the amplification rate of the strongly growing solution and spoil the integration of the weakly growing solution. This phenomenon is termed *parasitic error growth*.

The problem of parasitic error growth can be overcome by various approaches. The so-called *compound matrix method* (cf. Ng and Reid [48]) reformulates the problem to a new set of variables yielding a linear system of equations which is less prone to parasitic error growth but increases the numerical expense. In comparison to that, the so-called *Riccati method* (cf. Scott [56]) transforms the linear system of equations to a nonlinear (quadratic) system of equations which becomes singular during the integration process. This singularity can then be overcome, e.g., by integration in the complex plane.

For the current work we apply the approach of Godunov [27] and orthonormalize the base solutions in regular intervals by QR-decomposition.

This prevents the loss of linear independence of the base solutions. Numerically, this is implemented by the Gram-Schmid[1]procedure (e.g. [28]). This approach is computationally very efficient, when the k (i.e. two or three) base solutions are integrated. It is important to note that the base solutions in equation (3.4) can be chosen arbitrarily, as long as they are linearly independent. The orthonormalization essentially changes the linearly-independent solution base to a new unitary solution base. Conte [16] applies this approach to example equations and recommends checking the orthogonality of the base solutions using scalar products, and orthonormalize only when a certain margin is exceeded. Computations show that this margin is exceeded quite regularly, and that the calculation of the scalar products is almost as expensive as the Gram-Schmidt orthonormalization itself. Hence, it is cheaper to orthonormalize at fixed predetermined intervals than testing non-normality every step. Orthonormalizations every five integration steps for solving solely the Orr-Sommerfeld, and every two integration steps for solving the coupled Orr-Sommerfeld and Squire equation system provide good results.

We apply the incomplete Gram-Schmid orthonormalization

$$\mathbf{Y}_j = \mathbf{Q}_j \mathbf{R}_j \tag{3.18}$$

to obtain the unitary matrix $\mathbf{Q}_j$ and the upper triangular matrix $\mathbf{R}_j$. The unitary matrix $\mathbf{Q}_j$ replaces the matrix $\mathbf{Y}_j$ and the integration is continued. The upper triangular matrix $\mathbf{R}_j$ is only stored when the eigenfunction of the mode is to be calculated, otherwise it is discarded.

3.4 Wall Boundary Condition

In the shooting process, the base solutions are integrated toward the wall for a given set of the streamwise wavenumber α, spanwise wavenumber β, and angular frequency ω. Then it is tested if they can satisfy the boundary

---

[1]Throughout this work only the stable variant of the Gram-Schmid procedure is used, which is commonly referred to as the "modified Gram-Schmid" procedure.

condition at the wall (3.2). In the rigid wall case, we have the no-slip, no-penetration boundary condition

$$\mathbf{B} = \begin{bmatrix} 1 & 0 & 0 & 0 & 0 & 0 \\ 0 & 0 & 1 & 0 & 0 & 0 \\ 0 & 0 & 0 & 0 & 1 & 0 \end{bmatrix} \quad, \tag{3.19}$$

and in the compliant wall case, we have the dynamic-equilibrium, no-slip, and no-penetration boundary condition formulated in equations (2.23), (2.24), and (2.25). The resulting solution $\mathbf{z}$ is a superposition of the base solutions in $\mathbf{Y}$ with expansion coefficients $\mathbf{c}$

$$\mathbf{z} = \mathbf{Yc} \quad . \tag{3.20}$$

Inserted in (3.2) we require that

$$\mathbf{Kc} = \mathbf{0} \quad , \tag{3.21}$$

with

$$\mathbf{K} = \mathbf{BY}_1 \quad , \tag{3.22}$$

and

$$\mathbf{c} \neq \mathbf{0} \tag{3.23}$$

for the wall boundary condition to be satisfied. The determinant of $\mathbf{K}$ must be zero for this condition to be fulfilled.

We calculate the expansion coefficients of the base solutions $\mathbf{c}$ by choosing the coefficient c_k to be the (kk) minor[2] of $\mathbf{K}$, and determining the other coefficients using all but the last equation of (3.21). By this choice the residual $\epsilon(\alpha, \beta, \omega)$ of the last equation in (3.21) then is

$$\epsilon(\alpha, \beta, \omega) = \det(\mathbf{K}) \quad . \tag{3.24}$$

Depending on either the temporal model or the spatial model, the complex eigenvalues ω or α, respectively, are iterated so that $\epsilon = 0$. Arbitrary root finding methods for complex functions can be used to achieve this. However,

---

[2]The (ij) minor of $\mathbf{K}$ is the determinant of the $(k-1) \times (k-1)$ matrix formed by removing the i-th row and the j-th column of $\mathbf{K}$.

applying root finding methods to the residual in the present form shows poor convergence because the residual strongly varies its phase in the complex plane. To remedy this poor convergence, we scale the residual with the phase of the disturbance pressure at the wall. The disturbance pressure was chosen because it is the only quantity that is certainly unequal to zero for all modes but Squire-modes. This scaling improves the convergence of root finding methods significantly with the drawback that Squire-modes do not converge. However, Squire-modes are proven to be asymptotically stable at all times [59] and play no role in the asymptotic stability of the boundary layer, i.e., when transient growth is not of concern.

Fig. 3.1 shows a comparison of the residual in the complex phase speed plane with and without phase scaling for the Blasius boundary layer with parameters chosen by Mack [44, sect. 3], when solely the Orr-Sommerfeld equation is solved. Mack has used the intersections of the zero lines to determine the eigenvalues of the Orr-Sommerfeld equation. At the roots of the residual, the zero lines of the real and imaginary part intersect. In fig. 3.1(a), where the phase scaling was not applied, seven distinct intersections of the zero lines exist for phase speeds less than one, and several others exist for a phase speed of one. In the vicinity of the seven eigenvalues the residual phase varies clearly. Here a root finding algorithm converges only if the initial guess is close to the according eigenvalue. In contrast, fig. 3.1(b) displays the case with phase scaling. Here, the complex phase of the residual scarcely changes in the vicinity of the distinct eigenvalues, and initial guesses further away from the according eigenvalue converge. Note that intersections of zero lines do not necessarily mean that the residual is zero. This is visible for the continuous spectrum, i.e. for $c_r = 1$, and several distinct locations where phase scaling was applied. Also note that the zero lines of fig. 3.1(a) depend on the domain height. With increasing domain height, the number of zero lines in the viewport of this plot increases. Its number is also higher when the coupled Orr-Sommerfeld and Squire system is solved.
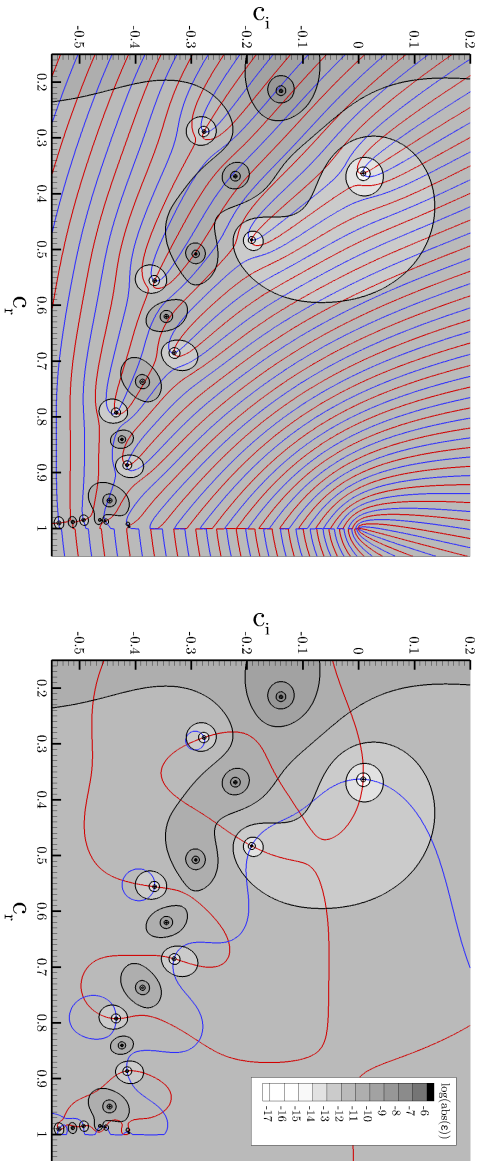
(a) without phase scaling

(b) with phase scaling

Figure 3.1 Comparison of the residual ϵ in the complex phase speed plane (c_r, c_i) for the Blasius boundary layer with $Re_{\delta_1} = 998$ and $\alpha = 3.0862 \times 10^{-4} U_\infty/\nu$. Shadings denote the magnitude of the residual, lines denote zero lines of the real and imaginary part: ——, $\Re(\epsilon) = 0$; ——, $\Im(\epsilon) = 0$.

3.5 Eigenvalue Iteration

The eigenvalue is iterated until the residual of the wall boundary condition and the last variation of the eigenvalue estimate are below the predefined limits

$$\epsilon < \epsilon_{\max} \qquad \wedge \qquad \left| \frac{\Delta \alpha \, \bar{u}_E}{\omega} \right| < c_{\max}^{(\alpha)} \qquad (3.25)$$

for the spatial case, and

$$\epsilon < \epsilon_{\max} \qquad \wedge \qquad \left| \frac{\Delta \omega}{\alpha \, \bar{u}_E} \right| < c_{\max}^{(\omega)} \qquad (3.26)$$

for the temporal case. For the current work diverse root finding methods were implemented:

Secant method To improve the eigenvalue estimate, the root of the secant through the last two functional values is used. Its order of convergence is 1.618. The secant method can be viewed as a variant of Newton's method[3], where the derivative of the function is approximated by the finite difference of the last two functional values. Therefore, the initial step size is chosen to be relatively small to ensure a good approximation of the derivative.

Muller's method An extension to the secant method with a convergence order of 1.839 is Muller's method [46]. The last three functional values are used to construct a parabola whose root is calculated to determine the next approximation. The numerical implementation of Press et.al. [50] is applied. To start this method the secant method is used to calculate the first three iterates.

Trust-region secant method For optimal robustness a trust-region secant method is used. The step size to the next iterate is restricted to stay within a given limit. If the residual has decreased in the last step the limit is increased by a preset factor, and otherwise decreased. Factors of 10 and 0.2, respectively, show rapid convergence and robustness.

---

[3]Indeed, in the literature of Orr-Sommerfeld shooting solvers this method is often termed Newton's method which suggests a convergence order of 2.0.

In the close vicinity of the root, this method converges as fast as the secant method.

"Trial-and-error" method The iterate is varied by a certain amount in the positive and negative direction of the real and imaginary axis. Only if the residual has reduced the new value is accepted. In case the residual cannot be reduced any more, we reduce the step size. This simple algorithm is computationally considerably more expensive than the other presented methods. On the other hand, it is robust and converges for Squire-modes because it does not depend on the phase of the residual.

The calculation of the stability diagram for a given instability mode, i.e., the values of $\omega(x_i, \alpha_j, \beta_k)$ for the temporal case, or the values of $\alpha(x_i, \omega_j, \beta_k)$ for the spatial case, is carried out in the following manner:

1. For the temporal or spatial framework, the user chooses the start point (x_i, α_j, β_k) or (x_i, ω_j, β_k) of the iteration and an initial guess for the eigenvalue ω_{start} or α_{start}, respectively.

2. The first eigenvalue at the start point is iterated using the trust-region secant method, because of its high robustness.

3. α_j or ω_j is increased successively with the eigenvalue previously found as the initial guess for the next iteration. After that the same procedure is carried out with decreasing α_j or ω_j. Here, Muller's method is used, because of its fast convergence.

4. Starting from the converged eigenvalues, β_k is increased and decreased successively with initial guesses of the previously converged eigenvalues.

5. Likewise, the streamwise location x_i is increased and decreased successively.

During this process, the initial guesses for the shooting method are improved by first-order approximation of the eigenvalue gradient with respect to the

parameter which was increased or decreased. To ensure computational efficiency the number of iterations per point is limited. In case the iteration was not successful at a certain point, an intermediate point is calculated between the grid points to improve the initial guess for the next point. The calculation of the eigenvalue at intermediate points is successively refined up to a given recursion depth. Hereby, the baseflow profile $\bar{u}(y)$ and $\bar{w}(y)$ at intermediate points is linearly interpolated.

3.6 Calculation of the Eigenfunction

In some cases, not only the amplification rate of an instability mode, but also the eigenfunction is of interest. Then the eigenvalue is first iterated until the conditions (3.25) or (3.26) are fulfilled. At the wall, the expansion coefficients of the base solutions $\mathbf{c}_1$ are determined as described in section 3.4, and then successively determined towards the free stream. At the locations where an orthonormalization was performed, the expansion coefficients must be transformed to the next set of base solutions using backsubstitution (cf. Scott [57])

$$\mathbf{R}_j \mathbf{c}_{j+1} = \mathbf{c}_j \ .$$ (3.27)

At locations where no orthonormalization was performed the coefficients are kept constant $\mathbf{c}_{j+1} = \mathbf{c}_j$. The final solution is then calculated by

$$\mathbf{z}_j = \mathbf{Y}_j \mathbf{c}_j \ .$$ (3.28)

In case one needs the values of the eigenfunction at some location $y > y_{\max}$, then it is feasible to determine the function of the eigensolution analytically. When the expansion coefficients of the base solutions at $y_{\max}$ have been discarded, then one can recalculate the expansion coefficients of the decaying eigensolutions in (3.13) by a least-squares approximation. We write

the decaying eigensolutions of (3.14) in the columns of a matrix

$$
\hat{\mathbf{S}} = \begin{bmatrix}
1 & t_{8,0} & 0 \\
\mp\kappa & \mp t_{8,0}^2 & 0 \\
\pm i\kappa^{-1} & \pm i & 0 \\
-t_{1,0}\kappa^{-2} & 0 & 0 \\
0 & 0 & 1 \\
0 & 0 & \pm t_{8,0}
\end{bmatrix} ,
\tag{3.29}
$$

orthogonalize it

$$
\hat{\mathbf{S}} = \hat{\mathbf{Q}}\hat{\mathbf{R}} ,
\tag{3.30}
$$

and solve for the coefficients $\mathbf{c}$ in

$$
\hat{\mathbf{R}}\mathbf{c} = \hat{\mathbf{Q}}^H \mathbf{z}_{N_p}
\tag{3.31}
$$

using backsubstitution.

3.7 Numerical Accuracy of the Shooting Solver

Table 3.1 lists the computed eigenvalues for the parameters used in fig. 3.1. The significant digits were determined by a grid study. The values are in excellent agreement with Mack [44]. Differences only appear in the fourth digit after the decimal point. These could be caused by small differences in the streamwise wavenumber α. Note that all values behind the second digit are of purely academic interest, because of the assumptions involved in the derivation of the solved equations.

Fig. 3.2 shows a grid study for the TS eigenvalue of the Blasius boundary layer. The relative deviation to the solution calculated on the finest grid is plotted over the grid spacing. A grid convergence of fourth order is clearly visible. For increasing resolution, the relative deviation of the eigenvalue does not decrease any further than 10^{-12} due to round-off errors. Note that the maximum achievable accuracy is dependent on the eigenvalue under consideration. For the given parameters the other eigenvalues in the spectrum converge at least to a relative deviation of 10^{-9}.

Table 3.1 Temporal eigenvalues of the Blasius boundary layer with $Re_{\delta_1} = 998$ and $\alpha = 3.0862 \times 10^{-4} U_\infty / \nu$.

mode	c_r / U_∞	c_i / U_∞
1	0.3641218582633	0.0079621468973
2	0.2897238514584	-0.2768735025583
3	0.483943169789	-0.192081324334
4	0.55721993015	-0.36535103558
5	0.68628627708	-0.33078484801
6	0.793685627	-0.434097786
7	0.887406422	-0.414760019

Expedient resolutions are in the order of 100 grid points within the boundary layer under investigation ($\Delta y / \delta_1 \approx 0.03$). Certainly, higher resolutions result in a higher accuracy, but due to the assumption of local parallelism, differences to, e.g., direct numerical simulations are in general larger than the numerical inaccuracy of the eigenvalue determination.
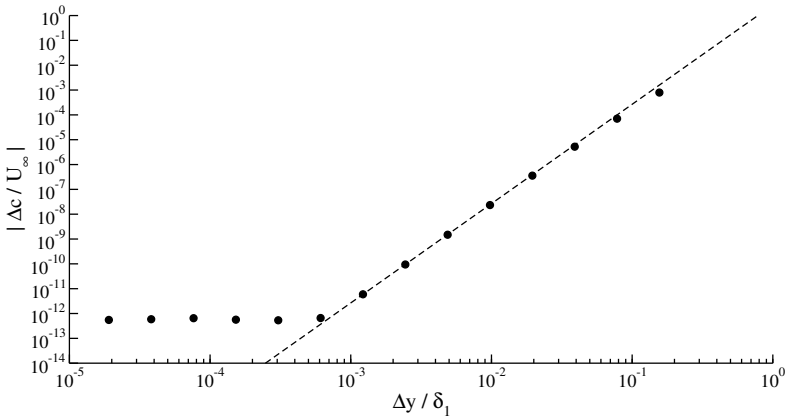
Figure 3.2 Numerical error versus wall-normal grid spacing for the calculation of the temporal TS eigenvalue with $Re_{\delta_1} = 998$, $\alpha = 3.0862 \times 10^{-4} U_\infty / \nu$ and $y_{\max} / \delta_1 = 20$. The dashed line displays 4th-order convergence.

4 Matrix Solver

> Pseudospectral algorithms are simply N$^{\text{th}}$ order finite differences in disguise.
>
> *John P. Boyd*

Depending on the temporal or the spatial case, the Orr-Sommerfeld and Squire equation constitute a generalized eigenvalue problem with the eigenvalue ω or a polynomial generalized eigenvalue problem of fourth order [18] with the eigenvalue α, respectively. By coordinate transformation, the spatial Orr-Sommerfeld problem can be reduced to a quadratic eigenvalue problem [33]. In general the compliant-wall boundary conditions theirself imply a quadratic eigenvalue problem in the temporal case, and a polynomial eigenvalue problem of sixth order in the spatial case. In the present work the *temporal eigenvalue spectrum* is solved using a so-called matrix solver.

We choose to solve the Orr-Sommerfeld and the Squire equation in the formulation of eq. (B.25) and eq. (B.26). These can be written in their discretized form as

$$\mathbf{A}\mathbf{x}_i = \omega_i \mathbf{B}\mathbf{x}_i \ , \tag{4.1a}$$

$$\text{or} \quad \mathbf{A}\mathbf{X} = \text{diag}(\boldsymbol{\omega})\,\mathbf{B}\mathbf{X} \ , \tag{4.1b}$$

with the generalized eigenvectors $\mathbf{x}_i$ and their according generalized eigenvalues ω_i, or the matrix $\mathbf{X}$ containing the generalized eigenvectors in columns and the vector $\boldsymbol{\omega}$ containing the according generalized eigenvalues. The eigenvalues are the complex wavenumber, whose real part is the disturbance frequency, and whose imaginary part is the temporal amplification rate. We solve this eigenvalue problem by QZ-decomposition (cf. Golub and Van Loan [28]) using LAPACK routines [1] to obtain the full eigenvalue spectrum.

In this chapter the method of discretization, computational domain and coordinate mapping is presented. The formulation of boundary conditions,

and the implementation of the generalized eigenvalue problem as well as the numerical quadrature of the eigenfunctions is elucidated. Finally, the effects of compliant walls on eigenspectra and the numerical accuracy of the matrix scheme is scrutinized.

4.1 Discretization

For the current application spectral methods have the advantage of a high accuracy for a given degree of freedom. However, high-resolution spectral calculations have a tendency to be spoiled by round-off errors. So the numerical implementation of the differentiation must be directed towards low round-off errors and numerical stability. The equations are discretized using *pseudospectral Chebyshev collocation*. We approximate a function by its values at the N_c Chebyshev-Gauß-Lobatto points

$$\check{y}_i = \cos\left(\frac{N_c - i}{N_c - 1}\pi\right) \qquad i = 1, \dots, N_c \ . \tag{4.2}$$

For this point distribution the interpolation error is particularly small [24]. We discretize the mth derivative using a differentiation matrix $\mathbf{D}^{(m)}$. Elaborate tests have shown that the recursion formula for off-diagonal elements [67]

$$\check{D}_{ij}^{(m)} = \frac{m}{\check{y}_i - \check{y}_j}\left(\frac{w_j}{w_i}\check{D}_{ii}^{(m-1)} - \check{D}_{ij}^{(m-1)}\right) \ , \tag{4.3}$$

in combination with the *negative-sum trick* [2]

$$\check{D}_{ii}^{(m)} = -\sum_{\substack{j=1 \\ j \neq i}}^{N_c} \check{D}_{ij}^{(m)} \tag{4.4}$$

reduce the round-off errors of differentiation considerably. Hereby,

$$w_i = \frac{1}{\prod_{k \neq i}(\check{y}_i - \check{y}_k)} \qquad i = 1, \dots, N_c \tag{4.5}$$

are the barycentric weights (cf. Berrut [7]) of the collocation points. Indeed this type of differentiation is a finite difference in disguise—the entries of the differentiation matrix are the weights of a finite-difference stencil spanned

over all collocation points. These stencils could be calculated using the Fornberg algorithm [23], but at a much higher computational cost.

4.2 Computational Domain and Coordinate Mapping

The stability equations of the flow within a boundary layer can either be solved in a finite interval (domain truncation) or in a semi-infinite domain by coordinate mapping to infinity. The distance between the collocation points increases successively towards the free-stream when the equations are mapped to a semi-infinite domain, so that at some point oscillations of the eigenfunction can not be properly resolved any further due to aliasing. Grosch and Orszag [30] inter alia compared domain truncation, exponential mapping, and algebraic mapping for the Tollmien-Schlichting eigenvalue of the Orr-Sommerfeld equation. They concluded that results using the algebraic mapping are superior in this case, but also stated that mapping to infinity fails for solutions that oscillate towards infinity. Since the matrix solver is also supposed to resolve the continuous spectrum which exhibits oscillations towards infinity, we use domain truncation.

We truncate the domain to the interval $y \in [0, y_{\max}]$, and use the rational map

$$y = f(\tilde{y}) = \frac{y_m y_{\max}(\tilde{y} + 1)}{\tilde{y}(2y_m - y_{\max}) + y_{\max}} \tag{4.6}$$

pointed out in Schmid and Henningson [55, Appendix A.4]. Hereby, the points are distributed so that half of the points are above and below $y = y_m$. This map allows to concentrate points in the boundary layer, e.g., by choosing $y_m = \delta_{99}$, to resolve particular eigenvalues better. In the light of basis functions, polynomials in $\tilde{y}$ become rational polynomials in y for $y_m \neq y_{\max}/2$. However, the full eigenvalue spectrum is resolved best when $y_m = y_{\max}/2$. In this case the mapping becomes a linear mapping which preserves the behavior of the basis functions.

Numerically, the coordinate mapping is implemented by transformation of the differentiation matrices using the equations

$$D_{ij}^{(1)} = f_1(\tilde{y}_j)^{-1} \check{D}_{ij}^{(1)} \ , \tag{4.7}$$

$$D_{ij}^{(2)} = f_1(\check{y}_j)^{-3} \left(f_1(\check{y}_j)\check{D}_{ij}^{(2)} - f_2(\check{y}_j)\check{D}_{ij}^{(1)} \right) \quad, \tag{4.8}$$

$$D_{ij}^{(3)} = f_1(\check{y}_j)^{-5} \left(f_1^2(\check{y}_j)\check{D}_{ij}^{(3)} - 3f_2(\check{y}_j)f_1(\check{y}_j)\check{D}_{ij}^{(2)} + \right.$$
$$\left. + \left(-f_3(\check{y}_j)f_1(\check{y}_j) + 3f_2^2(\check{y}_j) \right) \check{D}_{ij}^{(1)} \right) \quad, \tag{4.9}$$

and

$$D_{ij}^{(4)} = f_1(\check{y}_j)^{-7} \left(f_1^3(\check{y}_j)\check{D}_{ij}^{(4)} - 6f_2(\check{y}_j)f_1^2(\check{y}_j)\check{D}_{ij}^{(3)} \right.$$
$$+ \left(-4f_3(\check{y}_j)f_1^2(\check{y}_j) + 15f_2^2(\check{y}_j)f_1(\check{y}_j) \right) \check{D}_{ij}^{(2)}$$
$$\left. + \left(-f_4(\check{y}_j)f_1^2(\check{y}_j) + 10f_3(\check{y}_j)f_2(\check{y}_j)f_1(\check{y}_j) - 15f_2^3(\check{y}_j) \right) \check{D}_{ij}^{(1)} \right) \quad, \tag{4.10}$$

given by Boyd [8, Appendix E] with $f_m = \partial^m f/\partial\check{y}^m$.

4.3 Formulation of Boundary Conditions

At the wall we have the no-slip, no-penetration boundary conditions, as well as the dynamic equilibrium in the case of a compliant wall. At the free-stream boundary of the truncated domain we require the wall-normal velocity $\tilde{v}$ to exhibit an exponential decay with the (inviscid) decay rate of $\exp(-\kappa y)$, and the wall-normal vorticity $\tilde{\Omega}$ to be zero. This can be justified when the domain height is large enough so that the magnitude of the base solution of equation (3.13) that decays with the (viscous) decay rate of $\exp(-\sqrt{\kappa^2 + iRe\,(\alpha\bar{u}_0 + \beta\bar{w}_0 - \omega)}\,y)$ becomes negligibly small with respect to the inviscid decay rate. The exponential decay of the disturbance-velocity components can be expressed as

$$\mathcal{D}^2\tilde{v} + \kappa\mathcal{D}\tilde{v} = 0 \tag{4.11}$$

$$\mathcal{D}\tilde{v} + \kappa\tilde{v} = 0 \tag{4.12}$$

$$\tilde{\Omega} = 0 \ . \tag{4.13}$$

These equations do not contain the eigenvalue ω, so we introduce the predefined complex parameter μ (cf. Schmid [55, sect. A.5]) and write the equations in the form

$$\mu\left(\mathcal{D}^2\tilde{v} + \kappa\mathcal{D}\tilde{v}\right) = \omega\left(\mathcal{D}^2\tilde{v} + \kappa\mathcal{D}\tilde{v}\right) \tag{4.14}$$

$$\mu \left(\mathcal{D}\tilde{v} + \kappa \tilde{v} \right) = \omega \left(\mathcal{D}\tilde{v} + \kappa \tilde{v} \right) \tag{4.15}$$

$$\mu \tilde{\Omega} = \omega \tilde{\Omega} \ . \tag{4.16}$$

This approach maps the spurious eigenvalue associated with the boundary condition to the location of μ in the complex plane. It is evident that the eigenfunction of an eigenvalue $\omega \neq \mu$ must fulfill equations (4.11)-(4.13), and that the (spurious) eigenvalues $\omega = \mu$ must be removed from the result, because they generally do not satisfy the boundary conditions.

4.4 Implementation of the Generalized Eigenvalue Problem

Since the solution of a generalized eigenvalue problem has a numerical cost of $\mathcal{O}(N^3)$, we minimize the size of the solution vector $\mathbf{x}$ by choosing the formulation of equations(B.25) and (B.26). So for a given number of N_c collocation points y_j, the values of $\tilde{v}_j$ and $\tilde{\Omega}_j$ at these locations are unknowns and are to be calculated. The boundary condition represented by equation (2.32) implicitly poses a quadratic eigenvalue problem of ω which becomes visible if the unknown $\tilde{\eta}$ is replaced using equation (2.34). This quadratic eigenvalue problem can be overcome by increasing the size of the problem and, introducing another variable that is equal to $(\omega \tilde{v}_1)$(cf. Tisseur [61]). To keep our equations related to the physical problem we use the variable $\tilde{\eta} = i\tilde{v}/\omega$, which also has the effect of removing the quadratic term in ω. Hence, the solution vector contains $2N_c + 1$ elements. We define it as

$$\mathbf{x} = \left(\tilde{\mathbf{v}}^T, \tilde{\mathbf{\Omega}}^T, \tilde{\eta} \right)^T \ . \tag{4.17}$$

Note that the quadratic term in ω appears only in one boundary condition so that only an additional scalar and not an additional vector is introduced.

We require the Orr-Sommerfeld equation (B.25) to be satisfied at the collocation points except for two points at the wall and two points at the free-stream boundary, where the four boundary conditions (2.30), (2.32), (4.14), and (4.15) must be satisfied. Analogously, we require the Squire equation (B.26) to be satisfied at the collocation points except for the wall and free-stream boundary, where the boundary conditions (2.31) and (4.16) must

be satisfied. Finally, we require the definition of $\tilde{\eta}$, equation (2.34), to be satisfied. Upon discretization, the derivative operator $\mathcal{D}^m$ is replaced by the differentiation matrix $\mathbf{D}^{(m)}$ (cf. sect. 4.1) so that the contents of the matrices $\mathbf{A}$ and $\mathbf{B}$ in equation (4.1) are straightforward to fill, which is documented in Appendix C.

4.5 Numerical Quadrature of the Eigenfunctions

For post-processing of the eigenfunctions, e.g. for the calculation of their disturbance energy, a method of numerical integration is needed (cf. eqn. (6.1)). This method must have positive non-zero integration weights for all grid points to ensure that the energy given by equation (6.3) is positive for all non-zero eigenvectors. For that reason it was chosen to use Clenshaw-Curtis quadrature weights $\breve{w}_{cc,j}$ to approximate the integral of a function $g(\breve{y})$ over the computational domain as

$$\int_{-1}^{1} g(\breve{y})dx \approx \sum_{j=1}^{N_c} \breve{w}_{cc,j} g(\breve{y}_j) \ . \tag{4.18}$$

These weights are calculated by [63]

$$\breve{w}_{cc,1} = \breve{w}_{cc,N_c} = \begin{cases} \frac{1}{(N_c-1)^2-1} & \text{if } N_c \text{ odd,} \\ \frac{1}{(N_c-1)^2} & \text{if } N_c \text{ even,} \end{cases} \tag{4.19}$$

and

$$\breve{w}_{cc,j} = \begin{cases} \frac{2}{N_c-1}\left(1 - \frac{\cos((j-1)\pi)}{(N_c-1)^2-1} - \sum_{k=1}^{\frac{N_c-3}{2}} \frac{2\cos\left(2k\frac{N_c-j}{N_c-1}\pi\right)}{4k^2-1}\right) & \text{if } N_c \text{ odd,} \\ \frac{2}{N_c-1}\left(1 - \sum_{k=1}^{\frac{N_c-2}{2}} \frac{2\cos\left(2k\frac{N_c-j}{N_c-1}\pi\right)}{4k^2-1}\right) & \text{if } N_c \text{ even.} \end{cases} \tag{4.20}$$

Analogous to the mapping of the differentiation matrices, the integration weights are mapped by

$$\breve{w}_{cc,j} = f_1(\breve{y}_j)\breve{w}_{cc,j} \ . \tag{4.21}$$

To integrate to infinity we make use of the decay boundary condition at the truncated domain. A disturbance quantity $\tilde{\varphi}$ decays exponentially at $y > y_{\max}$ with $\tilde{\varphi} \sim \exp(-\kappa y)$ so we can write it as

$$\tilde{\varphi}(y) = \tilde{\varphi}(y_{\max})\, e^{-\kappa(y - y_{\max})} \quad . \tag{4.22}$$

Analytically, we obtain

$$\int_{y_{\max}}^{\infty} \tilde{\varphi}(y)^* \, \tilde{\varphi}(y)\, dy = \frac{1}{\mathrm{abs}(2\kappa)} \tilde{\varphi}(y_{\max})^* \, \tilde{\varphi}(y_{\max}) \tag{4.23}$$

for $\alpha_i = \beta_i = 0$, so we can increase the integration weight $\breve{w}_{cc,N_c}$ by $1/\mathrm{abs}(2\kappa)$ and get

$$\int_0^{\infty} \tilde{\varphi}(y)^* \, \tilde{\varphi}(y)\, dy \approx \sum_{j=1}^{N_c} w_{cc,j}\, \tilde{\varphi}(y_j)^* \, \tilde{\varphi}(y_j) \quad , \tag{4.24}$$

with

$$w_{cc,j} = \begin{cases} \breve{w}_{cc,j} & \text{if } j < N_c, \\ \breve{w}_{cc,j} + \frac{1}{\mathrm{abs}(2\kappa)} & \text{if } j = N_c. \end{cases} \tag{4.25}$$

4.6 Effect of Compliant Walls on Eigenvalue Spectra

The temporal eigenvalue spectrum of the Orr-Sommerfeld and Squire equation for the Blasius boundary layer is plotted in fig. 4.1 for the parameters investigated by Mack [44]. The spectrum was calculated using the matrix solver. In a second step the obtained eigenvalues were used as the initial guess for the shooting solver. Open symbols are the eigenvalues obtained by the matrix method and filled symbols are the eigenvalues for which the shooting solver also converges. The eigenvalue number 1 is the Tollmien-Schlichting eigenvalue. The eigenvalues with the numbers 2-7 are further eigenvalues resulting from the Orr-Sommerfeld equation. In between these eigenvalues are the so-called Squire-modes, which are characterized by a wall-normal velocity equal to zero. These modes are not present when the Orr-Sommerfeld equation is solved solely. The shooting solver does not converge for these eigenvalues, due to the implementation of the boundary
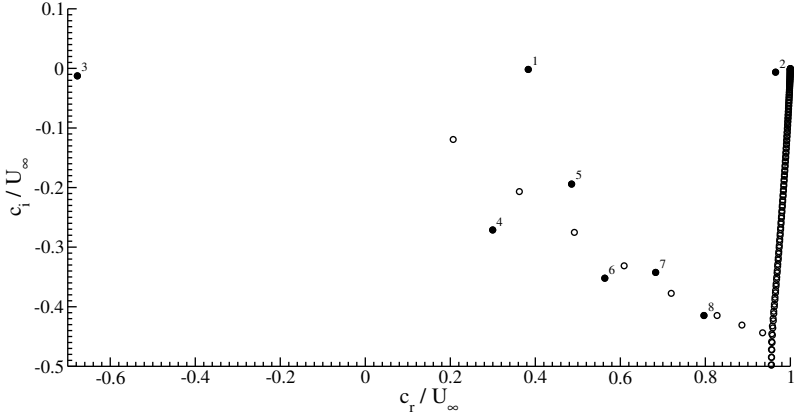
condition at the wall (cf. sect. 3.4). The continuous spectrum is located at $c_r = 1$ and is represented as a line of discrete eigenvalues due to the discretization. The deviation of the continuous spectrum to lower phase speeds can be explained with numerical errors, since it is dependent on discretization.

Figure 4.1 Temporal eigenvalue spectrum of the Blasius BL over a rigid surface for $Re_{\delta_1} = 998$, $\alpha = 3.0862 \times 10^{-4} U_\infty/\nu$ and $y_{\max}/\delta_1 = 20$. Filled symbols denote discrete eigenvalues for which the shooting solver converges.

Two additional eigenvalues, the FISI modes, typically appear when the rigid wall is replaced by a compliant wall. In fig. 4.2 an eigenvalue spectrum is plotted for the same parameters as before, but with an anisotropic compliant wall (parameter set 2, cf. app. A). Now, the TS eigenvalue, eigenvalue 1, is stable. The FISI modes are eigenvalue 2, with a positive phase speed, and the eigenvalue 3, with a negative phase speed. Both FISI modes can exhibit phase speeds larger or smaller than $\pm U_\infty$. These two modes are characterized by maximum disturbance velocities at the wall and a decay towards the free-stream.

Figure 4.2 Temporal eigenvalue spectrum of the Blasius BL over the aniso-
tropic compliant surface, case 2, for $Re_{\delta_1} = 998$, $\alpha = 3.0862 \times 10^{-4} U_\infty/\nu$
and $y_{\max}/\delta_1 = 20$. Filled symbols denote discrete eigenvalues for which
the shooting solver converges.

4.7 Numerical Accuracy of the Matrix Scheme

When computing the numerical solution of the stability equations the ques-
tion of the achieved numerical accuracy must be faced. Commonly, accuracy
considerations are restricted to a review of the discretization error. For
large, increasing resolution (degrees of freedom) this error typically decays
algebraically for finite-difference schemes, and geometrically for spectral
methods. When increasing the resolution further than a certain point round-
off errors become noticeable. Two effects of these round-off errors can be
observed. On one hand, the equation of the eigenvalue problem is disturbed
by the *representation error* which occurs when noting the matrices **A** and **B**
in floating point numbers. On the other hand, the calculation of the ma-
trices is furthermore disturbed by *round-off errors* during the calculation of
the pseudospectral differentiation matrices. These errors incurred by cal-
culating derivatives using Chebyshev polynomials have been investigated
by Breuer [10] and grow algebraically with increasing numerical order, i.e.

collocation points.

In fig. 4.3 a grid convergence study of the matrix method is shown for the eigenvalues plotted in fig. 4.1. Hereby the Orr-Sommerfeld and Squire equation system is solved. For this study the eigenvalue spectrum was calculated with different resolutions, i.e. number of collocation points. The eigenvalue was compared to the result with the next larger and the next smaller resolution and the smallest delta in phase speed is plotted over the number of collocation points N_c. A geometric convergence of the matrix method is visible for resolutions up to 120 to 160 collocation points, depending on the eigenvalue. For higher resolutions the error remains at a small plateau, and then increases again. There exists an optimal resolution for each eigenvalue where the numerical errors are minimal. For the current parameters a resolution of 200 collocation points is optimal for all discrete eigenvalues shown. However for this resolution, the TS eigenvalue is predominantly affected by round off errors, while the eigenvalue number 6 is approximately equally affected by discretization and round off errors.
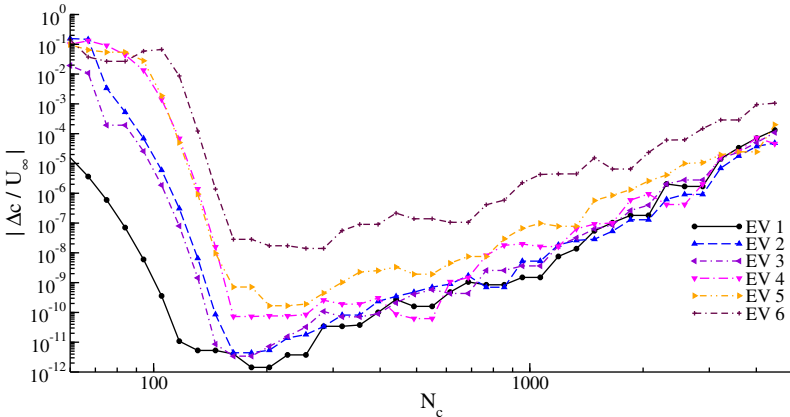

Figure 4.3 Grid convergence study of the matrix method for the eigenvalue spectrum of the Blasius BL over a rigid surface for $Re_{\delta_1} = 998$, $\alpha = 3.0862 \times 10^{-4} U_\infty / \nu$ and $y_{\max}/\delta_1 = 20$. Eigenvalue numbers correspond to fig. 4.1.

In fig. 4.4 the same grid convergence study is shown for the anisotropic compliant wall, case 2, for the eigenvalues plotted in fig. 4.2. Again a geometric convergence of the matrix method is visible—in this case for resolutions up to 105 to 145 collocation points, depending on the eigenvalue. For higher resolutions the numerical error forms a plateau. When the resolution is further increased the numerical error rises again. Again we can see that an optimal resolution exits for all discrete eigenvalues. Here a resolution of 160 collocation points minimizes the largest numerical error of the shown discrete eigenvalues.
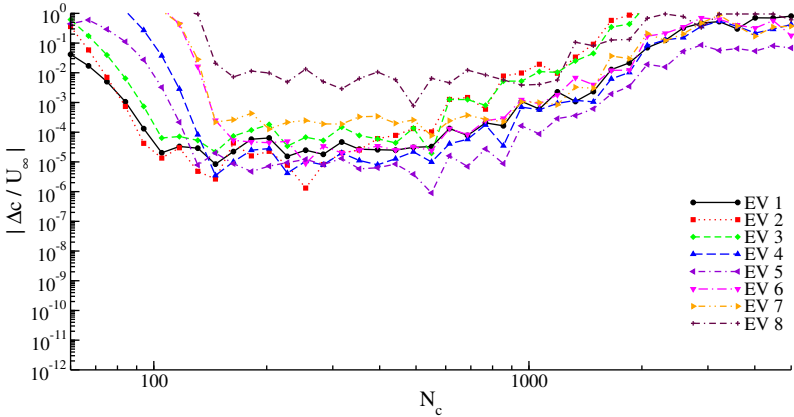
Figure 4.4 Grid convergence study of the matrix method for the eigenvalue spectrum of the Blasius BL over the anisotropic compliant surface, case 2, for $Re_{\delta_1} = 998$, $\alpha = 3.0862 \times 10^{-4} U_\infty/\nu$ and $y_{\max}/\delta_1 = 20$. Eigenvalue numbers correspond to fig. 4.2.

Note that a different behavior can be seen with respect to numerical errors, depending on the individual eigenvalue. This can be seen for the rigid and the compliant wall case. Due to the non-orthogonality of the eigenvectors, the associated eigenvalues some eigenvalues are more prone to round-off errors of the stability matrices than others. Their sensitivity to errors in the matrices is addressed by Reddy [51] and Trefethen [65] and can be visualized by calculating the ϵ-pseudospetrum of the generalized eigenvalue problem.

To evaluate these ϵ-pseudospectra, we calculate the resolvent energy norm

$$\left\| \left(z - \mathbf{B}^{-1}\mathbf{A} \right)^{-1} \right\|_E = \sigma_{\min} \left(\mathbf{F} \left(z - \mathbf{B}^{-1}\mathbf{A} \right) \mathbf{F}^{-1} \right) \tag{4.26}$$

on a computational grid in the complex plane and evaluate its contours. Hereby, we use the energy norm, which is defined in sec. 6.1 and calculate the smallest singular value $\sigma_{\min}$ by SVD. More elaborate ways of computing pseudospectra can be found in Trefethen [62].

Fig. 4.5 shows contour plots of the resolvent energy norm for the rigid wall, calculated by using 400, 300 and 250 collocation points. Also plotted is the eigenvalue spectrum calculated by the matrix solver. The ϵ-pseudospectra of different resolutions are only congruent in a dedicated region. Depending
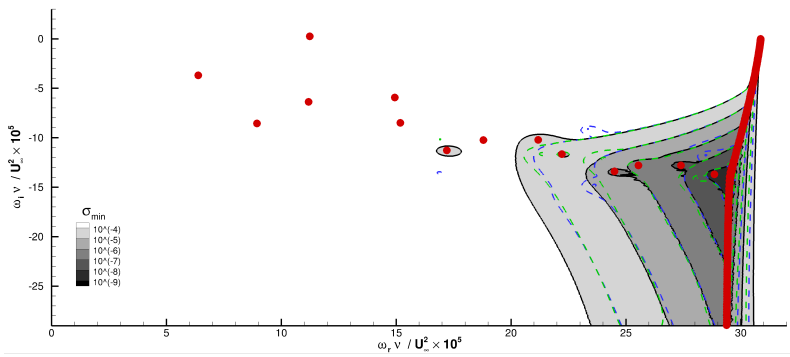
Figure 4.5 Resolvent energy norm for the Blasius BL over a rigid surface, for $Re_{\delta_1} = 998$, $\alpha = 3.0862 \times 10^{-4} U_\infty/\nu$ and $y_{\max}/\delta_1 = 20$. Contours and black lines were calculated with $N_c = 400$, dashed blue and green lines were calculated with $N_c = 300$ and $N_c = 250$, respectively. Red dots denote eigenvalues.

on the level of the contour lines, deviations between the different resolutions can ben seen. Contour lines exhibit bulges for one resolution, but not for the others. Due to the dependence of the results on the number of collocation points, a quantitative judgment cannot be made. Merely increasing the number of collocation points further is not helpful here. However, from qualitative perspective, we can conclude that that the discrete eigenvalues

which are closer to the continuous spectrum are more prone to round-off errors. This corresponds to the plateaus of the computed errors in fig. 4.3 and explains the fact that certain eigenvalues can only be computed up to a certain precision.

In fig. 4.6 the according resolvent energy norm for the compliant wall, case 2, and the eigenvalues are plotted. Here, we can also see deviations
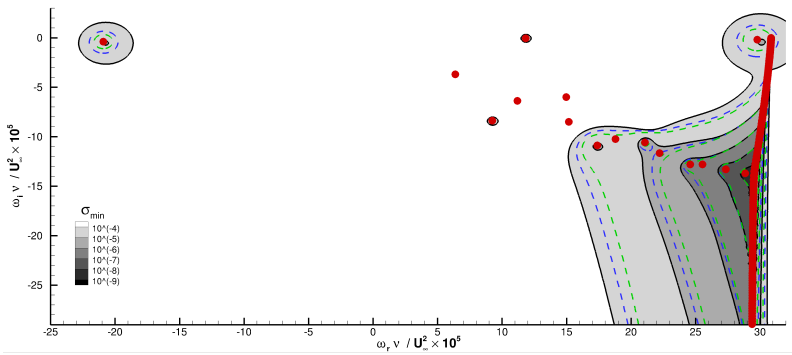
Figure 4.6 Resolvent energy norm for the Blasius BL over compliant surface, case 2, for $Re_{\delta_1} = 998$, $\alpha = 3.0862 \times 10^{-4} U_\infty/\nu$ and $y_{\max}/\delta_1 = 20$. Contours and black lines were calculated with $N_c = 400$, dashed blue and green lines were calculated with $N_c = 300$ and $N_c = 250$, respectively. Red dots denote eigenvalues.

between the contours generated with different resolution. Again, the ϵ-pseudospectrum qualitatively corresponds to the computed errors in fig. 4.4 and explains the fact that certain eigenvalues can only be computed up to a certain precision.

The convergency study shows that round-off errors affect the solution of the compliant-wall spectra by orders of magnitude larger than for the rigid wall case. Various methods of discretization, formulation of the equations, and implementations for calculation of the differentiation matrices were tried to find out that the method described in this thesis works best for the calculation of the eigenspectra of the coupled Orr-Sommerfeld and Squire

equation for external flows over anisotropic compliant walls. During the development of the numerical solver, it turned out that some implementations just could not accomplish the needed accuracy. For some implementations it was not possible to calculate the eigenvalue 8, because, depending on the resolution, either the numerical error or the discretization error were in the order of the exact value.

In conclusion we find that the formulation of the problem, numerical scheme and implementation are crucial for solving the undelying problem. Even though a suitable scheme was found, some investigations, such as the global calculation of ϵ-pseudospectra cannot be performed. In the following, all results generated by the matrix scheme were either validated by the shooting solver or by a second calculation with a different number of collocation points was performed to ensure grid-independence.

5 Yawing of the Anisotropic Compliant Wall

> A computation is a temptation that should be resisted as long as possible.
>
> *J. P. Boyd, paraphrasing T. S. Eliot*

5.1 The Dolphins' Inspiration

Previous investigators, e.g., Carpenter [15] and Yeo [68], have restricted their investigations to the case where the flow direction is perpendicular to the stiffeners of the compliant wall. Hereby, Carpenter [15] published a method to optimize compliant-wall parameters of his anisotropic compliant wall model for minimal growth of the TS mode and marginal stability of the FISI modes. It leaves one open parameter which can be varied to account for the optimization with respect to a specific e^N-Factor. Also, it needs a certain downstream-location to optimize for, so it is based on local optimization. These investigators however used solely two-dimensional approaches and did not account for three-dimensional modes.

Pavlov [49] investigated the skin properties of harbor porpoises and showed that the dermal ridges—these are comparable to the stiffeners of the anisotropic compliant wall model—are aligned in lines and make an angle (yawing) to the local flow direction. In fig. 5.1 is a visualization of the local flow direction (color scaled) and alignment of the dermal ridges (in brown) taken from Pavlov [49] (with permission of the author). This leads to the question, whether yawing of the anisotropic compliant wall with respect to the flow direction can be beneficial for transition delay.

Zengl and Rist [71] investigated the effect of compliant-wall yawing on the temporal stability of the Blasius boundary layer up to $Re_x = 3.0 \times 10^6$. They concluded that an increasing yaw angle of the anisotropic compliant wall moves the propagation direction of the least stable TS mode to oblique-traveling waves, while the least stable FISI mode is moved in the opposite
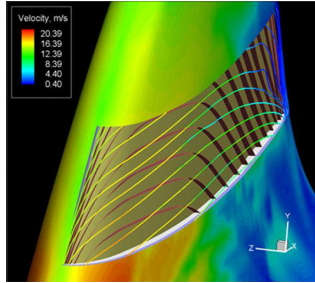
Figure 5.1 Visualization of the flow field over the dorsal fin, and the alignment of the dermal ridges of a harbor porpoise (source [49]).

direction. The TS mode is slightly stabilized and a FISI mode is destabilized by yawing of the wall. In the computational box it appears that a FISI mode becomes unstable at a yaw angle between $\psi = 36°$ and $\psi = 54°$ for compliant wall parameter set 2 (cf. app. A).

What remains unclear is the effect of yawing on the predicted transition location. This topic is addressed in this chapter and is based on three-dimensional spatial and temporal linear stability investigations of the wall parameter set 2 and 3 with Reynolds numbers up to $Re_x = 3.9 \times 10^7$. With this choice of the computational domain e^N-calculations were carried out up to $N > 10$, which is more than enough to predict the transition location for realistic disturbance environments. Spanwise-traveling waves were taken into account by variation of the real part of the spanwise wavenumber β, while its imaginary part was set to zero. The step width of the yaw angles was refined to $\Delta\psi = 5°$ in order to narrow the region of ψ in which the FISI mode becomes unstable. As a reference and introduction to the reader three-dimensional linear stability diagrams of the Blasius boundary layer over a rigid wall are presented.

In this chapter two sets of anisotropic compliant wall parameters published by Carpenter [15] where adopted. These are listed in app. A and correspond to dimensional values in [15, Table 2]. These parameters have the advantage that results with these parameters are available for comparison, and that marginal stability of the FISI modes in the three-dimensional

case and for yaw angles up to a certain yaw angle has been shown. Concerning the question whether these are "optimal parameters", they are at least in a region where approximately a four-fold transition delay can be demonstrated, which will be shown later in this chapter.

5.2 Three-Dimensional Linear Stability Diagrams for the Rigid Wall

With our linear stability calculations we solve the dispersion relation $D(Re_x, \alpha, \beta, \omega) = 0$. Hereby, Re_x is equivalent to $U(y)$ and/or $W(y)$. In the temporal problem we vary the parameters (Re_x, α, β) and solve for ω_r and ω_i. Note that the wavenumbers are scaled with U_∞/ν in contrast to the scale of δ_1 which is frequently found in literature. A temporal linear stability diagram of the Blasius boundary layer over a rigid wall is shown in fig. 5.2. Only the unstable region of the eigenvalues, i.e. $\omega_i > 0$, is shown. A translucent isosurface of neutral stability is plotted in gray. Neutral stability lines are plotted for constant values of β with a spacing of $\Delta\beta = 2.5 \times 10^{-5} U_\infty/\nu$, while the line of $\beta = 0$ is drawn thicker. Contours of the temporal amplification rate ω_i are plotted in sections of constant ω_r. Hereby, ω_r is varied with a delta of $\Delta\omega_r = 2.0 \times 10^{-5} U_\infty^2/\nu$ starting from $\omega_r = 2.0 \times 10^{-5} U_\infty^2/\nu$. Using this type of stability diagram three-dimensional stability properties of a specific flow problem can be assessed.

In the spatial problem we vary the parameters (Re_x, ω, β) and solve for α_r and α_i. A spatial linear stability diagram of the Blasius boundary layer over a rigid wall is shown in fig. 5.3. Again, only the unstable region of the eigenvalues, i.e. $\alpha_i < 0$, is shown. The neutral stability surface is displayed in gray (translucent). Contour lines of constant β at neutral stability are plotted with the line of $\beta = 0$ drawn thicker. These contour lines have a delta of $\Delta\beta = 2.5 \times 10^{-5} U_\infty/\nu$. Contours of the spatial amplification rate α_i are plotted in planes of constant ω_r starting from $\omega_r = 2.0 \times 10^{-5} U_\infty^2/\nu$ with a delta of $\Delta\omega_r = 2.0 \times 10^{-5} U_\infty^2/\nu$.
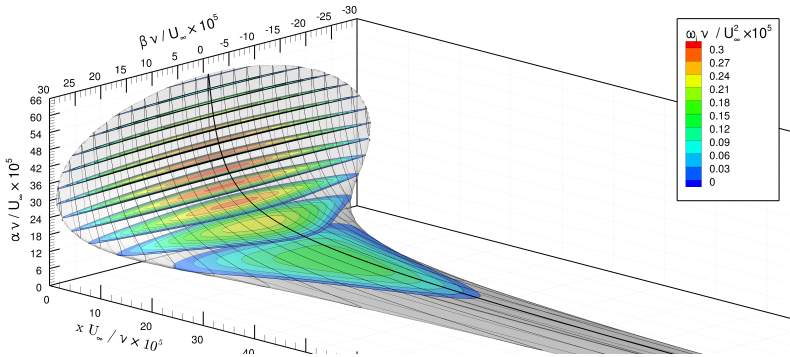
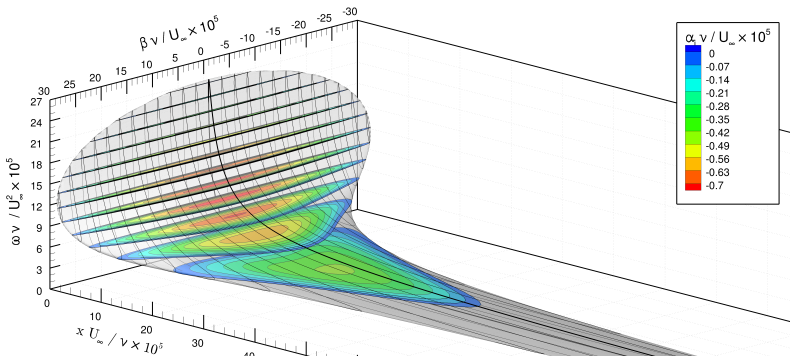Figure 5.2 Temporal linear stability diagram of the Blasius BL over a rigid wall.

Figure 5.3 Spatial linear stability diagram of the Blasius BL over a rigid wall.

5.3 Three-Dimensional Linear Stability Diagrams for Anisotropic Compliant Walls

As stated in chap. 1 the FISI modes of a compliant wall can become absolutely unstable. In contrast to that, TS modes can only be convectively unstable. In practice an absolute instability instantaneously triggers laminar-turbulent transition and leads to a failure in transition postponement. For the choice of a compliant wall, we follow Carpenter's approach [13] to constrain its properties so that the FISI modes are stable at all times, even though a convectively unstable FISI mode is not necessarily harmful. An instability mode is convectively or absolutely unstable if and only if it exhibits temporal instability (cf. Huerre and Monkewitz [35]). Hence, our aim is that FISI modes are temporarily stable and that the TS mode is as stable as possible. Now that the TS modes are typically damped with increasing suppleness of the compliant wall, and FISI modes typically amplified with increasing suppleness, optimized parameters usually exhibit marginal stability of FISI modes. It can be argued that transition could be further delayed if a convective instability of the FISI mode is accepted in order to reduce the TS instability further, but in the stability investigations performed for this work the FISI mode was, if it was unstable, always considerably more unstable than the TS mode of the rigid wall. Thus the investigations indicate that Carpenter's approach is reasonable. This approach also has the advantage, that extensive investigations whether a FISI mode is absolutely or convectively unstable are not necessary.

For the following temporal stability diagrams the TS mode and the FISI modes were computed and the unstable regions of all modes are shown in the same diagram. Note that this is not apparent since only the unstable regions are visualized. The temporal stability calculations of the individual modes were performed with the shooting method. Additionally, the matrix solver was used to make sure no other unstable mode exists, which has not already been tracked by the shooting method. For the following spatial stability diagrams only the TS mode was computed using the shooting method.
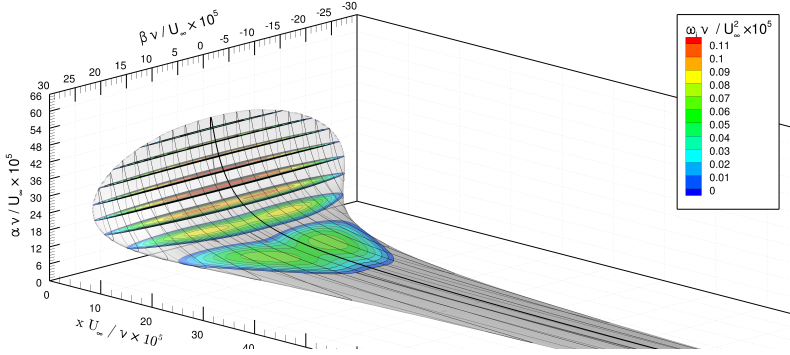
Figure 5.4 Temporal linear stability diagram of the Blasius BL over a compliant wall with parameter set 2, $\theta = 60°$, and $\psi = 0°$.

A temporal stability diagram of parameter set 2 is plotted in fig. 5.4. The visualization of surfaces, contour planes, etc. is analogous to fig. 5.2, except for a modified color legend. Note the considerably smaller maximum (temporal) amplification rate of $\omega_{i,\max} = 0.12 \times 10^{-5} U_\infty^2/\nu$ compared to the rigid wall case of $\omega_{i,\max} = 0.31 \times 10^{-5} U_\infty^2/\nu$. Also the region of instability is notably smaller than in the rigid wall case. Its extension in the α-, and β-direction is reduced, and branch II has moved slightly forward. Looking at the planes of constant ω_r, we can see that for lower values of ω_r there are two local maxima on either side of the plane $\beta = 0$ compared to one maximum in the rigid wall case. In comparison to Zengl and Rist [71] the computations extend considerably further downstream. As predicted by Carpenter [15] the FISI modes are stable in the whole domain.

The according spatial stability diagram of parameter set 2 is plotted in fig. 5.5. The visualization of surfaces, contour planes, etc. is analogue to fig. 5.3, except for a modified color legend. The (spatial) maximum amplification rate of $\alpha_{i,\min} = -0.28 \times 10^{-5} U_\infty/\nu$ is also notably smaller than in the rigid wall case of $\alpha_{i,\min} = -0.75 \times 10^{-5} U_\infty/\nu$. in analogy to the temporal case, there are also two local maxima in the planes of constant ω_r

In the presented linear stability diagrams we can see that the maximum amplification rate as well as the size of the instability region is decreased
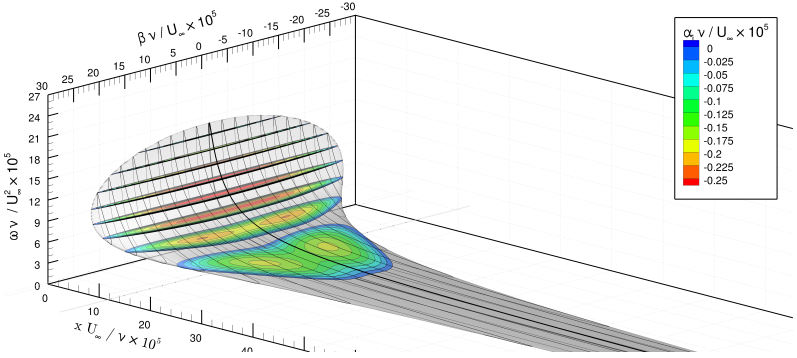
Figure 5.5 Spatial linear stability diagram of the Blasius BL over a compliant
wall with parameter set 2, $\theta = 60°$, and $\psi = 0°$.

in the case of the anisotropic compliant wall parameter set 2. Other than
the TS mode, no additional unstable modes are present in the temporal
case—so no absolute instability is present here. It is also to note that the
amplification rate contours at lower values of ω_r and accordingly α_r exhibit
two symmetric maxima at $\beta \neq 0$.

5.4 N-Factor Analysis of the Anisotropic Compliant Wall

We use N-factor analysis to examine the effect of the yawed anisotropic com-
pliant walls on the transition location. The basic idea of this type of analysis
for prediction of the transition location is, to calculate where the highest
amplification factor of unstable waves reaches an empirically determined
threshold. More information on transition prediction using N-factors can
be found e.g., in [17, 53, 55]. For a disturbance of frequency ω and spanwise
wavenumber β, we define $N(x, \beta, \omega)$ as

$$e^{N(x,\beta,\omega)} = \frac{A(x, \beta, \omega)}{A(x(\alpha_i = 0), \beta, \omega)} =$$

$$\int_{x(\alpha_i=0)}^{x} -\alpha_i(x, \beta, \omega) \quad dx \quad \text{for} \quad x \geqslant x(\alpha_i = 0) \quad . \quad (5.1)$$

In a low disturbance environment such as free flight the transition location is
typically at $N = 9$. Since we search for the highest wave amplification over

the streamwise coordinate, we need to take the envelope over all frequencies into account. We define it as:

$$N_\omega(x, \beta) = \max_\omega \left(N\left(x, \beta, \omega\right) \right) \qquad . \tag{5.2}$$

This envelope still varies over the spanwise wavenumber β. We define the envelope over ω and β as:

$$N_{\omega,\beta}(x) = \max_{\omega, \beta} \left(N\left(x, \beta, \omega\right) \right) \qquad . \tag{5.3}$$

It should be noted that the N-factor analysis does not account for the receptivity of the disturbances, their nonlinear growth, and their nonlinear interactions. Taking the envelope over all frequencies and/or spanwise wavenumbers basically assumes that these factors are equal for all waves, which is unlikely to be the case. Furthermore, it is only valid for low disturbance environments.

(a) Rigid wall case.

(b) Compliant wall with parameter set 2; $\theta = 60°$, $\psi = 0°$.
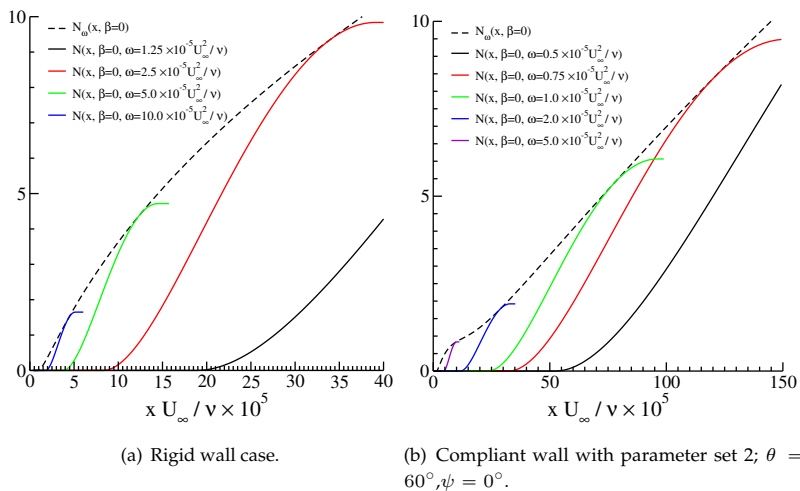
Figure 5.6 N-Factor development of the Blasius boundary layer for $\beta = 0$ and different angular frequencies. The envelope N_ω is shown as a dashed line.

N-Factor over x diagrams for two-dimensional TS modes (i.e. $\beta = 0$) with different angular frequencies ω are shown in fig. 5.6 for (a) the rigid wall

and (b) a compliant wall with parameter set 2. Their envelope N_ω is shown as a dashed line. In the boundary layer over the rigid wall the amplification factor of e^9 is first reached at the downstream location of $x = 32 \times 10^5 \nu/U_\infty$. The according wave has an angular frequency of approximately $\omega_r = 2.5 \times 10^{-5} U_\infty^2/\nu$. For the compliant wall, the amplification factor of e^9 is first reached by a 2-D wave at $x = 130 \times 10^5 \nu/U_\infty$. Here the according wave has an angular frequency of approximately $\omega_r = 0.75 \times 10^{-5} U_\infty^2/\nu$. So if only 2-D waves are under consideration, the laminar length is enlarged by a factor of 4.06. The frequencies of the TS modes that lead to transition are reduced down to approximately $\omega_r = 0.75 \times 10^{-5} U_\infty^2/\nu$, so that the lower frequencies play a larger role for the compliant wall under consideration.

As stated in sect. 2.5, three-dimensional instabilities have to be taken into account for an authoritative investigation of the stability properties and prediction of the transition location. Therefore, we extend the diagrams with the dimension of the spanwise wavenumber. In return, we restrict ourself to display the N-factor envelope over all frequencies N_ω. In fig. 5.7 the N-
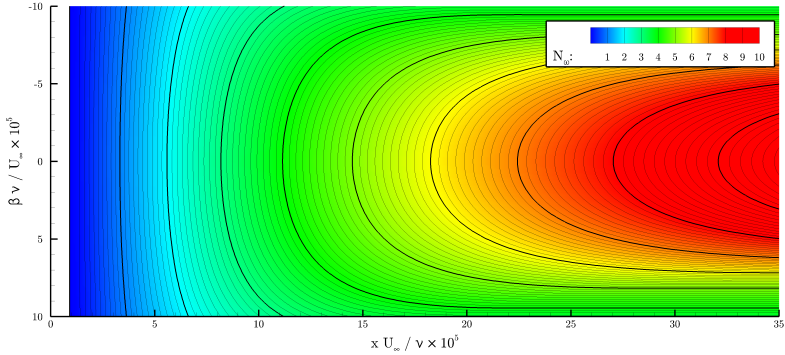
Figure 5.7 N-factor envelope over all frequencies for the rigid wall

factor envelope N_ω is plotted over the streamwise coordinate and spanwise wavenumber for the rigid wall. We can see that at $x = 32 \times 10^5 \nu/U_\infty$ a wave with $\beta = 0$ first reaches the amplification factor of e^9. It can be seen that two-dimensional waves reach given N-factors earlier than oblique-traveling waves. Hence, the transition location in a low disturbance environment is
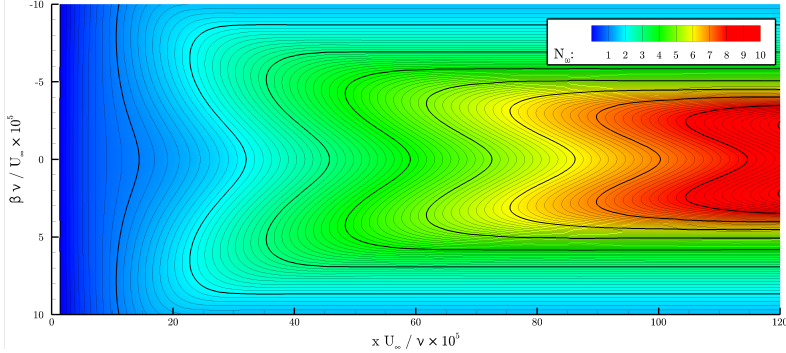
predicted to be at $x = 32 \times 10^5 \nu/U_\infty$.

Figure 5.8 N-factor envelope over all frequencies for the anisotropic compliant wall with parameter set 2; $\theta = 60°, \psi = 0°$.

In contrast to that, the N-factor envelope N_ω is plotted in fig. 5.8 over the streamwise coordinate and spanwise wavenumber for the anisotropic compliant wall with parameter set 2. For $N_\omega > 0.6$, it can be seen that three-dimensional waves reach given amplification factors first. Therefore, three-dimensional waves lead to transition. Since wall and flow field are symmetrical in spanwise direction, the amplifications are symmetrical as well. Here, the transition location based on the amplification factor of e^9 is predicted at $x = 120 \times 10^5 \nu/U_\infty$. So the predicted transition location is $\Delta x = 10 \times 10^5 \nu/U_\infty$ further upstream than in the 2-D based prediction. The predicted enlargement of the laminar length is 3.75 times greater than in the rigid wall case. It is evident that the transition prediction based only on two-dimensional solutions overpredicts transition delay. The streamwise and spanwise wavenumbers of the wave that first reaches the amplification factor of e^9 are $\alpha_r = 2.4 \times 10^{-5} U_\infty/\nu$ and $\beta = 2.0 \times 10^{-5} U_\infty/\nu$ and the angular frequency $\omega = 0.7 \times 10^{-5} U_\infty^2/\nu$. That corresponds to a phase speed of $c_{\text{ph.}} = 0.30$ and a wave propagation angle of $\Psi = \tan^{-1}\left(\frac{\beta}{\alpha}\right) = 40°$.

5.5 Yawing of the Compliant Wall with $\theta = 60°$

In a parameter study, the yaw angle was increased in steps of $\Delta\psi = 5°$ up to a value of $\psi = 90°$. A spatial linear stability diagram for the compliant

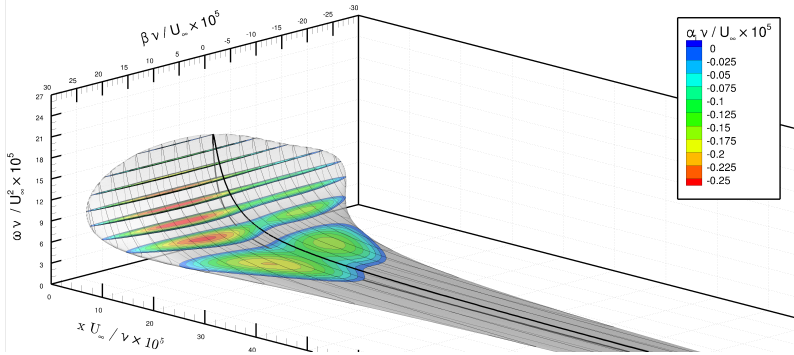*Figure 5.9* Spatial linear stability diagram of the Blasius BL over a compliant wall with parameter set 2, $\theta = 60°$, and $\psi = 35°$.

wall parameter set 2 with $\psi = 35°$ is plotted in fig. 5.9. For this case, temporal LST shows that both FISI modes are temporarily stable. So only the TS mode is unstable in the computational domain. As one would expect, the diagram is asymmetric with respect to $\beta = 0$. We can see that the maximum amplification rate has moved from $\beta = 0$ to approximately $\beta = 10 \times 10^{-5} U_\infty/\nu$ with a growth rate of $\alpha_{i,min} = -0.287 \times 10^{-5} U_\infty/\nu$. For lower frequencies two local maxima exist for left- and right-traveling waves. Hereby, the local maximum for right-traveling waves exhibits the higher growth rate. In the amplification rate contour of $\omega_r = 2.0 \times 10^{-5} U_\infty^2/\nu$ the right-traveling maximum shows a higher amplification rate than in the case of $\psi = 0$.

The according N_ω-diagram of the TS mode is presented in fig. 5.10. All waves that reach a particular N-factor first have a positive spanwise wavenumber β. It is also evident that transition delay is overpredicted if only two-dimensional waves are taken into account. The amplification factor e^9 is first reached at $x = 117 \times 10^5 \nu/U_\infty$. A comparison to the results with $\psi = 0$
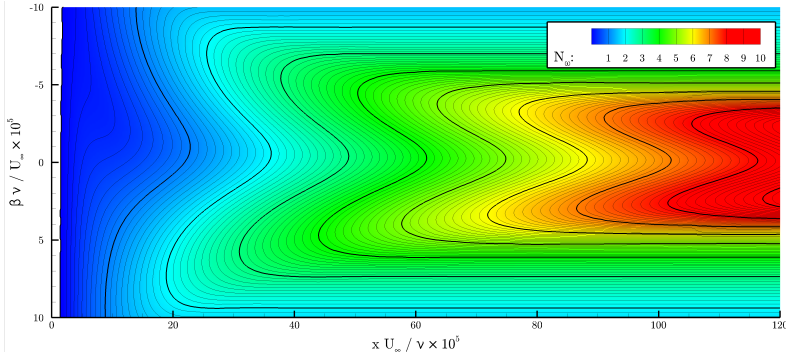
Figure 5.10 N-factor envelope over all frequencies for the anisotropic compliant wall with parameter set 2; $\theta = 60°, \psi = 35°$

shows, that the yawing of the compliant wall is not beneficial for delaying transition. The simulations at the intermediate steps between $\psi = 0°$ and $\psi = 35°$ show a continuous change of the amplification rates and N-factor plots, as well as the absence of instabilities other than the TS mode.

This changes for $\psi = 40°$—here a FISI mode becomes temporally unstable, with the potential risk of absolute instability. The instability of this mode prevails in all other cases up to $\psi = 90°$. A temporal linear stability diagram for $\psi = 45°$ is shown in fig. 5.11. Here the TS mode as well as a FISI mode is visible i.e. unstable. The FISI mode only exhibits amplification in a region with $\beta < 0$ and is stable for $\beta = 0$. Hence, if only two-dimensional stability investigations were performed, a FISI mode, which can exhibit absolute instability, would be present without showing up in the results. The N-factor envelope of the FISI mode over frequency is shown in fig 5.12. Apparently, if the FISI mode is only convectively unstable, it will not trigger transition, because the TS mode reaches given N-factors first. At $\psi = 50°$ the unstable FISI mode is also unstable at $\beta = 0$.

Increasing the yaw angle further to $\psi = 70°$ the TS waves location of the maximum growth rate shifts from a right-traveling wave to a left-traveling wave. This can be observed in fig. 5.13. Here, the spatial amplification rates of the global maximum of the amplification rate is now on the side of
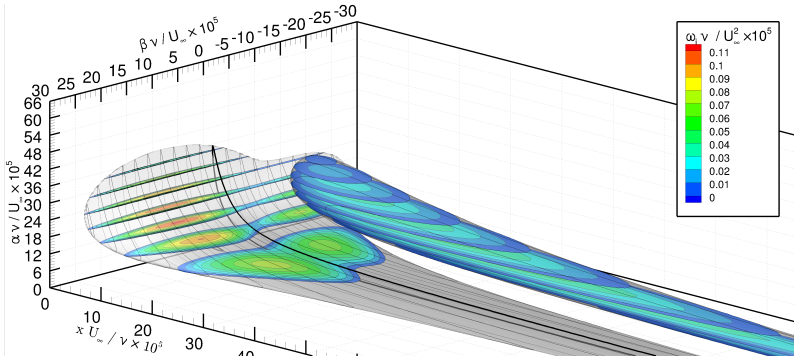
Figure 5.11 Temporal linear stability diagram of the Blasius BL over a compliant wall with parameter set 2, $\theta = 60°$, and $\psi = 45°$.
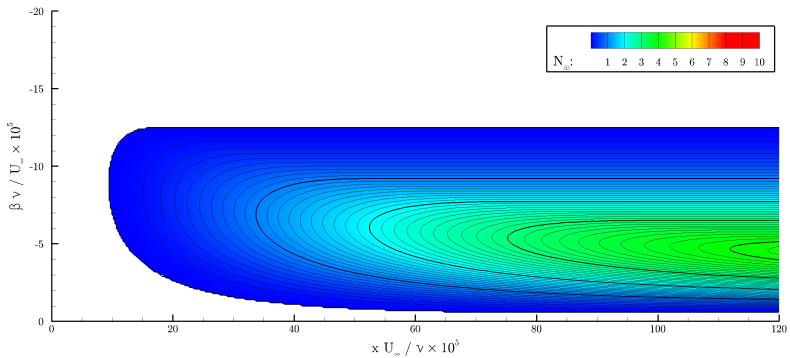

Figure 5.12 N-factor envelope over all frequencies of the unstable FISI mode for the anisotropic compliant wall with parameter set 2; $\theta = 60°, \psi = 45°$.
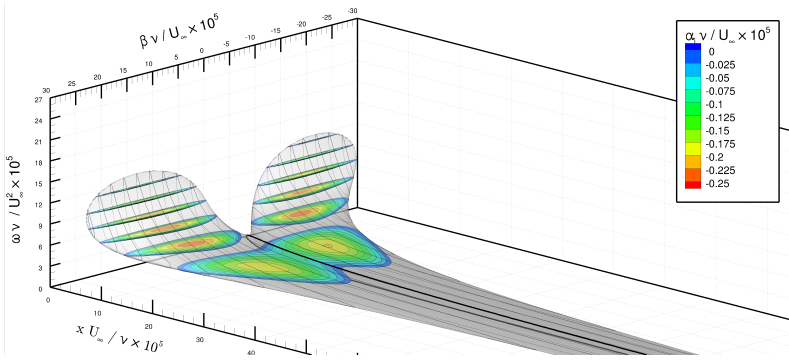
Figure 5.13 Spatial linear stability diagram of the Blasius BL over a compliant wall with parameter set 2, $\theta = 60°$, and $\psi = 70°$.

left-traveling waves. For the low frequencies, which play the key role for transition in a low disturbance environment, the maximum amplification rate also occurs at a left-traveling wave. The diagram displays some type of symmetry in the extent of the unstable region. Two-dimensional instabilities are greatly reduced, which is perceivable by the thick line at $\beta = 0$. However, a FISI mode is unstable (detected in the according temporal stability investigations), rendering any benefit of damping the TS wave as useless.

5.6 Yawing of the Compliant Wall with $\theta = 75°$

The effects that we have seen for the compliant wall parameter set 2 also show up for compliant wall parameter set 3. In fig. 5.14 is a temporal LST diagram for the yaw angle of $\psi = 0°$. Only the TS mode is unstable/visible. Its amplification rate is further reduced compared to the case of $\theta = 60°$ with a maximum amplification rate of $\omega_{i,\max} = 0.835 \times 10^{-5} U_\infty^2 / \nu$ in the temporal case, and a maximum amplification rate of $\alpha_{i,\min} = -0.207 \times 10^{-5} U_\infty / \nu$ in the spatial case. Additionally, the unstable region is smaller. Again there exist two symmetric local maxima for the low frequencies, and these are relevant for laminar turbulent transition.

With increasing yaw angle the location of the maximum amplification rate moves to positive spanwise wavenumbers. In fig. 5.15 is a temporal LST
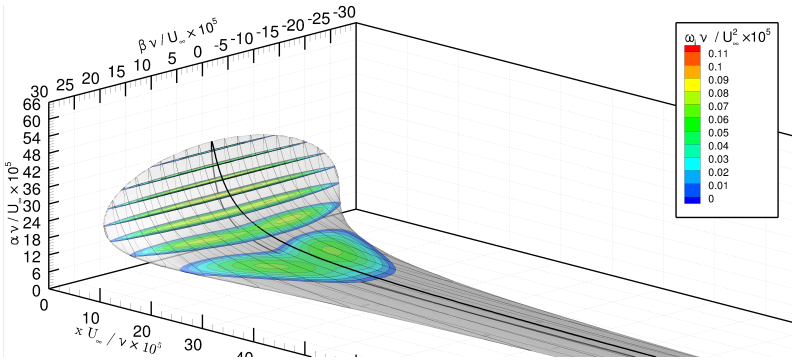
Figure 5.14 Temporal linear stability diagram of the Blasius BL over a compliant wall with parameter set 3, $\theta = 75°$, and $\psi = 0°$.

diagram for $\theta = 30°$ which shows that the maximum amplification rate has increased to $\omega_{i,max} = 0.936{\times}10^{-5}U_\infty^2/\nu$ and is located at $\beta = 10.0{\times}10^{-5}U_\infty/\nu$. In the low frequency region the unstable region has increased slightly with approximately the same level of amplification rates as in $\psi = 0°$.
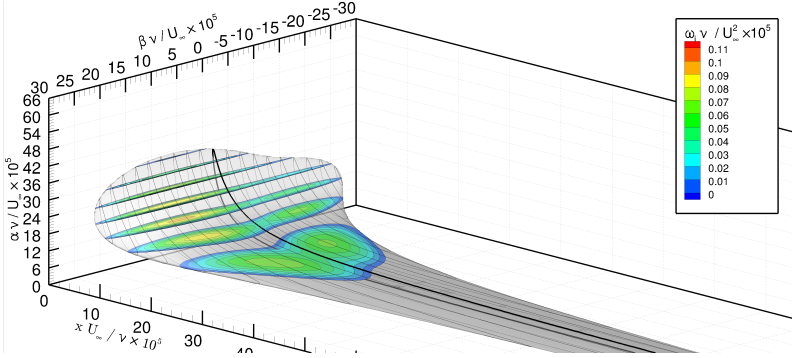

Figure 5.15 Temporal linear stability diagram of the Blasius BL over a compliant wall with parameter set 3, $\theta = 75°$, and $\psi = 30°$.

Fig. 5.16 shows that for $\psi = 55°$ the location of the maximum amplification rate also switches to a left-traveling wave. Here it is also visible that the plane for $\beta = 0$ exhibits a clearly smaller instability region and lower amplification rates than in the case of $\psi = 0$.
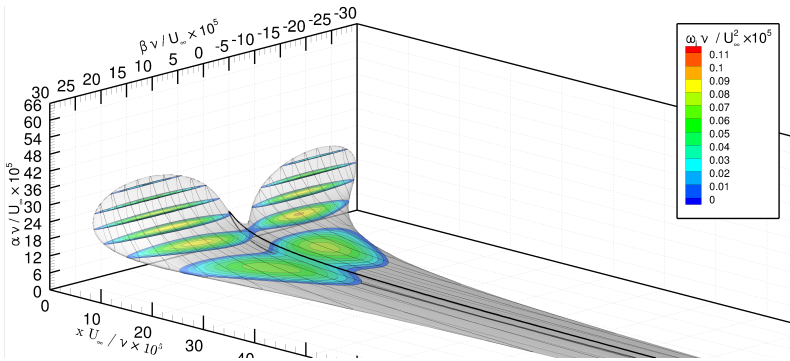
Figure 5.16 Temporal linear stability diagram of the Blasius BL over a compliant wall with parameter set 3, $\theta = 75°$, and $\psi = 55°$.

At a yaw angle of $\psi = 70°$ a FISI mode becomes temporally unstable rendering the setup as prone to suffer absolute instability. The according temporal LST diagram is shown in fig. 5.17. It is visible that the maximum amplification rate has risen. Also the unstable region in the low frequency range is larger and exhibits higher amplification rates.
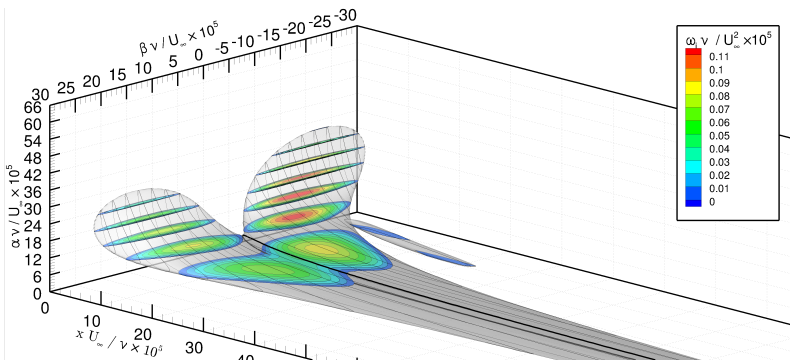

Figure 5.17 Temporal linear stability diagram of the Blasius BL over a compliant wall with parameter set 3, $\theta = 75°$, and $\psi = 70°$.

So when the wall with parameter set 3 is yawed, the flow over the compliant wall shows similar effects as the flow over the compliant wall with parameter set 2, but amplification rates and the specific angle at which the

effects takes place are different.

5.7 Conclusions on Yawing of the Compliant Wall

The effect of yawing the anisotropic compliant wall with respect to the flow direction can be evaluated using fig. 5.18. Here the N-factor envelope over frequency and spanwise wavenumber is plotted versus the streamwise direction. It can be seen that with increasing yaw angle the laminar length
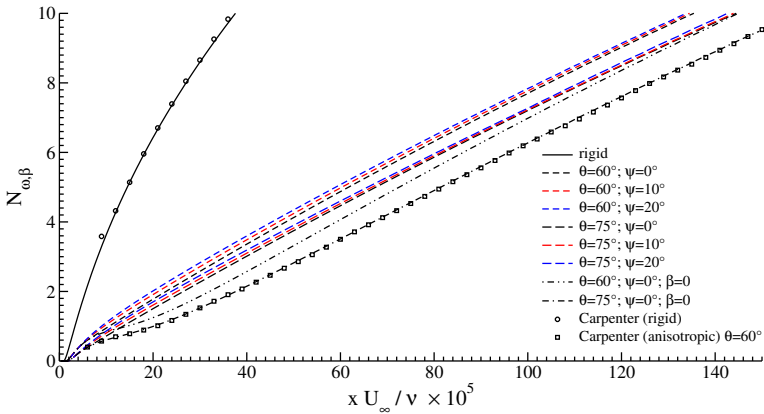

Figure 5.18 N-factor envelope with respect to frequency and spanwise wavenumber versus streamwise direction for rigid wall, compliant wall parameter set 2 ($\theta = 60°$.), and set 3 ($\theta = 75°$) for different yaw angles, and when only two-dimensional waves are considered ($\beta = 0$). Symbols represent digitized data of Carpenter [15, fig.22]

shortens for both, the compliant wall with parameter set 2, and with parameter set 3 . Hereby, the previous findings are that a FISI mode becomes unstable at a certain point. The comparison with Carpenter [15, fig. 22] shows that the rigid-wall results of our method and Carpenter are in good agreement with each other. Since Carpenter has based his results on two-dimensional calculations the N-factor envelope of parameter set 2 and set 3 with respect to all frequencies is plotted for $\beta = 0$. Here the result of

Carpenter does not agree with the according curve of our method. However, it can be seen that Carpenter's curve for $\theta = 60°$ is in good agreement with our curve for $\theta = 75°$. A plausible explanation is that Carpenter's curve might be labeled wrong, since the curves for the rigid wall are in good agreement and since other comparisons to Carpenter shown in app. D exhibit good agreements. The comparison of the two-dimensional to the three-dimensional results shows that the transition delay is overpredicted for all underlying N-factors in the plotted range.

In the previous sections spatial and temporal linear stability calculations were presented. These have shown that the spanwise wavenumber, where the maximum amplification rate of the TS mode is located at, can be altered by the yaw angle. For low disturbance environments, N-Factor calculations have shown that the relevant waves leading to laminar-turbulent transition for anisotropic compliant walls exhibit lower frequencies than in the rigid wall case. Also these waves have a much lower frequency than the waves which exhibit the highest growth rate. Furthermore, for the anisotropic compliant walls (parameter sets 2 and 3), the waves that lead to transition are not two-dimensional waves, rather they are waves with wave propagation angles in the order of $\Psi = 40°$. This implies that the breakdown scenario is fundamentally different compared to rigid walls. Here, oblique breakdown (cf. Fasel et.al. [22], Thumm[60]) can play a role, as well as other types of breakdown scenarios, such as subharmonic breakdown (cf. Kosinov et.al. [40]) or oblique-subharmonic resonance (cf. Zengl, von Terzi, and Rist [73]).

The assessments in this chapter show that concise stability investigations of anisotropic compliant walls must incorporate oblique-traveling waves. The findings are:

1. FISI modes can exhibit temporal stability for two-dimensional waves, but temporal instability at oblique-traveling waves. Since FISI modes can exhibit absolute instability this can be counterproductive for the delay of transition.

2. Two-dimensional waves can be significantly more stable than oblique-

traveling waves. Prediction of laminar-turbulent transition can lead to inherently wrong results if it is only based on two-dimensional instabilities.

In conclusion, for the chosen wall parameters, no benefits on the transition location could be obtained by yawing of the compliant wall with a yaw angle which is constant in streamwise direction. The results have underlined the significance of oblique-traveling waves for their relevance on laminar-turbulent breakdown.

6 Transient Growth

In the previous chapters the behavior of disturbances in low disturbance environments, where exponential disturbance growth is relevant, were assessed. The higher the disturbance level, the more relevant is the short-term behavior, i.e. transient growth, of fluid instabilities. In sect. 4.7 it is shown that, when the resolution is increased, the numerical results of the eigenvalue problem deteriorate earlier for compliant walls than for rigid walls. This indicates that the compliant wall might alter the transient behavior of instabilities considerably.

To examine the long-term behavior of instabilities, we investigate the growth or decay of eigenmodes in the boundary layer. Hereby, the least stable eigenmode typically triggers transition. To examine the short-term behavior of instabilities, i.e., their transient growth, we now investigate a superposition of several eigenmodes, independent of weather they are stable or not. Hereby, the initial condition—the starting disturbance—which exhibits the strongest transient growth typically triggers transition. Even if all eigenmodes are stable, their superposition can result in a transient growth, because the eigenmodes of the Orr-Sommerfeld and Squire equation are non-orthogonal. With a chosen disturbance measure, we evaluate how different initial conditions, i.e. initial disturbances, develop over time, before they resemble the shape of the least unstable eigenmode.

6.1 The Choice of Disturbance Measure

To quantify the amplitude of disturbances in the boundary layer over a compliant wall, we need an appropriate measure. This measure should be independent of numerical parameters, such as resolution and domain size, and should ideally have a physical meaning. From a mathematical point-of-view the measure must result in a mathematical norm. In incompressible flows the use of the kinetic energy in the fluid disturbance is a common choice. Since the compliant wall generally also exhibits distortions due to the disturbances, the energy of the wall must be considered as well. Taking solely the fluid kinetic energy will result in initial conditions where little energy is in the flow but large energy is stored in the kinetic or potential energy of the wall, which leads to skyrocketing energy growth when energy is transferred from the wall to the fluid. Therefore, we choose to use the sum of the energy of the fluid

$$E_{\text{fluid}} = \int_0^\infty \tilde{u}^H \tilde{u} + \tilde{v}^H \tilde{v} + \tilde{w}^H \tilde{w} \, dy \ , \tag{6.1}$$

and the kinetic and potential energy of the compliant wall

$$E_{\text{wall}} = \frac{C_m}{\cos^2 \theta} \tilde{v}_w^H \tilde{v}_w + \left(\frac{C_k}{\cos^2 \theta} + \kappa^4 C_b + \alpha^2 C_{Tx} + \beta^2 C_{Tz} + \right.$$
$$\left. C_i \tan^2 \theta \left(\alpha^2 + \beta^2 - C_\nu \left(\alpha \sin \psi - \beta \cos \psi \right)^2 \right) \right) \tilde{\eta}^H \tilde{\eta} \ . \tag{6.2}$$

as our measure of disturbance amplitude. Hence the only source of disturbance amplitude is the base flow.

After discretization, we can write the energy of an arbitrary disturbance as

$$E(t) = \mathbf{x}^H \, \mathbf{Q}_E \, \mathbf{x} \ , \tag{6.3}$$

with $\mathbf{x}$ (defined in eqn. (4.17)) being the complex state of the disturbance, and the energy weight matrix

$$\mathbf{Q}_E = \underbrace{\mathbf{U}^H \, \text{diag}(\mathbf{w_{cc}}) \mathbf{U} + \mathbf{V}^H \, \text{diag}(\mathbf{w_{cc}}) \mathbf{V} + \mathbf{W}^H \, \text{diag}(\mathbf{w_{cc}}) \mathbf{W}}_{\text{fluid energy}} +$$

$$\underbrace{\frac{C_m}{\cos^2\theta}\mathbf{V_0}^H\mathbf{V_0}}_{\text{kinetic wall energy}} +$$

$$\underbrace{\left(\frac{C_k}{\cos^2\theta} + \kappa^4 C_b + \alpha^2 C_{Tx} + \beta^2 C_{Tz} + \tan^2\theta\, C_i\left(\kappa^2 - t_5^2 C_\nu\right)\right)\boldsymbol{\eta}^H\boldsymbol{\eta}}_{\text{potential wall energy}} \quad . \quad (6.4)$$

Hereby the matrices

$$\mathbf{U} = \frac{\mathrm{i}}{\kappa^2}\left[\alpha\mathbf{D}^{(1)} \quad -\beta\mathbf{D}^{(0)} \quad \mathbf{0}_{(N_c\times 1)}\right] \quad , \tag{6.5}$$

$$\mathbf{V} = \left[\mathbf{D}^{(0)} \quad \mathbf{0}_{(N_c\times N_c)} \quad \mathbf{0}_{(N_c\times 1)}\right] \quad , \tag{6.6}$$

$$\mathbf{W} = \frac{\mathrm{i}}{\kappa^2}\left[\beta\mathbf{D}^{(1)}\alpha\mathbf{D}^{(0)}\mathbf{0}_{(N_c\times 1)}\right] \quad , \tag{6.7}$$

$$\mathbf{V_0} = \left[\mathbf{1}_{(1\times 1)} \quad \mathbf{0}_{(1\times 2N_c)}\right] \quad , \tag{6.8}$$

and

$$\boldsymbol{\eta} = \left[\mathbf{0}_{(1\times 2N_c)} \quad \mathbf{1}_{(1\times 1)}\right] \tag{6.9}$$

transform the disturbance state $\mathbf{x}$ to the fluid velocities $\mathbf{u}$, $\mathbf{v}$, $\mathbf{w}$, wall velocity $\mathbf{v_0}$ and wall elongation $\boldsymbol{\eta}$, respectively, e.g., like $\mathbf{u} = \mathbf{U}\mathbf{x}$.

Note that the matrix $\mathbf{Q}_E$ is positive definite due to the choice of Clenshaw-Curtis quadrature, which has positive nonzero weights. Hence, a Cholesky decomposition exists for $\mathbf{Q}_E = \mathbf{F}^H\mathbf{F}$ so that we obtain the energy-based norm of a disturbance $\mathbf{x}$ as

$$\|\mathbf{x}\|_E = \|\mathbf{F}\mathbf{x}\|_2 \quad . \tag{6.10}$$

Using the SVD of $\mathbf{Q}_E = \mathbf{U}\boldsymbol{\Sigma}\mathbf{V}^H$ we calculate a Cholesky factor of it with

$$\mathbf{F} = \boldsymbol{\Sigma}^{\frac{1}{2}}\mathbf{V}^H \quad , \tag{6.11}$$

and the inverse of the Cholesky factor with

$$\mathbf{F}^{-1} = \left(\mathbf{V}^H\right)^H \boldsymbol{\Sigma}^{-\frac{1}{2}} \quad . \tag{6.12}$$

6.2 Calculation of Transient Growth and Optimal Perturbations

Starting from the eigenvalue spectrum obtained by the matrix method, we choose a set of eigenmodes to consider, and optimize a superposition of these modes with respect to maximum growth within a time span τ. With the matrix $\mathbf{X}$ containing the eigenvectors we consider in columns, we can write an arbitrary disturbance $\mathbf{x}$ as a superposition of these modes with the amplitudes k_i

$$\mathbf{x} = \mathbf{X}\,\mathbf{k} \ . \tag{6.13}$$

Since the amplitudes $\mathbf{k}$ of the modes are time dependent, we define the Matrix $\mathbf{\Lambda}$ as the diagonal matrix containing the amplification rates ω_i on its diagonal and obtain

$$\mathbf{k} = e^{-\mathrm{i}\mathbf{\Lambda}t}\mathbf{k}_0 = \begin{bmatrix} e^{-\mathrm{i}\omega_1 t} & & \\ & \ddots & \\ & & e^{-\mathrm{i}\omega_N t} \end{bmatrix} \mathbf{k}_0 \ . \tag{6.14}$$

Hence, the energy of an arbitrary disturbance formed by the eigenmodes under consideration is

$$E(t) = \mathbf{x}^H\,\mathbf{Q}_E\mathbf{x} = \mathbf{k}_0^H \left(e^{-\mathrm{i}\mathbf{\Lambda}t}\right)^H \underbrace{\mathbf{X}^H\mathbf{Q}_E\mathbf{X}}_{\mathbf{M}=\mathbf{S}^H\mathbf{S}}\, e^{-\mathrm{i}\mathbf{\Lambda}t}\mathbf{k}_0 \ . \tag{6.15}$$

The matrix $\mathbf{M}$ is named the matrix of angles and we use the symbol $\mathbf{S}$ for its Cholesky factor.

We define an optimal perturbation to be a disturbance, which exhibits maximum energy growth within a certain time span. To calculate the maximum energy gain $G(t)$, we want to know the initial amplitudes $\mathbf{k}_0$ of all modes under consideration which maximize the energy gain within the time span t. This can be written as

$$G(t) = \max_{\mathbf{k}_0} \frac{E(t)}{E(t=0)} \ . \tag{6.16}$$

The function $G(t)$ forms an upper envelope for all time transients in energy.

In case the eigenvectors of $\mathbf{X}$ are scaled with their disturbance energy, we can rewrite the energy gain as follows (cf. Schmid [55], sect. 4.4.2):

$$G(t) = \max_{\mathbf{k}_0} \frac{\mathbf{k}_0^H \left(e^{-i\mathbf{\Lambda} t}\right)^H \mathbf{S}^H \mathbf{S} e^{-i\mathbf{\Lambda} t} \mathbf{k}_0}{\mathbf{k}_0^H \mathbf{S}^H \mathbf{S} \mathbf{k}_0} \tag{6.17}$$

$$= \max_{\mathbf{k}_0} \frac{\left\| \mathbf{S} e^{-i\mathbf{\Lambda} t} \mathbf{k}_0 \right\|_2^2}{\left\| \mathbf{S} \mathbf{k}_0 \right\|_2^2} \tag{6.18}$$

$$= \max_{\mathbf{k}_0} \frac{\left\| \mathbf{S} e^{-i\mathbf{\Lambda} t} \mathbf{S}^{-1} \left(\mathbf{S} \mathbf{k}_0 \right) \right\|_2^2}{\left\| \mathbf{S} \mathbf{k}_0 \right\|_2^2} \tag{6.19}$$

$$= \left\| \mathbf{S} e^{-i\mathbf{\Lambda} t} \mathbf{S}^{-1} \right\|_2^2 \quad . \tag{6.20}$$

The initial amplitudes $\mathbf{k}_0$, representing the optimal disturbance, can be determined with the principal left singular vector $\mathbf{v}_1$ of the matrix $\left(\mathbf{S} e^{-i\mathbf{\Lambda} t} \mathbf{S}^{-1}\right)$ (cf. Schmid [55], sect. 4.4.3) using

$$\mathbf{k}_0 = \mathbf{S}^{-1} \mathbf{v}_1^* \quad . \tag{6.21}$$

To calculate $G(t)$, we

1. solve the Orr-Sommerfeld-Squire eigenvalue problem,

2. choose a set of eigenmodes to be considered for transient growth,

3. scale the eigenvectors with their disturbance energy,

4. calculate the according matrix of angles $\mathbf{M}$,

5. determine its Cholesky factor $\mathbf{S}$,

6. calculate the Euclidian norm of the matrix $\left(\mathbf{S} e^{-i\mathbf{\Lambda} t} \mathbf{S}^{-1}\right)$,

7. and finally take the square.

The Singular Value Decomposition (SVD) was chosen for the calculation of the Cholesky factor of $\mathbf{M}$ because it is less prone to numerical errors than the Cholesky algorithm (cf. Trefethen [64]). Furthermore, the SVD is used for the calculation of the Euclidian matrix norm. LAPACK routines [1] are used for the numerical implementation of the SVD. Note that the current method was

validated with results published in Schmid [55], results of this comparison can be found in App. D. Also, excellent quantitative agreement was found with Butler [12] regarding the location, magnitude and amplification time of the global optimal.

As an example, and for convenience of using the same parameters as in chap. 3 and chap. 4, energy transients of four different optimal perturbations and their envelope $G(t)$ are plotted over time in fig. 6.1 for the Blasius BL with $Re = 998$ and $\alpha = 3.0862 \times 10^{-4} U_\infty/\nu$. The calculations of the matrix
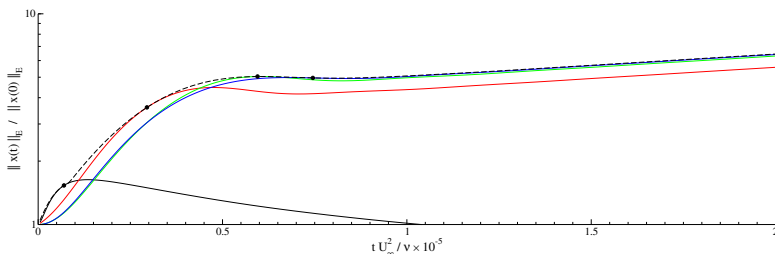

Figure 6.1 Energy transients of optimal perturbations with maximum growth within time span τ and their envelope $\sqrt{G(t)}$ for the Blasius BL over a rigid wall, with $Re_{\delta_1} = 998$, $\alpha = 3.0862 \times 10^{-4} U_\infty/\nu$, and $\beta = 0 :$ ——, $\tau = 0.07\, U_\infty^2/\nu \times 10^{-5}$; ——, $\tau = 0.3\, U_\infty^2/\nu \times 10^{-5}$; ——, $\tau = 0.595\, U_\infty^2/\nu \times 10^{-5}$; ——, $\tau = 0.75\, U_\infty^2/\nu \times 10^{-5}$; –––, $\sqrt{G(t)}$.

and shooting solver have shown, that the TS mode is unstable in this case. Hence, all transients and their envelope show an exponential growth with $\sqrt{E(t)/E(0)} \sim e^{\omega_i t}$ for $t \to \infty$. This is already visible for three perturbations. The optimal perturbation for $\tau = 0.07\, U_\infty^2/\nu \times 10^{-5}$ shows this behavior for $t \gg 10\, U_\infty^2/\nu \times 10^{-5}$, which is out of the viewport of this graph. A maximum energy growth[1] of $E(t)/E(0) = 25.4$ can be seen for the optimal perturbation with $\tau = 0.595\, U_\infty^2/\nu \times 10^{-5}$ and an immediate exponential growth due to a TS-type instability with $\omega_i = 0.246 \times 10^{-5} U_\infty^2/\nu$. This 2D-case shows significantly less transient growth potential compared to the 3D case, which can exhibit transient growth up to $E(t)/E(0) = 1514$ at $Re_{\delta 1} = 1000$ (cf.

---

[1] Note that the energy growth is the square of the plotted energy norm.

Butler [12]).

In contrast to that, the compliant wall case, with $\theta = 60°$ is shown in fig. 6.2. Here, all eigenvalues are stable. Consistently to that, all perturbations decay over time with the decay rate of the least stable discrete mode, i.e. the TS mode with $\omega_i = -0.055 \times 10^{-5} U_\infty^2/\nu$. In this case the maximum transient growth exhibits $E(t)/E(0) = 34.1$, which is larger than in the rigid wall case, but still significantly less than in the 3D-case which will be shown later. Note that the time transients in the compliant wall case exhibit oscillations in
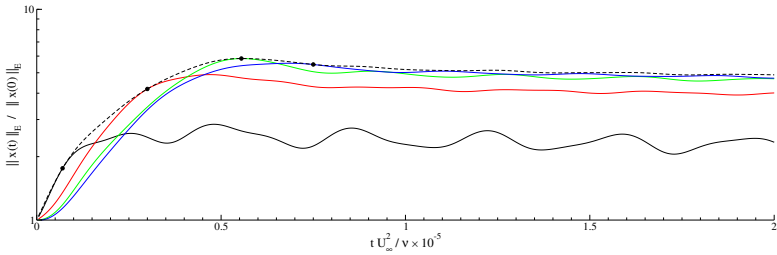

Figure 6.2 Energy transients of optimal pertubations with maximum growth within timespan τ and their envelope $\sqrt{G(t)}$ for the Blasius BL over the anisotropic compliant surface, case 2, with $Re_{\delta_1} = 998$, $\alpha = 3.0862 \times 10^{-4} U_\infty/\nu$, and $\beta = 0$: ——, $\tau = 0.07$; ——, $\tau = 0.3$; ——, $\tau = 0.555$; ——, $\tau = 0.75$; − − −, $\sqrt{G(t)}$.

time, which can be explained by superposition of two or more eigenmodes of similar amplitude. Even though the compliant surface stabilizes the TS mode in this case, the maximum transient energy growth increases. Therefore, the transient behavior is investigated in the α–β-plane in the following section.

6.3 Transient Growth for the Anisotropic Compliant Wall Case

To assess the influence of the compliant walls, with parameter set 2 and set 3, with $\theta = 60°$ and $\theta = 75°$, respectively, we follow Butler and Farrell [12] and Schmid [55] and calculate the maximum transient growth in the α–β-plane for $Re_{\delta_1} = 1000$. Here, we plot the largest singular value $\sigma_{\max} = \sqrt{G(t)}$ of

the matrix $\left(\mathbf{S}e^{-\mathrm{i}\mathbf{\Lambda}t}\mathbf{S}^{-1}\right)$, which corresponds to the maximum growth of an optimal perturbation in the energy norm (6.10). Note that this corresponds to the (local) maximum in the diagrams shown in the previous section.

Fig. 6.3 shows the contours of maximum transient growth for the rigid wall case. Hereby, the exponentially unstable region is omitted, and the exponential growth rate is plotted in black-white contours. The region
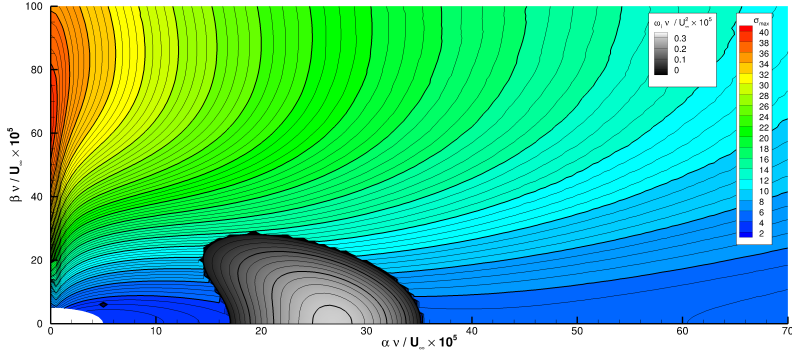

Figure 6.3 Colour-contours of maximum transient growth σ_{max} in the α–β-plane for $Re_{\delta_1} = 1000$ in the rigid wall case. Black-white contours denote the exponentially unstable region with temporal amplification rate ω_i.

where $\kappa < 5 \times 10^{-5} U_\infty/\nu$ is also omitted, because towards $\kappa = 0$ the solution becomes increasingly more dependent on the domain height. This is due to the implemented decay boundary condition in the free stream which requires larger domain heights for smaller resulting wavenumbers κ. Increasing domain height could partly remedy this effect, but therefore more collocation points would be necessary with according loss of precision (cf. sec. 4.7).

Fig. 6.4 shows the contours of maximum transient growth for the compliant wall case for parameter set 2, i.e. for $\theta = 60°$. Here we can see the typical reduction of the exponential growth in size and magnitude. It can clearly be seen that the global optimal at $\alpha = 0$ and $\beta = 65 \times 10^{-5} U_\infty/\nu$ is not affected in magnitude and location. The compliant wall does not affect this transient

growth mechanism at all. For small spanwise wavenumbers the compliant wall alters the transient growth of disturbances, with only a slight increase of maximum transient growth.
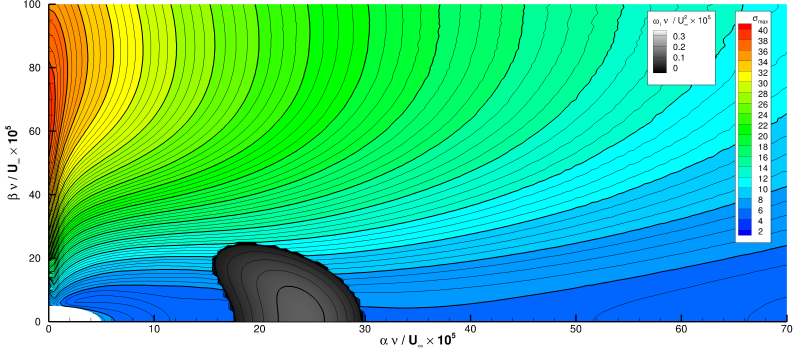

Figure 6.4 Color-contours of maximum transient growth $\sigma_{\max}$ in the α–β-plane for $Re_{\delta_1} = 1000$ in the compliant wall case, with $\theta = 60°$ and $\psi = 0°$. Black-white contours denote the exponentially unstable region with temporal amplification rate ω_i.

Fig. 6.5 shows the contours of maximum transient growth for the compliant wall case for parameter set 3, i.e. for $\theta = 75°$. Again, the global maximum transient growth is not altered by the compliant wall. Changes in transient growth are only visible in the region of smaller spanwise wavenumbers α. Also, the maximum transient growth is altered only in the region where transient growth is small compared to the global maximum.

We can conclude that the compliant walls under consideration do not exhibit a new relevant transient growth mechanism. However, the classical transient growth mechanism which is prevalent in the rigid wall case is not altered by the compliant walls under consideration of this work. So while exponential growth is attenuated by these compliant walls, transient growth is not attenuated.
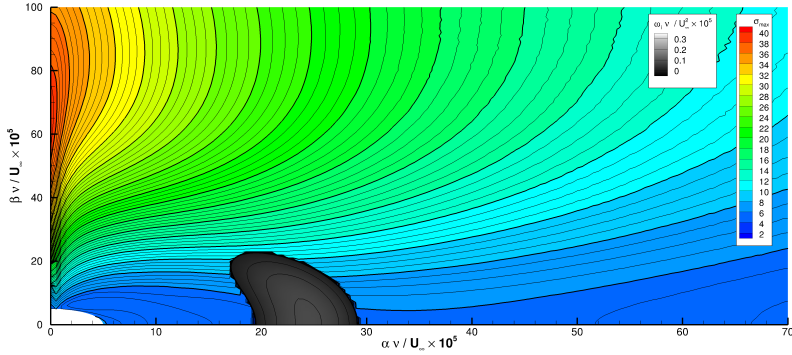
Figure 6.5 Color-contours of maximum transient growth $\sigma_{\max}$ in the α–β-plane for $Re_{\delta_1} = 1000$ in the compliant wall case, with $\theta = 75°$ and $\psi = 0°$. Black-white contours denote the exponentially unstable region with temporal amplification rate ω_i.

6.4 Effect of Yawing on Transient Growth of the Compliant Wall Case with $\theta = 60°$

Since yawing of the compliant wall material was investigated in chap. 5 regarding exponential growth and transition prediction using N-factors, we investigate yawing of the anisotropic compliant walls also regarding transient growth as well. Since yawing of the compliant wall breaks symmetry of left- and right-traveling waves, we need to consider negative spanwise wavenumbers β.

In fig. 6.6, the maximum transient growth is shown for a yaw angle of $\psi = 35°$. Compared to the case with $\psi = 0°$, the exponentially unstable region is larger for $\beta > 0$. Again, the global maximum of transient is unaltered. For the 2D-case, i.e. $\beta = 0$, the transient growth is slightly reduced compared to the case of $\psi = 0°$ and the rigid wall case. So yawing of the compliant wall indeed has an influence on transient growth, but in this case no change of the classical transient growth mechanism can be observed.
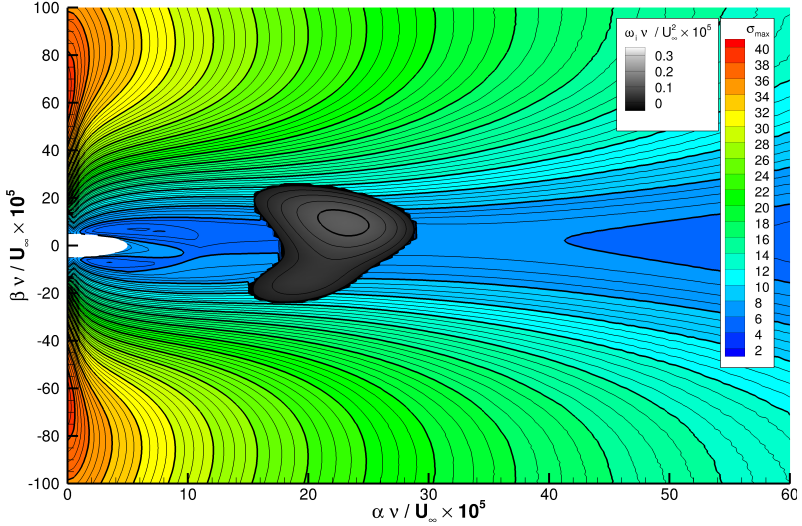
Figure 6.6 Color-contours of maximum transient growth $\sigma_{\max}$ in the α–β-
plane for $Re_{\delta_1} = 1000$ in the compliant wall case, with $\theta = 60°$ and
$\psi = 35°$. Black-white contours denote the exponentially unstable region
with temporal amplification rate ω_i.

6.5 Conclusions on Transient Growth for the Anisotropic Compliant Wall

In this chapter the transient growth of disturbances of the Blasius boundary
layer over anisotropic compliant walls was investigated. Hereby the wall
parameters were chosen based on the two-dimensional investigations and
optimization of Carpenter [15]. It was shown, that the compliant wall can
indeed alter the transient growth of disturbances. In the two-dimensional
case it increased maximum transient growth slightly. The two-dimensional
case is however not relevant, due to the much stronger three-dimensional
transient growth.

In contrast to the works of Hœpffner [34], who has shown that spanwise
standing waves of the compliant wall can be involved with transient growth

within plane channel flow, such a mechanism was not found for the chosen compliant walls. What is remarkable in the investigations is, that the classical transient growth mechanism of streamwise vortices is not altered by the compliant wall at all. This gives rise to the question whether this mechanism can be altered by compliant walls in general.

The attenuation of modal growth by using compliant walls with an effective reduction of N-factors increases the importance of transient growth for these materials. The fact that the investigated compliant materials do not introduce any relevant transient growth is good news. However, for the flow over compliant walls, transient growth must be considered more than for the rigid wall case.

7 Conclusions and Outlook

The effect of anisotropic compliant walls on three-dimensional disturbances in the Blasius boundary layer was investigated in this work. The prevailing surface-based anisotropic compliant wall model found in literature was extended to allow yawing of the compliant material with respect to the flow. It is important to note that most works on the stability of flow over compliant walls consider only two-dimensional disturbances. While it is true that the two-dimensional case can be transformed to the three-dimensional case, and vice versa, via Squire transformation, this is rarely a valid approach. The current work incorporates a compliant wall model which enforces a coupling of the Orr-Sommerfeld and the Squire equation. This leads to the implication, that the Squire-transformation is no longer applicable. Also the Squire-theorem is no longer valid in this case, and that three-dimensional modes can reach certain amplitudes to trigger laminar-turbulent transition before their two-dimensional counterparts has always been the case.

Two complimentary numerical solvers, a shooting solver, and a matrix solver, were developed to enable the evaluation of three-dimensional linear instabilities. A novel approach was introduced in the shooting solver, which highly increases robustness by scaling the boundary condition residual at the wall with disturbance pressure. The implementation of these solvers is also somewhat special, because the two governing equations must be solved in coupled form. The numerical accuracy of the solvers was evaluated, and it appears that the solvers produce results of sufficient accuracy to investigate exponential (modal) and transient (non-modal) instabilities.

Due to the plethora of compliant wall parameters, two parameter sets found in literature were chosen, which were optimized in a purely two-dimensional framework for attenuation of the Tollmien-Schlichting insta-bility, while keeping Flow-Induced Surface Instabilities marginally stable.

The presented investigations have shown that purely two-dimensional stability calculations can lead to inherently wrong conclusions on the stability of flows over compliant surfaces. Also, the calculations have shown that transition prediction based on N-factors is slightly overpredicted. However, for the two chosen materials, a significant delay of laminar-turbulent transition is predicted. Therefore it confirms that anisotropic compliant walls can significantly delay transition.

Investigations on transient growth have also been carried out for the two compliant wall parameter sets. These have shown that no additional transient growth mechanism with relevant amplification is introduced by the compliant walls. Here it is important to note that the classical transient-growth mechanism, incorporating streamwise vortices, is not altered by the compliant walls. These results show that it is unlikely for compliant walls to attenuate this transient-growth mechanism.

A yawing of the chosen compliant materials, inspired by findings that dermal ridges in delphinoidea make an angle to the local flow direction, have not turned out to show a benefit in delay of laminar-turbulent transition for the investigated parameters sets. This was the case for modal and non-modal growth. Concerning modal growth, it was shown that yawing alters the wave propagation angle of the most amplified wave. This suggests, that yawing of the anisotropic material could help in optimization of compliant wall parameters if a variation of wall parameters in the downstream direction is admitted.

In the presented investigations the compliant wall parameters have been kept constant in streamwise direction. Also, the boundary layer was restricted to Blasius flow. However, the stability solvers which were developed for this work can be used for a much wider field of investigations. The inclusion of crossflow and pressure gradients in the governing equations gives the possibility to apply the presented numerics to various external flows, like e.g., the Falkner-Skan-Cooke boundary layers. A local adaption of the compliant wall parameters could be used to attenuate instability waves even more. This will lead to an ambitious optimization problem for compliant wall parameters. Hereby, the solvers for the calculation of the

stability equations must be very robust. The temptation to optimize wall parameters should be resisted as long as possible, because the optimized wall parameters need to be realizable in a future practice. Otherwise, the result will be of little use.

A weak point of most investigations which incorporate compliant walls, including this work, is that they lack comparisons with experiments. Experimental evidence is a key factor for a future application of these findings and should be taken as priority in future investigations. The author hopes that the current work can help finding an experimental setup for future investigations.

A Employed Compliant Wall Parameters

Table A.1: Employed compliant wall parameters of the presented investigations.

parameter set	θ	$C_m^{(\nu)}$	$C_k^{(\nu)}$	$C_b^{(\nu)}$	$C_i^{(\nu)}$	$C_\nu^{(\nu)}$
1^a	$0°$	1.464×10^4	4.443×10^{-5}	1.208×10^{12}	—	—
2	$60°$	2.211×10^3	7.405×10^{-6}	1.529×10^9	2.814×10^3	0.000×10^0
3	$75°$	5.777×10^2	1.983×10^{-6}	2.281×10^7	6.152×10^2	0.000×10^0

[a] isotropic wall case

B Linear Stability Equations

> It is not the linearization that limits insight. It is the
> nature of the state that we choose to linearize about.
>
> *Erik Eady*

Coordinate System

We define a Cartesian coordinate system where the $x^\star$-axis points in stream-wise direction, the $y^\star$-axis in wall-normal direction and the $z^\star$-axis combines the axes to a right-handed coordinate system pointing in spanwise direction. The fluid velocities in the aforementioned directions are $u^\star$, $v^\star$ and $w^\star$, respectively, with starred quantities denoting dimensional quantities.

Non-Dimensionalization

The quantities in the equations of this work are non-dimensionalized using the following relations:

$$x = \frac{x^\star}{L^\star} \qquad y = \frac{y^\star}{L^\star} \qquad z = \frac{z^\star}{L^\star}$$
$$u = \frac{u^\star}{U_\infty^\star} \qquad v = \frac{v^\star}{U_\infty^\star} \qquad w = \frac{w^\star}{U_\infty^\star}$$
$$t = \frac{U_\infty^\star}{L^\star} t^\star \qquad \rho = \frac{\rho^\star}{\rho_\infty^\star} \qquad p = \frac{p^\star}{\rho_\infty^\star U_\infty^{\star\,2}} \tag{B.1}$$

Hereby, the quantities $U_\infty^\star$, $\rho_\infty^\star$, $L^\star$ are a reference velocity, reference density, and reference length, respectively, and can be chosen arbitrarily. The Reynolds number

$$Re = \frac{\rho_\infty^\star U_\infty^\star L^\star}{\mu^\star} = \frac{U_\infty^\star L^\star}{\nu^\star} \;\;, \tag{B.2}$$

with $\mu^\star$ and $\nu^\star$ being the dynamic and the kinematic viscosity, respectively, depends on these chosen quantities. Dimensional quantities sharing the

same units are scaled analogous, e.g., Young's modulus E and pressure p. Furthermore, we define the wall-normal vorticity as

$$\Omega = \frac{\partial u}{\partial z} - \frac{\partial w}{\partial x} \ . \tag{B.3}$$

Linearization

To apply the linear stability theory (LST) on fluid flows, the governing equations must be linearized. Hereby, the fluid quantities φ are written as a superposition of their steady mean part $\bar{\varphi}$ and their fluctuating part $\acute{\varphi}$ as

$$\varphi(x, y, z, t) = \bar{\varphi}(x, y, z) + \acute{\varphi}(x, y, z, t) \ . \tag{B.4}$$

Additionally, it is assumed that the fluctuating part of the fluid quantities are much smaller than their mean part

$$\acute{\varphi}(x, y, z, t) \ll \bar{\varphi}(x, y, z) \ . \tag{B.5}$$

Unless otherwise denoted, a Falkner-Skan similarity solution was taken as the steady mean part of the flow, which was calculated by an improved version of Seebach's [58] implementation.

Local Parallelism

Since boundary layers are typically thin with respect to their streamwise extent, some terms in the linearized Navier-Stokes equations are negligible. Analyzing the order of magnitude of the different terms, it can be shown that terms involving $\bar{v}$ are orders of magnitude smaller compared to terms involving $\bar{u}$ and $\bar{w}$, and that terms with derivatives with respect to x and z are orders of magnitude smaller than terms with derivatives with respect to y. This approach is analogous to the derivation of Prandtl's boundary layer equations. Assuming that all disturbance velocity components have the same order of magnitude, the linearized Navier-Stokes equations simplify as if one assumes that the baseflow velocity profile is only dependent on the wall-normal direction y and that the baseflow has no velocity component in y direction, i.e.

$$\bar{u} = \bar{u}(y) \qquad \bar{w} = \bar{w}(y) \qquad \bar{v} = 0 \ . \tag{B.6}$$

The mean flow is virtually assumed as parallel flow. Therefore, one speaks of the locally-parallel assumption. This procedure implicitly assumes that the streamwise wavelength of the disturbances is small compared to the streamwise extent of the boundary layer.

Modal Approach

The form of the disturbance equations suggests introducing a modal approach of the form

$$\acute{\varphi}(x, y, z, t) = \tilde{\varphi}(y) \, e^{\mathrm{i}(\alpha x + \beta z - \omega t)} + \text{complex conjugate} \, , \qquad \text{(B.7)}$$

with modes that are waves and have an amplitude $\tilde{\varphi}$ which is dependent on y only. This reduces the disturbance equations to a set of ordinary differential equations. The generally complex quantities α, β, and ω are the streamwise wavenumber, spanwise wavenumber, and the angular frequency, respectively, and are in general complex quantities. The real part of the complex wavenumbers is the physical wavenumber and the real part of the complex angular frequency is the physical angular frequency. The imaginary part of the complex wavenumbers is the spatial amplification rate and the imaginary part of the complex angular frequency is the temporal amplification rate. The phase velocity of the disturbance modes is

$$c_{\text{ph.}} = \frac{\omega_r}{\alpha_r} \quad . \qquad \text{(B.8)}$$

For simplicity we define the complex resulting wavenumber as

$$\kappa = \sqrt{\alpha^2 + \beta^2} \quad . \qquad \text{(B.9)}$$

Note that in general the real part of κ is not equal to the resulting physical wavenumber.

The modal approach implies periodicity in spanwise direction in case the imaginary part of the spanwise wavenumber β is zero. Throughout this work this is assumed to be the case: All derivatives of the baseflow with respect to the spanwise direction are zero.

Formulations of the Linear Stability Equations

Different formulations of the linear stability equations can be chosen which of course have their own advantages and disadvantages. Mack [45, sect. 2.5], inter alia, presents the following definition of the quantities

$$z_1 = \alpha\tilde{u} + \beta\tilde{w} \tag{B.10}$$

$$z_2 = \alpha\tilde{u}_y + \beta\tilde{w}_y \tag{B.11}$$

$$z_3 = \tilde{v} \tag{B.12}$$

$$z_4 = \tilde{p} \tag{B.13}$$

$$z_5 = \alpha\tilde{w} - \beta\tilde{u} \tag{B.14}$$

$$z_6 = \alpha\tilde{w}_y - \beta\tilde{u}_y \tag{B.15}$$

that form the linear stability equations

$$z_{1,y} = z_2 \tag{B.16}$$

$$z_{2,y} = \left(\kappa^2 + \mathrm{i}Ret_1\right) z_1 + Ret_2 z_3 + \mathrm{i}\kappa^2 Re z_4 \tag{B.17}$$

$$z_{3,y} = -\mathrm{i}z_1 \tag{B.18}$$

$$z_{4,y} = -\mathrm{i}Re^{-1}z_2 - \left(\mathrm{i}t_1 + \kappa^2 Re^{-1}\right) z_3 \tag{B.19}$$

$$z_{5,y} = z_6 \tag{B.20}$$

$$z_{6,y} = Ret_3 z_3 + \left(\kappa^2 + \mathrm{i}Ret_1\right) z_5 \ . \tag{B.21}$$

Some terms of the linear stability equations are simplified as

$$t_1 = \alpha\bar{u} + \beta\bar{w} - \omega \tag{B.22}$$

$$t_2 = \alpha\bar{u}_y + \beta\bar{w}_y \tag{B.23}$$

$$t_3 = \alpha\bar{w}_y - \beta\bar{u}_y \tag{B.24}$$

to reduce the length of the equations. In the implemented solver, these terms are stored after their calculation when they are used again, e.g., for the different stages of the Runge-Kutta scheme. The equations (B.16)-(B.19) are equivalent to the Orr-Sommerfeld equation and the equations (B.20)-(B.21) are equivalent to the Squire equation.

In contrast to the formulation as a system of first order equations, the stability equations can be written as two coupled equations of each fourth and second order. The fourth-order equation, namely the *Orr-Sommerfeld* equation, is

$$Re\left(\alpha\bar{u} + \beta\bar{w}\right)\left(\tilde{v}_{yy} - \kappa^2\tilde{v}\right) + \mathrm{i}\left(\tilde{v}_{yyyy} - 2\kappa^2\tilde{v}_{yy} + \kappa^4\tilde{v}\right)$$
$$- Re\left(\alpha\bar{u}_{yy} + \beta\bar{w}_{yy}\right)\tilde{v} = \omega\left[Re\left(\tilde{v}_{yy} - \kappa^2\tilde{v}\right)\right] \quad, \quad \text{(B.25)}$$

and the second order equation, namely the *Squire* equation, is

$$Re\left(\alpha\bar{w}_y - \beta\bar{u}_y\right)\tilde{v} + \mathrm{i}\left(\kappa^2\tilde{\Omega} - \tilde{\Omega}_{yy}\right) - Re\left(\alpha\bar{u} + \beta\bar{w}\right)\tilde{\Omega} = \omega\left[-Re\tilde{\Omega}\right] \quad.$$
$$\text{(B.26)}$$

Choice of the Formulation

Equations (B.10)-(B.15) have the advantage, that they contain solely the base flow and its first derivative. Errors emerging from taking the second derivative of the base flow do not appear. This is valuable when experimental data is used. Also, their quantities contain the disturbance pressure directly, so that it does not have to be calculated out of the disturbance velocities, which incorporates up to third derivatives with respect to y.

Equations (B.25) and (B.26) have the advantage, that only the wall-normal disturbance velocity $\tilde{v}$ and the wall-normal vorticity $\tilde{\Omega}_y$ appear in the equations. This fact is important when computing the LST-eigenvalue problem with a dense-matrix method, such as the QZ-algorithm because the size of the discretized matrix is the number of collocations points times the number of variables. Moreover, the computational cost of the QZ-algorithm is proportional to the size of the matrix to the power of three. Hence, this formulation has a significantly lower computational cost when using dense-matrix methods.

Useful Formulas

For conversion between the formulations of the linear stability equations present in this work we have:

$$z_1 = i\tilde{v}_y$$

$$z_2 = i\tilde{v}_{yy}$$

$$z_3 = \tilde{v}$$

$$z_4 = \left(\tilde{v}_{yyy} - \left(\kappa^2 + iRe\left(\alpha\bar{u} + \beta\bar{w}\right)\tilde{v}_y\right) + iRe\omega\tilde{v}_y + iRet_2\tilde{v}\right)\frac{1}{\kappa^2 Re}$$

$$z_5 = i\tilde{\Omega}$$

$$z_6 = i\tilde{\Omega}_y$$

$$\tilde{u} = \kappa^{-2}\left(\alpha z_1 - \beta z_5\right) = i\kappa^{-2}\left(\alpha\tilde{v}_y - \beta\tilde{\Omega}\right)$$

$$\tilde{v} = z_3$$

$$\tilde{w} = \kappa^{-2}\left(\beta z_1 - \alpha z_5\right) = i\kappa^{-2}\left(\beta\tilde{v}_y + \alpha\tilde{\Omega}\right)$$

$$\tilde{p} = z_4$$

$$\tilde{\Omega} = -iz_5$$

$$t_1 = \alpha\bar{u} + \beta\bar{w} - \omega$$

$$t_2 = \alpha\bar{u}_y + \beta\bar{w}_y$$

$$t_3 = \alpha\bar{w}_y - \beta\bar{u}_y$$

$$t_4 = \alpha\cos\psi + \sin\psi$$

$$t_5 = \alpha\sin\psi - \beta\cos\psi$$

$$t_6 = \bar{u}_{yy}\cos\psi + \bar{w}_{yy}\sin\psi$$

$$t_7 = \alpha\bar{u} + \beta\bar{w}$$

C Contents of the Stability Matrix

In the following is explained how the matrices are composed for the compliant-wall stability problem. The matrices $\mathbf{A}$ and $\mathbf{B}$ of equation (4.1) can be written as

$$
\mathbf{A} = \begin{bmatrix}
\mathbf{A}^{(1,1)} & \mathbf{0} & \mathbf{0} \\
\mathbf{A}^{(2,1)} & \mathbf{A}^{(2,2)} & \mathbf{A}^{(2,3)} \\
\mathbf{A}^{(3,1)} & \mathbf{0} & \mathbf{0} \\
\mathbf{A}^{(4,1)} & \mathbf{0} & \mathbf{0} \\
\mathbf{A}^{(5,1)} & \mathbf{0} & \mathbf{0} \\
\mathbf{A}^{(6,1)} & \mathbf{0} & \mathbf{0} \\
\mathbf{A}^{(7,1)} & \mathbf{A}^{(7,2)} & \mathbf{0} \\
\mathbf{0} & \mathbf{A}^{(8,2)} & \mathbf{0} \\
\mathbf{A}^{(9,1)} & \mathbf{0} & \mathbf{0}
\end{bmatrix} , \tag{C.1}
$$

and

$$
\mathbf{B} = \begin{bmatrix}
\mathbf{B}^{(1,1)} & \mathbf{0} & \mathbf{0} \\
\mathbf{B}^{(2,1)} & \mathbf{0} & \mathbf{0} \\
\mathbf{B}^{(3,1)} & \mathbf{0} & \mathbf{0} \\
\mathbf{B}^{(4,1)} & \mathbf{0} & \mathbf{0} \\
\mathbf{B}^{(5,1)} & \mathbf{0} & \mathbf{0} \\
\mathbf{B}^{(6,1)} & \mathbf{B}^{(6,2)} & \mathbf{0} \\
\mathbf{0} & \mathbf{B}^{(7,2)} & \mathbf{0} \\
\mathbf{0} & \mathbf{B}^{(8,2)} & \mathbf{0} \\
\mathbf{0} & \mathbf{0} & \mathbf{B}^{(9,3)}
\end{bmatrix} . \tag{C.2}
$$

Each row of the matrices constitutes a boundary condition or a governing equation evaluated at the collocation points. The submatrices

$$
\mathbf{A}^{(1,1)} = \mathrm{i}t_2 \mathbf{D}^{(0)}_{1,1:N_c} , \tag{C.3}
$$

and

$$\mathbf{B}^{(1,1)} = \tan\theta t_4 \mathbf{D}^{(0)}_{1,1:N_c} - i\mathbf{D}^{(1)}_{1,1:N_c} \tag{C.4}$$

constitute the boundary condition (2.30). The submatrices

$$\mathbf{A}^{(2,1)} = \kappa^2 Re C_d \mathbf{D}^{(0)}_{1,1:N_c} + \cos^2\theta \left(\mathbf{D}^{(3)}_{1,1:N_c} - 3\kappa^2 \mathbf{D}^{(1)}_{1,1:N_c} \right)$$
$$+ \cos^2\theta\, iRe \left(t_2 \mathbf{D}^{(0)}_{1,1:N_c} - t_7 \mathbf{D}^{(1)}_{1,1:N_c} \right) - \sin\theta\cos\theta\, it_4 \left(\kappa^2 \mathbf{D}^{(0)}_{1,1:N_c} + \mathbf{D}^{(2)}_{1,1:N_c} \right) \ , \tag{C.5}$$

$$\mathbf{A}^{(2,2)} = -\sin\theta\cos\theta t_5\, i\mathbf{D}^{(1)}_{1,1:N_c} \ , \tag{C.6}$$

$$\mathbf{A}^{(2,3)} = \kappa^2 \left(Re C_k + \cos^2\theta Re \left(\kappa^4 C_b + \alpha^2 C_{Tx} + \beta^2 C_{Tz} \right) \right.$$
$$\left. + \sin^2\theta Re C_i \left(\kappa^2 - C_\nu t_5^2 \right) - \sin\theta\cos\theta t_6 \right) \ , \tag{C.7}$$

and

$$\mathbf{B}^{(2,1)} = iRe \left(\kappa^2 C_m \mathbf{D}^{(0)}_{1,1:N_c} - \cos^2\theta \mathbf{D}^{(1)}_{1,1:N_c} \right) \tag{C.8}$$

constitute the boundary condition (2.32). The submatrices

$$\mathbf{A}^{(3,1)} = Re \left(\alpha \operatorname{diag}(\mathbf{u}_{3:N_c-2}) + \beta \operatorname{diag}(\mathbf{w}_{3:N_c-2}) \right)$$
$$\left(\mathbf{D}^{(2)}_{3:N_c-2,1:N_c} - \kappa^2 \mathbf{D}^{(0)}_{3:N_c-2,1:N_c} \right) +$$
$$i \left(\mathbf{D}^{(4)}_{3:N_c-2,1:N_c} - 2\kappa^2 \mathbf{D}^{(2)}_{3:N_c-2,1:N_c} + \kappa^4 \mathbf{D}^{(0)}_{3:N_c-2,1:N_c} \right)$$
$$- Re \left(\alpha \operatorname{diag}(\mathbf{u}_{yy,3:N_c-2}) + \beta \operatorname{diag}(\mathbf{w}_{yy,3:N_c-2}) \right) \mathbf{D}^{(0)}_{3:N_c-2,1:N_c} \ , \tag{C.9}$$

and

$$\mathbf{B}^{(3,1)} = Re \left(\mathbf{D}^{(2)}_{2:N_c-1,1:N_c} - \kappa^2 \mathbf{D}^{(0)}_{2:N_c-1,1:N_c} \right) \tag{C.10}$$

constitute the Orr-Sommerfeld equation (B.25) evaluated at the points $y_3 \ldots y_{N_c-2}$. The submatrices

$$\mathbf{A}^{(4,1)} = \left(\mathbf{D}^{(2)}_{N_c,1:N_c} + \kappa \mathbf{D}^{(1)}_{N_c,1:N_c} \right) \mu \ , \tag{C.11}$$

and

$$\mathbf{B}^{(4,1)} = \left(\mathbf{D}^{(2)}_{N_c,1:N_c} + \kappa \mathbf{D}^{(1)}_{N_c,1:N_c} \right) \tag{C.12}$$

constitute the boundary condition (4.14). The submatrices

$$\mathbf{A}^{(5,1)} = \left(\mathbf{D}^{(1)}_{N_c,1:N_c} + \kappa \mathbf{D}^{(0)}_{N_c,1:N_c} \right) \mu \ , \tag{C.13}$$

and

$$\mathbf{B}^{(5,1)} = \left(\mathbf{D}^{(1)}_{N_c,1:N_c} + \kappa \mathbf{D}^{(0)}_{N_c,1:N_c} \right) \tag{C.14}$$

constitute the boundary condition (4.15). The submatrices

$$\mathbf{A}^{(6,1)} = \mathrm{i} t_3 \mathbf{D}^{(0)}_{1,1:N_c} \ , \tag{C.15}$$

$$\mathbf{B}^{(6,1)} = \tan \theta t_5 \mathbf{D}^{(0)}_{1,1:N_c} \ , \tag{C.16}$$

and

$$\mathbf{B}^{(6,2)} = - \mathrm{i} \mathbf{D}^{(0)}_{1,1:N_c} \tag{C.17}$$

constitute the boundary condition (2.31). The submatrices

$$\mathbf{A}^{(7,1)} = Re \left(\alpha \, \mathrm{diag}(\mathbf{w}_{y,2:N_c-1}) - \beta \, \mathrm{diag}(\mathbf{u}_{y,2:N_c-1}) \right) \mathbf{D}^{(0)}_{2:N_c-1,1:N_c} \ , \tag{C.18}$$

$$\mathbf{A}^{(7,2)} = \mathrm{i} \left(\kappa^2 \mathbf{D}^{(0)}_{2:N_c-1,1:N_c} - \mathbf{D}^{(2)}_{2:N_c-1,1:N_c} \right)$$
$$- Re \left(\alpha \, \mathrm{diag}(\mathbf{u}_{2:N_c-1}) + \beta \, \mathrm{diag}(\mathbf{w}_{2:N_c-1}) \right) \mathbf{D}^{(0)}_{2:N_c-1,1:N_c} \ , \tag{C.19}$$

and

$$\mathbf{B}^{(7,2)} = -Re \mathbf{D}^{(0)}_{2:N_c-1,1:N_c} \tag{C.20}$$

constitute the Squire equation (B.26) evaluated at the points $y_2 \dots y_{N_c-1}$. The submatrices

$$\mathbf{A}^{(8,2)} = \left(\mathbf{D}^{(1)}_{N_c,1:N_c} + \kappa \mathbf{D}^{(0)}_{N_c,1:N_c} \right) \mu \ , \tag{C.21}$$

and

$$\mathbf{B}^{(8,2)} = \left(\mathbf{D}^{(1)}_{N_c,1:N_c} + \kappa \mathbf{D}^{(0)}_{N_c,1:N_c} \right) \tag{C.22}$$

constitute the boundary condition (4.16). The submatrices

$$\mathbf{A}^{(9,1)} = \mathrm{i} \mathbf{D}^{(0)}_{1,1:N_c} \ , \tag{C.23}$$

and

$$\mathbf{B}^{(9,3)} = 1 \tag{C.24}$$

constitute equation (2.34).

D Validation of the Linear Stability Solvers

For code validation numerical results of the shooting method are compared to results in literature. Fig. D.1 shows neutral stability curves in the $(\alpha\delta_1)-(Re_{\delta_1})$ plane, for the Blasius boundary layer over rigid and compliant walls. Symbols denote scanned and digitized data of Carpenter [15, fig.19], lines denote the solution obtained by the shooting method. The results for the compliant walls are in perfect agreement to each other. For the rigid wall case the results are in less than perfect agreement. A comparison to other rigid-wall results in literature shows perfect agreement with our shooting method. So the differences can be explained by a deviation of Carpenters results.
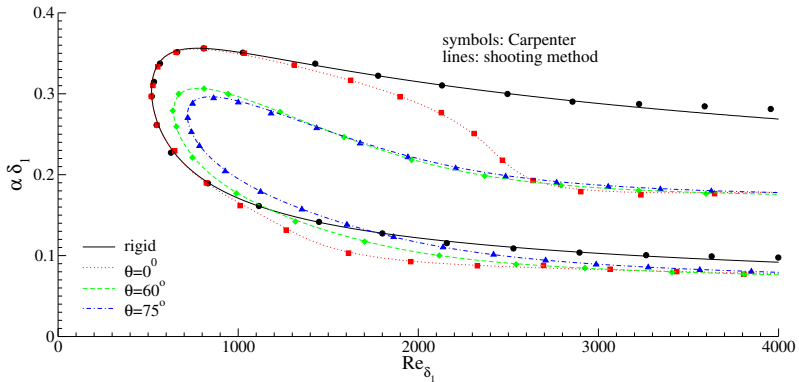

Figure D.1 Neutral stability curves, for the Blasius boundary layer over rigid and compliant walls, in the $(\alpha\delta_1)-(Re_{\delta_1})$ plane. Symbols denote scanned and digitized data of Carpenter [15, fig.19], lines denote the results of the shooting method. Wall parameters are listed in table A.1.

Fig. D.2 shows contours of maximum transient growth in the $\alpha-\beta$ plane for the Blasius boundary layer over a rigid wall at $Re_{\delta_1} = 1000$. These

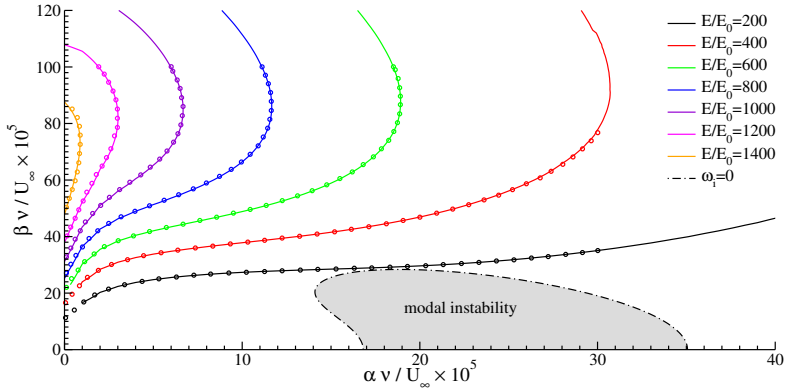results show very good agreement of the present method and the scanned and digitized data of Schmid [55].

Figure D.2 Contours of maximum transient growth in the $\alpha - \beta$ plane for the Blasius boundary layer over a rigid wall at $Re_{\delta_1} = 1000$. Lines denote the results of the current method, symbols denote scanned and digitized data of Schmid and Henningson [55, fig. 4.6].

The results obtained by the implementations of the numerical methods, presented in this work, are in perfect agreement to well-respected results literature. It is notable that the results of Carpenter were obtained by different numerical methods, different formulations of the governing equations, and different boundary conditions. Furthermore, it is to note that both, the implementation of the shooting method, and the implementation of the matrix method, exhibit results which are also in perfect agreement. Hereby, these methods also use different formulations of equations, boundary conditions.

Bibliography

[1] ANDERSON E., BAI Z., BISCHOF C., BLACKFORD S., DEMMEL J., DON-GARRA J., DU CROZ J., GREENBAUM A., HAMMARLING S., MCKEN-NEY A., AND SORENSEN D. *LAPACK Users' Guide*. 3rd edition. Society for Industrial and Applied Mathematics, 1999. ISBN 0898714478.

[2] BALTENSPERGER R. AND TRUMMER M.R. *Spectral differencing with a twist*. SIAM Journal on Scientific Computing, 24, pp. 1465–1487, 2002. DOI 10.1137/S1064827501388182.

[3] BATCHELOR G.K. *An Introduction to Fluid Dynamics*. 1st edition. Cambridge Mathematical Library, Cambridge University Press, 2000. ISBN 0521663962.

[4] BECHERT D.W., BRUSE M., HAGE W., VAN DER HOEVEN J.G.T., AND HOPPE G. *Experiments on drag-reducing surfaces and their optimization with an adjustable geometry*. Journal of Fluid Mechanics, 338, pp. 59–87, 1997. DOI 10.1017/S0022112096004673.

[5] BENJAMIN T.B. *Effects of a flexible boundary on hydrodynamic stability*. Journal of Fluid Mechanics, 9(04), pp. 513–532, 1960. DOI 10.1017/S0022112060001286.

[6] BENJAMIN T.B. *The threefold classification of unstable disturbances in flexible surfaces bounding inviscid flows*. Journal of Fluid Mechanics, 16(03), pp. 436–450, 1963. DOI 10.1017/S0022112063000884.

[7] BERRUT J.P. AND TREFETHEN L.N. *Barycentric lagrange interpolation*. SIAM Review, 46(3), pp. 501–517, 2004. DOI 10.1137/S0036144502417715.

[8] BOYD J.P. *Chebyshev and Fourier Spectral Methods*. 2nd edition. Dover Publications, Mineola, New York, 2001. ISBN 0486411834.

[9] BOYER G. *Investigation of the Influence of Wall Parameters and Pressure Gradients on the Linear Stability of Laminar Boundary Layers over Compliant Walls*. Internship report, Institut für Aerodynamik und Gasdynamik, Universität Stuttgart, 2008.

[10] BREUER K.S., EVERSON, AND M. R. *On the errors incurred calculating derivatives using Chebyshev polynomials*. Journal of Computational Physics, 99(1), pp. 56–67, 1992. ISSN 0021-9991. DOI 10.1016/0021-9991(92)90274-3.

[11] BRONSTEIN, SEMENDJAJEW, MUSIOL, AND MÜHLIG. *Taschenbuch der Mathematik*. 6th edition. Harri Deutsch, Frankfurt am Main, 2005. ISBN 3817120060.

[12] BUTLER K.M. AND FARRELL B.F. *Three-dimensional optimal perturbations in viscous shear flow*. Physics of Fluids A, 4(8), pp. 1637–1650, 1992. DOI 10.1063/1.858386.

[13] CARPENTER P.W. AND GARRAD A.D. *The hydrodynamic stability of flow over Kramer-type compliant surfaces. Part 1. Tollmien-Schlichting instabilities*. Journal of Fluid Mechanics, 155, pp. 465–510, 1985. DOI 10.1017/S0022112085001902.

[14] CARPENTER P.W. AND GARRAD A.D. *The hydrodynamic stability of flow over Kramer-type compliant surfaces. Part 2. flow-induced surface instabilities*. Journal of Fluid Mechanics, 170, pp. 199–232, 1986. DOI 10.1017/S002211208600085X.

[15] CARPENTER P.W. AND MORRIS P.J. *The effect of anisotropic wall compliance on boundary-layer stability and transition*. Journal of Fluid Mechanics, 218, pp. 171–223, 1990. DOI 10.1017/S0022112090000970.

[16] CONTE S.D. *The numerical solution of linear boundary value problems*. SIAM Review, 8(3), pp. 309–321, 1966. DOI 10.1137/1008063.

[17] CRIMINALE W.O., JACKSON T.L., AND JOSLIN R.D. *Theory and Computation of Hydrodynamic Stability*. Cambridge University Press, 2003. ISBN 0521632005.

[18] DANABASOGLU G. AND BIRINGEN S. *A Chebyshev matrix method for the spatial modes of the Orr-Sommerfeld equation*. International Journal for Numerical Methods in Fluids, 11(7), pp. 1033–1037, 1990. DOI 10.1002/fld.1650110709.

[19] DANIEL T.L. *Fish mucus: In situ measurements of polymer drag reduction*. Biological Bulletin, 160(3), pp. 376–382, 1981.

[20] DAVENPORT J., HUGHES R., SHORTEN M., AND LARSEN P. *Drag reduction by air release promotes fast ascent in jumping emperor penguins—a novel hypothesis*. Marine Ecology Progress Series, 430, pp. 171–182, 2011. DOI 10.3354/meps08868.

[21] DUNCAN J.H. *A comparison of wave propagation on the surfaces of simple membrane walls and elastic coatings bounded by a fluid flow*. Journal of Sound and Vibration, 119(3), pp. 565–573, 1987.

[22] FASEL H., THUMM A., AND BESTEK H. *Direct numerical simulation of transition in supersonic boundary layers: oblique breakdown*. In: *American Society of Mechanical Engineers, Fluids Engineering Division (Publication) FED*, volume 151, pp. 77–92. ASME, 1993. ISBN 0791809595.

[23] FORNBERG. B. *Generation of finite difference formulas on arbitrarily spaced grids*. Mathematics of Computation, 51(184), pp. 699–706, 1988. DOI 10.1090/S0025-5718-1988-0935077-0.

[24] FORNBERG B. *A Practical Guide to Pseudospectral Methods*. Cambridge University Press, 1998. ISBN 0521645646.

[25] GAD-EL-HAK M. *Compliant coatings for drag reduction*. Progress in Aerospace Sciences, 38, pp. 77–99, 2002.

[26] GASTER M. *Is the dolphin a red herring?* In: H.W. Liepmann and R. Narasimha (editors), *Proceedings of the IUTAM Symposium on Turbulence Management and Relaminarization*, pp. 285–304. IUTAM Bookseries, Springer, Berlin, 1988. ISBN 3540185747.

[27] GODUNOV S.K. *Numerical solution of boundary-value problems for systems of linear ordinary differential equations.* Uspekhi Matematicheskikh Nauk, 16(3(99)), pp. 171–174, 1961.

[28] GOLUB G.H. AND VAN LOAN C.F. *Matrix Computations.* 3rd edition. Johns Hopkins University Press, 1996. ISBN 0-8018-5414-8.

[29] GRAY J. *Studies in animal locomotion: VI the propulsive powers of the dolphin.* Journal of Experimental Biology, 13, pp. 192–199, 1936.

[30] GROSCH C.E. AND ORSZAG S.A. *Numerical solution of problems in unbounded regions: Coordinate transforms.* Journal of Computational Physics, 25(3), pp. 273–296, 1977. DOI 10.1016/0021-9991(77)90102-4.

[31] GROSS D., HAUGER W., SCHRÖDER J., AND WALL W. *Technische Mechanik 2.* 9th edition. Springer, Berlin, 2007. ISBN 9783540707622.

[32] GROSS D., HAUGER W., AND WRIGGERS P. *Technische Mechanik 4.* 6th edition. Springer, Berlin, 2007. ISBN 9783540707370.

[33] HAJ-HARIRI H. *Transformations reducing the order of the parameter in differential eigenvalue problems.* Journal of Computational Physics, 77(2), pp. 472–484, 1988. ISSN 0021-9991. DOI 10.1016/0021-9991(88)90178-7.

[34] HŒPFFNER J., BOTTARO A., AND FAVIER J. *Mechanisms of non-modal energy amplification in channel flow between compliant walls.* Journal of Fluid Mechanics, 642, pp. 489–507, 2010. DOI 10.1017/S0022112009991935.

[35] HUERRE P. AND MONKEWITZ P.A. *Local and global instabilities in spatially developing flows.* Annual Review of Fluid Mechanics, 22(1), pp. 473–537, 1990. DOI 10.1146/annurev.fl.22.010190.002353.

[36] JOSLIN R.D. *The effect of compliant walls on three-dimensional primary and secondary instabilities in boundary layer transition*. Technical Report TR91-003, The Pennsylvania State University, Applied Research Laboratory, 1991.

[37] JOSLIN R.D. AND MORRIS P.J. *The sensitivity of flow and surface instabilities to changes in compliant wall properties*. Journal of Fluids and Structures, 3(4), pp. 423–437, 1989. DOI 10.1016/S0889-9746(89)80020-9.

[38] JOSLIN R.D. AND MORRIS P.J. *Effect of compliant walls on secondary instabilities in boundary-layer transition*. AIAA Journal, 30(2), pp. 332–339, 1992.

[39] JOSLIN R.D., MORRIS P.J., AND CARPENTER P.W. *Role of three-dimensional instabilities in compliant wall boundary-layer transition*. AIAA Journal, 29(10), pp. 1603–1610, 1991.

[40] KOSINOV A.D. AND TUMIN A. *Resonance interaction of wave trains in supersonic boundary layer*. In: P.W. Duck and P. Hall (editors), *IUTAM Symposium on Nonlinear Instability and Transition in Three-Dimensional Boundary Layers: Proceedings of the IUTAM Symposium, Manchester, U.K., 1995*, pp. 379–388. Springer Netherlands, 1996. ISBN 9789400917002.

[41] KRAMER M.O. *Boundary layer stabilization by distributed damping*. Journal of the American Society of Naval Engineers, 72(1), pp. 25–34, 1960. ISSN 1559-3584. DOI 10.1111/j.1559-3584.1960.tb02356.x.

[42] LANDAHL M.T. *On the stability of a laminar incompressible boundary layer over a flexible surface*. Journal of Fluid Mechanics, 13(04), pp. 609–632, 1962. DOI 10.1017/S002211206200097X.

[43] LEGAC P., FISH F., WILLIAMS T., AND WEI T. *DPIV measurements on dolphins: Examining Gray's paradox*. Bulletin of the American Physical Society, 52, 2007.

[44] MACK L.M. *A numerical study of the temporal eigenvalue spectrum of the Blasius boundary layer*. Journal of Fluid Mechanics, 73(3), pp. 497–520, 1976. DOI 10.1017/S002211207600147X.

[45] MACK L.M. *Boundary-layer linear stability theory*. In: *Special Course on Stability and Transition of Laminar Flow*, volume 709 of *AGARD report*, 1984. ISBN 9283503554.

[46] MULLER D.E. *A method for solving algebraic equations using an automatic computer*. Mathematical Tables and Other Aids to Computation, 10(56), pp. 208–215, 1956. ISSN 08916837.

[47] MUNZ C.D. AND WESTERMANN T. *Numerische Behandlung gewöhnlicher und partieller Differenzialgleichungen*. Springer, Berlin, 2006. ISBN 9783540298670.

[48] NG B. AND REID W. *An initial value method for eigenvalue problems using compound matrices*. Journal of Computational Physics, 30(1), pp. 125–136, 1979. DOI 10.1016/0021-9991(79)90091-3.

[49] PAVLOV V.V. *Dolphin skin as a natural anisotropic compliant wall*. Bioinspiration & Biomimetics, 1(2), pp. 31–40, 2006. DOI 10.1088/1748-3182/1/2/001.

[50] PRESS W.H., TEUKOLSKY S.A., VETTERLING W.T., AND FLANNERY B.P. *Numerical Recipes - The Art of Scientific Computing*. 3rd edition. Cambridge University Press, New York, 2007. ISBN 9780521880688.

[51] REDDY S.C., SCHMID P.J., AND HENNINGSON D.S. *Pseudospectra of the Orr–Sommerfeld operator*. SIAM Journal on Applied Mathematics, 53(1), pp. 15–47, 1993. DOI 10.1137/0153002.

[52] RILEY J.J., EL HAK M.G., AND METCALFE R.W. *Complaint coatings*. Annual Review of Fluid Mechanics, 20(1), pp. 393–420, 1988. DOI 10.1146/annurev.fl.20.010188.002141.

[53] SCHLICHTING H. AND GERSTEN K. *Boundary-Layer Theory*. 8th edition. Springer, Berlin, 2003. ISBN 3540662707. Corrected.

[54] SCHMID P.J. *Nonmodal stability theory*. Annual Review of Fluid Mechanics, 39(1), pp. 129–162, 2007. DOI 10.1146/annurev.fluid.38.050304.092139.

[55] SCHMID P.J. AND HENNINGSON D.S. *Stability and Transition in Shear Flows*. Number 142 in Applied Mathematical Sciences, Springer, New York, 2001. ISBN 9780387989853.

[56] SCOTT M.R. *An initial value method for the eigenvalue problem for systems of ordinary differential equations*. Journal of Computational Physics, 12(3), pp. 334–347, 1973. DOI 10.1016/0021-9991(73)90156-3.

[57] SCOTT M.R. AND WATTS H.A. *Computational solution of linear two-point boundary value problems via orthonormalization*. SIAM Journal on Numerical Analysis, 14(1), pp. 40–70, 1977. DOI 10.1137/0714004.

[58] SEEBACH S. *Berechnung selbstähnlicher, laminarer Grenzschichten mit Druckgradient und Absaugung*. Studienarbeit, Institut für Aerodynamik und Gasdynamik, Universität Stuttgart, 2007.

[59] SQUIRE H.B. *On the stability for three-dimensional disturbances of viscous fluid flow between parallel walls*. Proceedings of the Royal Society of London Series A, 142(847), pp. 621–628, 1933.

[60] THUMM A. *Numerische Untersuchung zum laminar-turbulenten Strömungsumschlag in transsonischen Grenzschichtströmungen*. Ph.D. thesis, Universität Stuttgart, 1991.

[61] TISSEUR F. AND MEERBERGEN K. *The quadratic eigenvalue problem*. SIAM Review, 43(2), pp. 235–286, 2001. DOI 10.1137/S0036144500381988.

[62] TREFETHEN L.N. *Computation of pseudospectra*. Acta Numerica, 7, p. 247–295, 1999. DOI 10.1017/S0962492900002932.

[63] TREFETHEN L.N. *Spectral Methods in MATLAB*. Society for Industrial and Applied Mathematics, 2000. ISBN 0898714656.

[64] TREFETHEN L.N. AND BAU D. *Numerical Linear Algebra*. Society for Industrial and Applied Mathematics, Philadelphia, 1997. ISBN 0898713617.

[65] TREFETHEN L.N. AND EMBREE M. *Spectra And Pseudospectra: The Behavior of Nonnormal Matrices And Operators*. Princeton University Press, 2005. ISBN 0691119465.

[66] TSIGKLIFIS K. AND LUCEY A.D. *The interaction of Blasius boundary-layer flow with a compliant panel: global, local and transient analyses*. Journal of Fluid Mechanics, 827, p. 155–193, 2017. DOI 10.1017/jfm.2017.453.

[67] WELFERT B.D. *Generation of pseudospectral differentiation matrices I*. SIAM Journal on Numerical Analysis, 34(4), pp. 1640–1657, 1997. ISSN 00361429. DOI 10.1137/S0036142993295545.

[68] YEO K.S. *The hydrodynamic stability of boundary-layer flow over a class of anisotropic compliant walls*. Journal of Fluid Mechanics, 220, pp. 125–160, 1990. DOI 10.1017/S0022112090003214.

[69] YEO K.S. *The three-dimensional stability of boundary-layer flow over compliant walls*. Journal of Fluid Mechanics, 238, pp. 537–577, 1992. DOI 10.1017/S0022112092001812.

[70] YEO K.S. AND DOWLING A.P. *The stability of inviscid flows over passive compliant walls*. Journal of Fluid Mechanics, 183, pp. 265–292, 1987. DOI 10.1017/S0022112087002635.

[71] ZENGL M. AND RIST U. *Linear stability investigations of flow over yawed anisotropic compliant walls*. In: P. Schlatter and D.S. Henningson (editors), *Proceedings of the Seventh IUTAM Symposium on Laminar-Turbulent Transition, Stockholm, Sweden, 2009*, volume 18 of *IUTAM Bookseries*, pp. 601–604. Springer, Berlin, 2010. ISBN 9789048137220. DOI 10.1007/978-90-481-3723-7_110.

[72] ZENGL M. AND RIST U. *Linear-stability investigations for flow-control experiments related to flow over compliant walls*. In: C. Tropea and H. Bleckmann (editors), *Nature-Inspired Fluid Mechanics*, volume 119 of *Notes on Numerical Fluid Mechanics and Multidisciplinary Design*, pp. 223–237. Springer Berlin, 2012. ISBN 9783642283017. DOI 10.1007/978-3-642-28302-4_14.

[73] ZENGL M., VON TERZI D., AND FASEL H. *Numerical investigations of subharmonic resonance triads in a mach 3 boundary layer*. In: P. Schlatter and D.S. Henningson (editors), *Proceedings of the Seventh IUTAM Symposium on Laminar-Turbulent Transition, Stockholm, Sweden, 2009*, volume 18 of *IUTAM Bookseries*, pp. 445–450. Springer, Berlin, 2010. ISBN 9789048137220. DOI 10.1007/978-90-481-3723-7_72.